



HUNGARIAN UNIVERSITY OF
AGRICULTURE AND LIFE SCIENCES

(SZENT ISTVÁN UNIVERSITY formerly)

Load bearing capacity of soil as a homogeneous finite half-space

PhD Dissertation

by

Nihal Dawood Salman

DOI: 10.54598/002060

Gödöllő
2022

Doctoral school

Denomination: Doctoral School of Mechanical Engineering

Science: Mechanical Engineering

Leader: Prof. Dr. Gábor Kalácska, DSc
Institute of Technology
Hungarian University of Agriculture and Life Sciences,
Szent István Campus, Gödöllő, Hungary

Supervisor: Prof. Dr. Kiss Péter
Institute of Technology
Hungarian University of Agriculture and Life Sciences,
Szent István Campus, Gödöllő, Hungary

.....

Affirmation of supervisor

.....

Affirmation of head of school

CONTENTS

NOMENCLATURE AND ABBREVIATION	5
1. INTRODUCTION, OBJECTIVES	6
1.1. Introduction	6
1.2. Objectives	8
2. LITERATURE REVIEW	9
2.1. Soil strength and structure	9
2.2. Methods of assessing soil strength	10
2.2.1. Cone penetrometer	10
2.2.2. Bevometer technique	12
2.3. Stress distribution in soils under a load	14
2.4. Soil bearing capacity	17
2.5. Pressure–sinkage relationship	19
2.5.1. <i>Some empirical pressure-sinkage model not based on Bernstein- Letoshnev model</i>	22
2.5.2. <i>Developing the conventional pressure- sinkage equations</i>	23
2.5.3. <i>Soil hardpan</i>	27
2.6. Soil compaction	29
2.6.1. <i>Bulk density and moisture content</i>	30
2.6.2. <i>Soil organic matter</i>	31
2.6.3. <i>Tillage operation</i>	32
2.6.4. <i>Mapping of momentary soil properties</i>	33
2.7. Deformation under loading surface	34
2.8. Dimensional analysis	35
2.9. Summary of literature review	36
3. MATERIALS AND METHODS	38
3.1. Bevometer parts design	38
3.1.1. <i>Mechanical structure</i>	38
3.1.2. <i>Control system</i>	40
3.2. Soil preparation	41
3.3. Experimental procedure	42
3.4. Determining moisture content and bulk density of the soil	44
3.5. Confined compression test	45
3.6. Direct shear test	46

4. RESULTS AND DISCUSSION	48
4.1. Effect of finite half-space on the pressure distribution under tire.....	48
4.2. Deformation under pressure plate as a function of depth/ diameter ratio.....	49
4.3. Similarity numbers	51
4.4. Direct shear test	54
4.5. Interaction of the compact zone with the effect of a rigid layer	54
4.6. New pressure–sinkage relationship equation.....	58
4.7. Effect of finite depth on the load bearing capacity factor.....	70
4.8. Generalized pressure-sinkage equation.....	72
4.9. Load bearing capacity increment due to rigid layer interaction.....	72
4.10. Behaviour of soil in shallow layer	74
4.11. New scientific results	76
5. CONCLUSIONS AND RECOMMENDATIONS.....	78
6. SUMMARY	79
7. ÖSSZEFOGLALÁS (SUMMARY IN HUNGARIAN)	80
8. APPENDICES	81
A1: Bibliography.....	81
A2: Publications related to the dissertation	89
A3: Pressure-sinkage curves.....	90
A4: Pressure-sinkage curves with k_{app} curves	94
A5: Relation of Δk and $\Delta(z/D)$.....	97
9. ACKNOWLEDGEMENT	103

NOMENCLATURE AND ABBREVIATION

Symbols

$N_c, N_\gamma,$ and N_q	Bearing capacity factors
b	Smaller dimension of the contact patch
B and c	Constants
c	Soil cohesion
D	Diameter of the loading area
E	Young's modulus
G	Nominal load
H	Soil depth or soil thickness
h	Height of the compacted zone
H/R or H/D	Relative depth
k	Load carrying capacity factor
k_{app}	Apparent sinkage modulus
k_c	Sinkage modulus influenced by soil cohesion
k_ϕ	Sinkage modulus influenced by soil friction angle
$p/\Delta\gamma \cdot D$	Pressure number
R^2	Coefficient of determination
v_k	Concentration factor
z	Sinkage of flat plate
z/D	Relative sinkage
f	Rolling resistance
n	An exponent of deformation

Greek symbols

τ	Shear stress
ρ	Soil density
Π	Dimensionless number
σ	Normal stress
ϕ	Internal friction angle of soil
γ	Unit weight of the soil
ε	Strain

Abbreviations

CI	Cone index
TDCP	Time domain reflectometry sensors
PR	Penetration resistance
DTW	Depth to water index
M.c	Moisture content

1. INTRODUCTION, OBJECTIVES

This chapter presents the background and the importance of the study as well as the objectives of the research.

1.1. Introduction

Off-road vehicles specifically designed to traverse territory void of infrastructure are still utilised in myriad enterprises such as military operations, mining, logging, exploration, construction, recreation, and agriculture, despite the vast majority of transportation of both commodities and passengers occurring over paved roads. Since Second World War, significant attention was placed upon the design of off-road vehicles and their rational development, evidenced by numerous systematic investigations of their fundamental principles (Bekker, 1961; Horiko and Ishigami, 2020).

Terramechanics is the relatively recent nomenclature given to describe the study of an off-road vehicle's performance in the context of its operating environment. Development of terramechanics has accelerated in the last several years due to heightened environmental preservation and energy conservation apprehensions. a particular relevance to terramechanics research is comprehending the effect of the vehicular load on terrain behaviour below it (Wong, 2010).

Vehicle mobility is most significantly impacted when the wheels slip or sink, which is primarily attributed to soil deformation (Jang et al., 2016; Li and Yuan, 2019). limitation on traction impacts machine mobility as a result of the mechanical properties of soil (Taghavifar and Mardani, 2017).

Shearing in the tangential direction and bearing properties in the normal direction form the mechanical properties that soil is often split into. Pressure-sinkage relationship equations identified as being representative of bearing (Ding et al., 2014). Within terramechanics, a vital part is performed by pressure-sinkage relationship. Drawbar pull, thrust, and other performance metrics are ascertained via the resistance and sinkage that, in turn, are calculated through pressure-sinkage models (Meirion-Griffith and Spenko, 2013).

The extent to which soil deformation or stability occur is indicated by the calculations of soil strength in the pressure-sinkage model, thereby demonstrating its pivotal role in assessing soil mechanics (Gao, 2016).

Several models of soil pressure-sinkage have been put forward since the 1950s. Pressure-sinkage models are usually confirmed experimentally by employing flat rigid plates, and the parameters are evaluated according to the results (Ding et al., 2014).

Bekker (1956, 1960, 1969) founded two distinct groups of tests that are known as the bevameter technique. A shear test and a plate penetration test make up the two assessments respectively. In the penetration test, the contact area of the running gear of a vehicle is replicated through the use of a plate of appropriate size, thus, assessing the pressure-sinkage relationship of the terrain (Wong, 2010). The plate penetration test and the shear test assist the predictions of bearing capacity and surface traction respectively (Mason et al., 2020). Janosi (1961) states “the bevameter is the standard method for scientific and engineering exploration of soils and off-road vehicle design”.

The impact on off-road conditions by interactions between vehicles and soil is one area of investigation assisted by the implementation of penetration tests, for the purposes of developing enhanced analytical technique through the data produced (Zelege et al., 2007; Kim et al., 2022).

Bernstein (1913) together with another academic named Goriatchkin, put forward the first and most basic empirical model outlining the pressure-sinkage relationship for terrain. With said model serving as a basis, multiple enhanced models arose later. Circular or rectangular plates were often used in plate-sinkage experiments to determine the parameters. The plate diameter and the sinkage are the sole two variables used within every plate-sinkage equation put forward. Note that these variables follow from Boussinesq theory 1883 for the homogenous elastic half-space in the form:

$$p = \frac{4 E}{\pi (1 - \nu^2)} \frac{z}{D}, \quad (1.1)$$

which can be utilized for viscoelastic-plastic bodies for the homogenous infinite half-space in its widely known form as

$$p = k \left(\frac{z}{D} \right)^n. \quad (1.2)$$

The homogenous infinite half-space is, however, a serious restriction which in the practice is never fulfilled.

To this day, the characterisation of the load bearing capacity of soil, otherwise known as the pressure-sinkage relationship is incomplete. The manner in which the load bearing capacity, which reflects the soil density and thickness of the finite half-space, is impacted by the loading surface diameter provokes a lack of certainty in this area. The equivalent contact diameter of tyres mirror the depth to which agricultural soils are tilled 30-40 cm which, in turn, is the cause for the use of a finite half-space (Sitkei et al., 2019). The homogenous infinite half-space varies entirely with regard to pressure distribution of such soils, as the soil consists of hard layers below and upper layers near the surface. An esoteric piece of information is that there is an extension of the infinite half-space to the finite half-space (Yegorov, 1961). The generalisation of experimental findings regarding load bearing capacity of soils is a significant challenge due to the altering hardness of soil in the finite thickness and the behaviour of the finite half-space.

Analysing the load bearing capacity of soil functioning as a homogenous finite half-space is a research objective of this work. Additionally, an examination of the parameters of pressure-sinkage relationships in distinct scenarios will take place alongside an investigation of the incessantly growing deformation zone throughout the sinkage of the loading plate, the cone-shaped compact zone beneath the loading surface, and the compaction of the soil. Lastly, the manner in which load bearing capacity is impacted by soil depth, loading surface diameter, and soil density will be explored.

1.2. Objectives

A meticulous examination of the effects of deformation from loading upon soil and the issues that finite half-space soil confronts with regard to load bearing capacity form the principal objectives of this work. Through the adoption and implementation of distinct soil thickness levels on sandy loam soil, multiple densities and plate diameters. The mentioned aims are further described below:

- Investigate the compact zone under loading surface defining the transition zone.
- Developing an equation of the load bearing capacity factor k , for expressing the deformation of soil after the transition zone.
- Generalizing the pressure-sinkage equation by taking account the effect of soil density, loading surface diameter and soil thickness.
- Examine the pressure and load bearing capacity of shallow homogenous upper layer.

2. LITERATURE REVIEW

The obstacles, gaps, and findings of the existing literature in the field are investigated in this chapter, taking into consideration recommendations for overcoming such obstacles and the issues previously confronted. Bridging the gaps in the existing literature are among the objectives of this study.

2.1. Soil strength and structure

The structure of soil consists of different components within the three states of matter: dissolved salts components and water make up the liquid; organic matter, primary rock minerals, intergranular cement, and clay minerals make up the solid; and water vapour and air make up the gas. Soil strength is determined by the amalgamation of these elements (Scott, 1994).

Particle size varies between roughly a micron to several millimetres with regard to the solid particles in soil. The particle size usually determines the type of soil. Fig. 2.1 illustrates the European system of stratification of soil in accordance with particle size. This system is generally applicable around the world with only a little variance such as distinct sieve sizes serving as the basis in the USA. Moisture content and particle size are the principal determinants of soil's mechanical behaviour, thereby ensuring that mineralogy, origin, or age are overlooked in favour of particle size for stratification. Additionally, the particular surface area (m^2/g) is linked to the impact of moisture content (Powrie, 2018).

Fine soil				Coarse soil						Very coarse soil		
Clay (Cl)	Silt (Si)			Sand (Sa)			Gravel (Gr)			Cobble (Co)	Boulder (Bo)	Large boulder (LBo)
	F	M	C	F	M	C	F	M	C			
	.002	.0063	.02	.063	.2	.63	2	6.3	20	63	200	630

Size (mm)

F = Fine M = Medium C = Corse

Fig. 2.1. Stratification of soils in line with particle size (Powrie, 2018)

The durability and strength of the soil structure are impacted by the grain size, particle shape, plasticity, void ratio, compressibility, and other properties that diverse kinds of soil and amalgams of particles possess (Whitlow, 1995). A stress state limitation that upon being surpassed leads to a form of failure is what is commonly referred to as strength. Rupture or a plastic flow are examples of significant deformation outcomes following a failure. Shear stress resistance is represented by the soil's shear strength. It is a measure of the resistance of the material to deformation by persistent displacement of its individual particles (Kaliakin, 2017).

Friction and cohesion are the two principal determinants of soil strength. The resistance between soil particles upon sliding over one another is known as friction, whereas two particles bonding is termed cohesion. Heightened quantity of particle contacts per unit volume and grain irregularity typically lead to heightened friction. A soil friction rises upon higher levels of soil bulk density. (Earl, 1996).

Soils are classified into two general varieties: cohesive and frictional, which can be appointed typically to fine-grained and coarse-grained soils, respectively (Eslami et al., 2020). Commonly soils are a combination of both cohesive and frictional as shown in Fig. 2.2 which displays the relation between normal stress and shear strength for different soils (Inns and Kilgour, 1978). In addition, soil may classify as loose and dense soil as shown in Fig. 2.3.

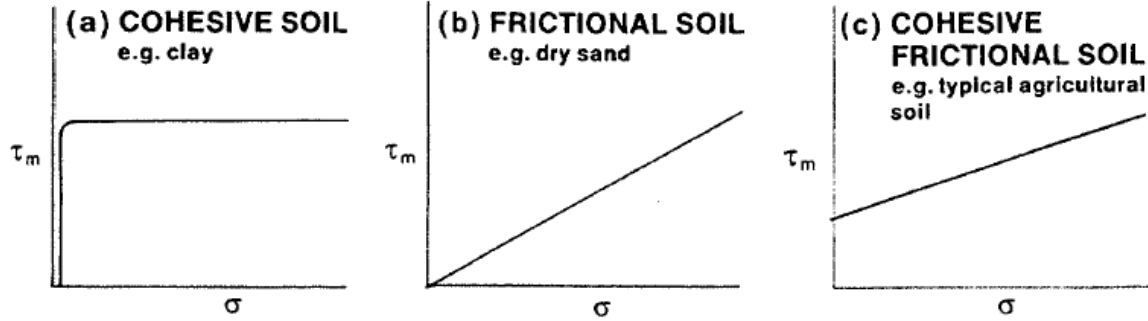


Fig. 2.2. Graphs of soil strength (Inns and Kilgour, 1978)

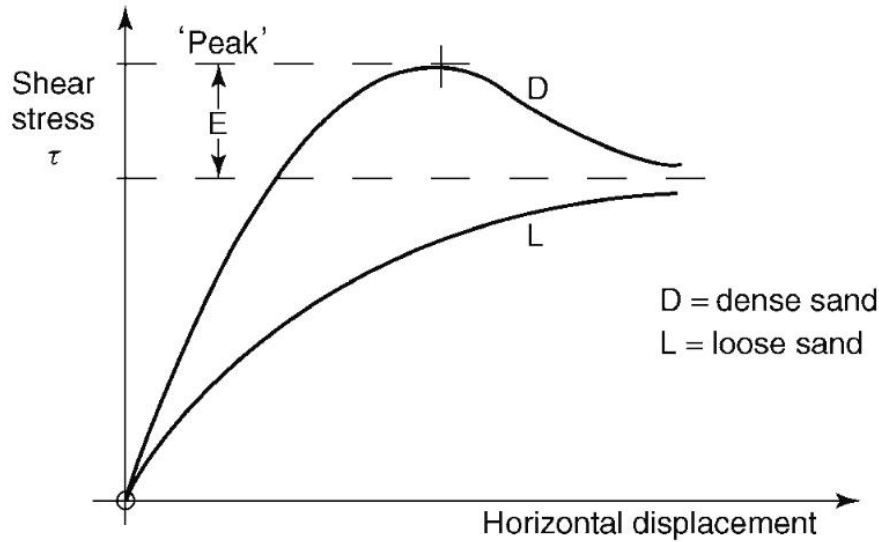


Fig. 2.3. The shear properties of loose and dense sand soils (Head and Epps, 2011)

2.2. Methods of assessing soil strength

To accurately predict motion resistance, gross traction, and other indicators of off-road vehicle mobility, it is vital to accurately assess the strength properties of the terrain. Strength characteristics of soils are estimated by several diverse techniques, two of which include the bevameter and cone penetrometer (Mason et al., 2020).

2.2.1. Cone penetrometer

The instrument created by Mayer, in 1910, serves as the archetype for soil penetrometers in the context of off-road travel (Bernstein, 1913). As far as could be confirmed, a comparable American instrument dates back to Proctor 1933, who used it for civil engineering intents.

The adequacy of soil to sustain multiple ground vehicles is principally determined by the prevalently used cone penetrometer. The soil state can be provided by cone penetrometers based

2. Literature review

on penetration resistance of the cone that relates to shear strength, moisture content, and bearing capacity, and they can be operated to rapidly gather in numerous soil state measurements at different depths and over considerable areas (Goodin and Priddy, 2016)

The Waterways Experiment Station (WES) that were part of the US Army Corps of Engineers created the cone penetrometer technique during the Second World War. Enabling reconnaissance service members to determine whether it was possible or not to traverse terrain through measuring vehicle mobility was the principal function of the device, thereby providing important military intelligence. A 3.23 cm² base area and a 30-degree right circular cone describe the WES-developed cone penetrometer. The acquisition of the cone index is enabled via penetrometer use. The resistance to penetration into the terrain per unit cone base area is signified by this parameter. The cone-terrain interface and its friction and cohesion alongside the compressive and shear properties are also represented by this parameter. Nonetheless, it is challenging to distinguish between the effects of said elements. Off-road vehicle mobility performance of coarse-grained soil, such as sand, and fine-grained soil, such as clay is predicted via the cone index and its inclination regarding penetration depth (Wong, 2010).

A pressure transducer or an analogy dial are used for readout which are paired with a strain gauge or load cell in the measure device itself. Measurements are taken for several sinkage depths after it is pushed into the soil vertically. An example of Cone penetrometer is shown in Fig. 2.4. (Herrick and Jones, 2002).

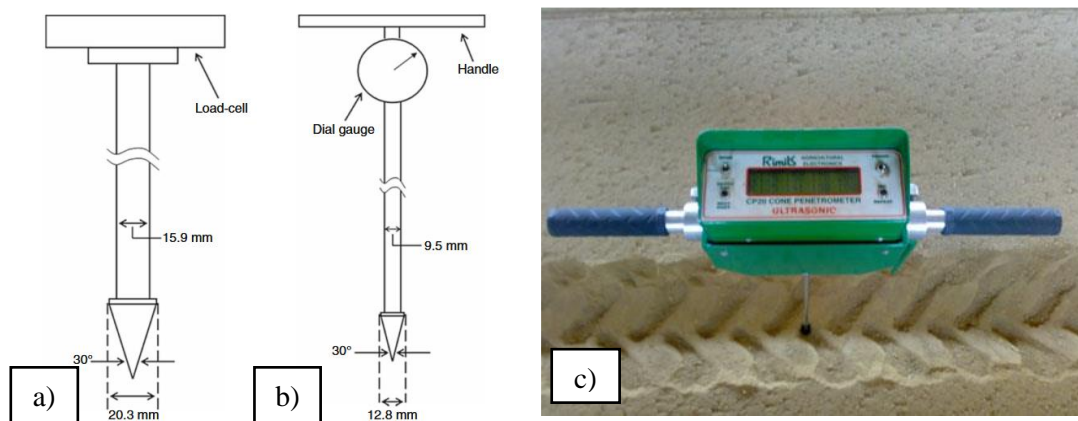


Fig. 2.4. Two prevalently used designs of the soil cone penetrometer: a) Force data measurement enabled by load-cell use; b) A dial gauge and manual design; and c) A cone penetrometer situated in a field (Arriaga et al., 2011; Taghavifar and Mardani, 2017)

The force per unit base area necessary to force the penetrometer through a particular small addition of soil depth is one definition for cone index (CI). Soil strength measurements are influenced by bulk density, water content, and clay content (or texture) of soil (Chung et al., 2013).

Evaluating the compaction quality of soil and observing soil engineering characteristics is carried out in multiple studies via use of the device. Pillinger et al. (2018) employed the cone penetrometer to determine the soil-density distribution in deeper layers of sandy loam soil. S. Gorucu et al. (2006) offered a method for determining the ideal tillage depth through soil cone penetrometer measurements to effectively eliminate the hardpans of soil. Beckett et al. (2018) discovered compaction in ripped agricultural soils through the use of dynamic cone penetrometers. Hernanz et al. (2000) created an empirical model that could attain variables regarding the water

accumulation in the soil profile while also precisely estimating the bulk density of drained loamy soil via cone penetrometer use.

The bulldozing and rolling resistance was ascertained through the application of the cone penetrometer in the study by Máthé et al. (2013). The soil load bearing capacity determines the mentioned resistances. At the point in time when a vehicle goes off-road, entering the terrain in analysis, the initial speed is identified via the soil data and the assessed soil parameter. Máthé and Kiss (2015) used the cone penetrometer to determine rolling losses of a towed vehicle. The Slope compression properties for initial soil water content, organic matter content, and several textures within five soil types served as a function of the cone penetrometer resistance, alongside the precompression stress, in the study by Gao et al. (2012).

Hong et al. (2019) developed a dynamic cone penetrometer incorporated with time domain reflectometry sensors (TDCP) for evaluating the subsurface water content based on the relative permittivity compensated by the ground temperature and for characterizing strength by the penetration index. Soil water for clay and silt-loam soil was used in tandem with CI and dual-sensor penetrometer data to determine soil bulk density in the investigation by Lin et al. (2014). Sastre Jurado et al. (2020) used a lightweight dynamic cone penetrometer test as the basis for collecting field data through a site investigation programme to assess the soil spatial variability.

The lack of complexity in employing the cone penetrometer has led to its prevalent use in vehicle mobility research. To evaluate the mechanical characteristics of terrain for the purposes of locomotion, it is widely acknowledged that the CI by itself falls short of the mark. The soil characteristics under loading conditions can be evaluated by another method, namely the bevameter technique (Wong, 2010).

2.2.2. Bevameter technique

Bekker (1956) developed the bevameter instrument to reproduce the forces undergone by a wheel under typical loading conditions through applying standardized mechanical loads to soil test beds. The shear test and the plate penetration test make up the two kinds of tests frequently undertaken. By utilising a vertical motion displacement transducer and a load cell, the response to pressing a flat plate into the soil with a piston is recorded, thereby indicating the wheel response under a standard load. This process is called the plate penetration (bevameter) test, or more simply, the penetration test.

The penetration test also evaluates the pressure-sinkage relationship of the soil. Through rotation of the terrain surface, the shearing action the vehicle running gear is replicated in the annular shear ring subjected to a preselected standard stress. This process is known as the shear bevameter test. The test measures the corresponding angular and displacement applied torque (Edwards et al., 2017). Janosi (1961) states, “the bevameter is the standard method for scientific and engineering exploration of soils and off-road vehicle design”. The original bevameter is shown in Fig. 2.5. it is constructed at the University of Newcastle upon Tyne and considerably modified at Carleton University (Wong, 2010).

Wills (1964) developed a semiautomatic bevameter where hydraulic pressure is employed to apply torque and an axial load; this allows a single investigator to perform research with a bevameter. Golob developed a bevameter that can accomplish both pressure–sinkage and shear tests through a single hydraulic cylinder and that could storage digital data instead of analogy data. Upadhyaya

et al. (1993) used the bevameter approach by installing a portable machine that was attached to the tractor to estimate the soil sinkage with three rectangular plates. Furthermore, the shear displacement with five various rectangular grouser plates on a loam soil class was studied. Alexandrous and Earl (1995) presented an equipment of hydraulic bevameter that adjusts with the tractor and confirmed that it could indicate the pre-compaction stress of field soils in situ with acceptable accuracy .

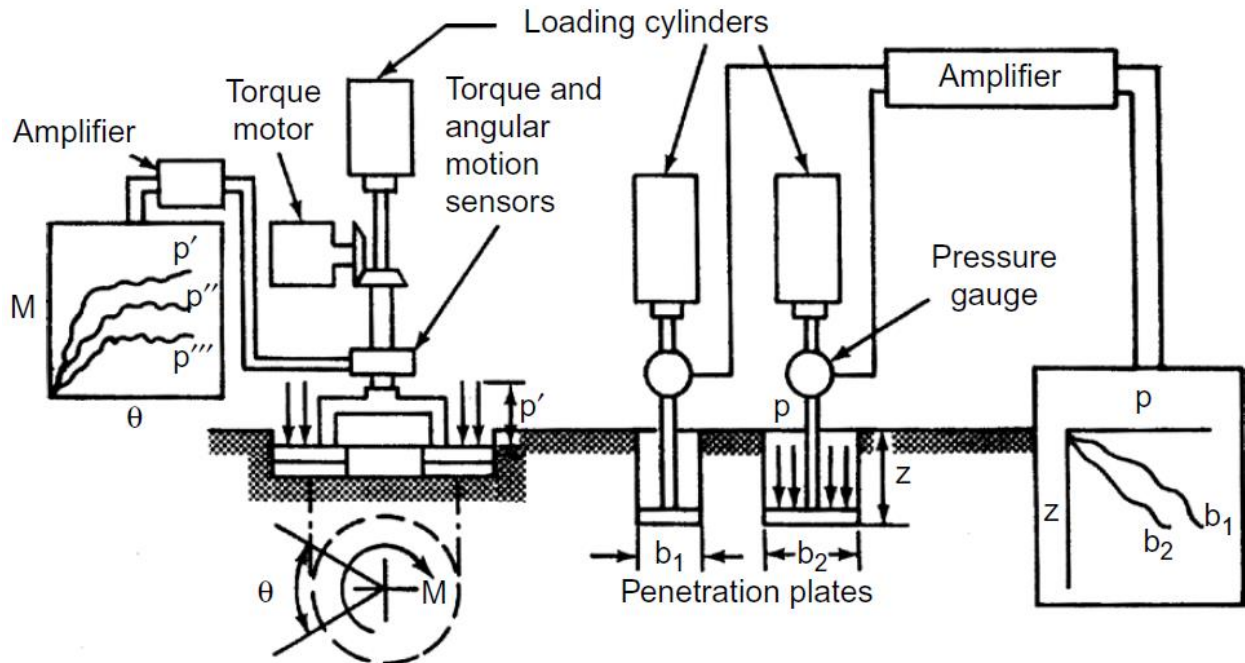


Fig. 2.5. Schematic diagram of a bevameter (Wong, 2010)

Further, Gotteland and Benoit (2002) developed an experimental apparatus named DE CART that was powered by a hydraulic ram and could accomplish penetration tests in the laboratory and in-situ with a diversity of soils (silty sand, sand, and silt) and various plates diameters. Yu (2006) constructed an equipment employing the bevameter technique to acquire the soil parameters needed for the traction modelling based on analytical methods. Lunar soil simulant GRC-1 is assessed via the bevameter made by Oravec (2009) to replicate rover mobility on lunar terrain.

A portable lightweight bevameter design for planetary soils was momentarily exhibited by Apfelbeck et al. (2009). The capacity to undertake multiple parameter evaluations with the same equipment is a key utility feature of the bevameter. Massah and Noorolahi (2010) designed bevameter mounted on a tractor with diverse sizes and shapes (rectangular, circular, and oval) of plates and tested in loam soil field. Mähönen et al. (2021) developed a portable bevameter to estimate the mechanical characteristic of snow, they demonstrated that the bevameter can be used in snow.

The above literature review shows that bevameters have been used for research in diverse fields. Because there is no confirmed standard of instrumentation and equipment, most investigators designed and built their own bevameter to suits their particulars needs.

2.3. Stress distribution in soils under a load

The reclamation of damaged land, amelioration, wind and water erosion, ploughing, excavation, and sealing are among the anthropogenic processes, that in tandem with natural soil development, cause severe alterations in the biological, chemical, and physical properties of soils. The processes known to be most damaging for agriculture are wind and water provoked soil erosion and soil compaction. Soil biodiversity, nutrient export, soil-water household components, soil quality for crop production, buffering and filtering utility of soils are impacted by the multiple alterations to the environment that arise from the combined effect of shear processes and soil compaction that result in soil deformation, heedless of land use (Fig. 2.6) (Horn and Peth, 2011).

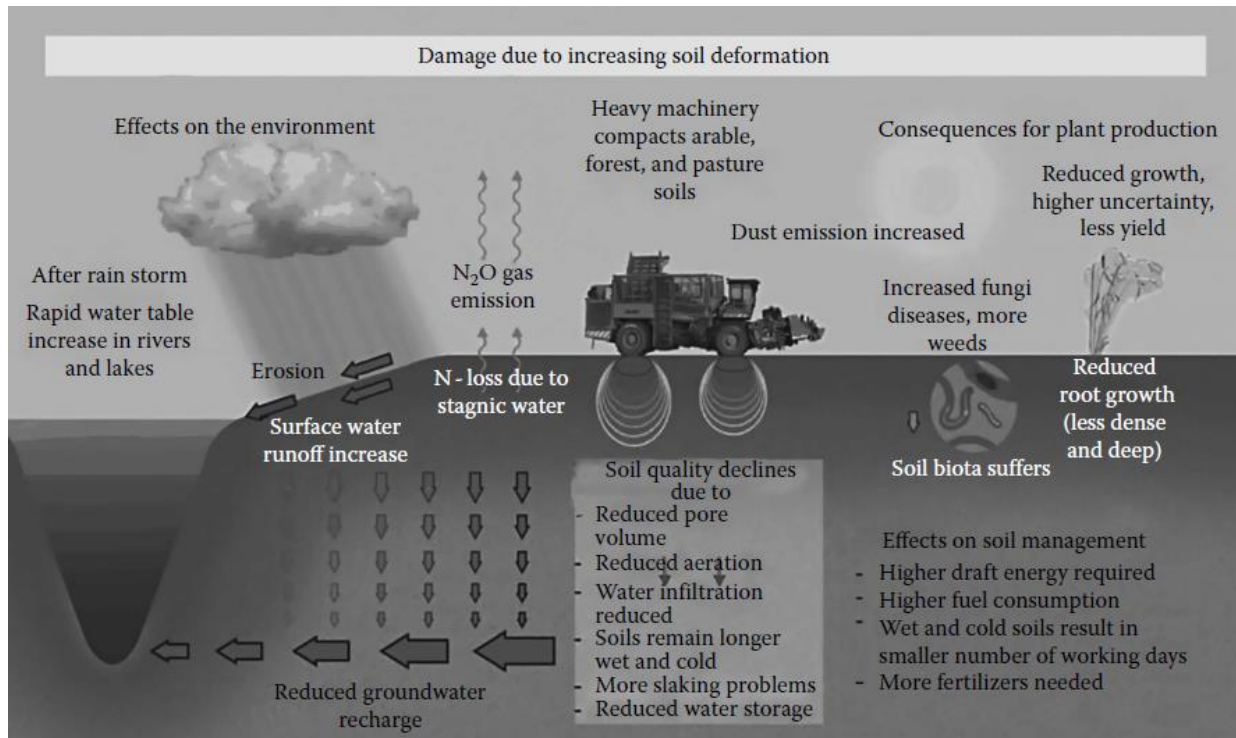


Fig. 2.6. Impact of stress application on soil characteristics (Horn and Peth, 2011)

Soil is recognised as a plastic medium above a specific level of stress and an elastic medium below, thereby being viewed as a semi-infinite elasto-plastic medium. It can then be inferred that vertical stresses at a particular point in the soil are additive and ellipses are signified by stress isobars in a soil loaded under the stress level required for plastic. Thus, heightened size of the loaded area will cause heightened stress in the subsoil within the average ground pressure. Resultantly, while less impact will occur at more significant depths, the risk of soil compaction near the surface of the soil will rise in accordance with heightened ground pressure. Inversely, compaction would heighten intensively at more significant depths when wheel load rises at a particular average ground pressure (Lamandé and Schjønning, 2011).

The work by Boussinesq in 1883 serves as the basis for the theoretical framework regarding the distribution of stresses in the soil. His well-known equation has been developed by Froehlich 1934 to account for different soil stabilities by presenting concentration factor v_k . The mentioned factor ranges between 3 and >5 representing very stable hard soil and unstable soft soil respectively (Wong, 2010).

2. Literature review

By adhering to the principle of superposition, predictions can be made of the stress distribution in a an elastic medium subjected to diverse loading forms. Pressure bulbs, a frequently used nomenclature used for a family of iso-stress lines, as demonstrated in Fig. 2.7, serve as a representation of the distribution of stresses in a semi-infinite elastic medium subjected to the action of a tracked vehicle. Roughly half of the pressure is exerted by the track on the surface, represented by the vertical stress below the centre of the loading area. It decreases at a depth equivalent to twice the track width. an inclined angle of 45° with the horizontal describe the limits of the vertical pressure bulbs (Söhne, 1953; Wong, 2010).

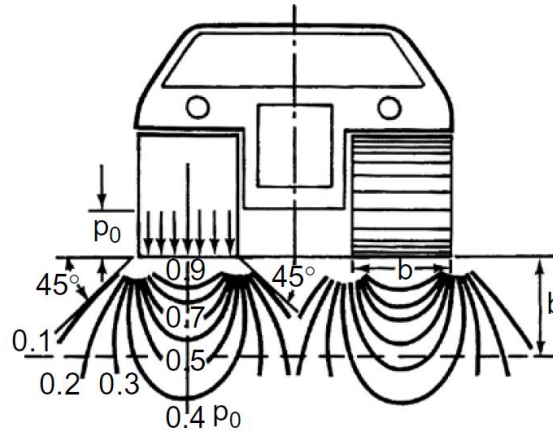


Fig. 2.7. Vertical stress distribution in a semi-infinite elastic medium subjected to a tracked vehicle (Wong, 2010)

Alterations in the functions of soil can occur from stress-induced deformation caused by the use of agricultural machinery in transmitting stress in the soil. This highlights the significance of comprehending stress transmission, particularly for two reasons: to comprehend cause and effect, which in this case is mechanical loading transmitting soil stress and the effect being alterations in soil pore functionality; and second to avert soil compaction by generating decision support tools and predictive model for land users (Keller et al., 2014).

Upon soil strength, or soil mechanical resistance being surpassed by soil mechanical stress, soil compaction takes place. Resultantly, elevating soil strength or diminishing soil stress help mitigate the risk of soil compaction. In practice, it is much easier to handle the soil stress caused by the vehicle running over the soil than to control soil strength, which is greatly affected by soil structure, soil matric potential, and soil root interactions. The soil stress can be mitigated by either decreasing the load or by raising the agricultural machinery contact area (Keller and Arvidsson, 2016).

Within the soil volume, intensive variance in stress propagation and the stress path at the surface layer of the soil are impacted by the type of stress application, such as rubber belt tire-inflation pressure or tire, that regulate the impact of speed in wheeling. In line with the Boussinesq theory in 1883, Horn and Peth (2011) demonstrate, as Fig. 2.8 portrays, that stresses are transmitted at greater depths for increased ground contact pressures at a particular contact area, and that the greater the contact area, the deeper the stress propagation at a particular surface load.

A plastic flow is provoked when a minute increase in stress generates a swift rise in strain upon the specific threshold being surpassed by the load that the soil surface is subjected to. Plastic equilibrium is that state used to describe the stage immediately before the plastic flow. The failure

2. Literature review

of the soil can be demonstrated by the transition to a plastic flow from a state of plastic equilibrium (Wong and Asnani, 2008).

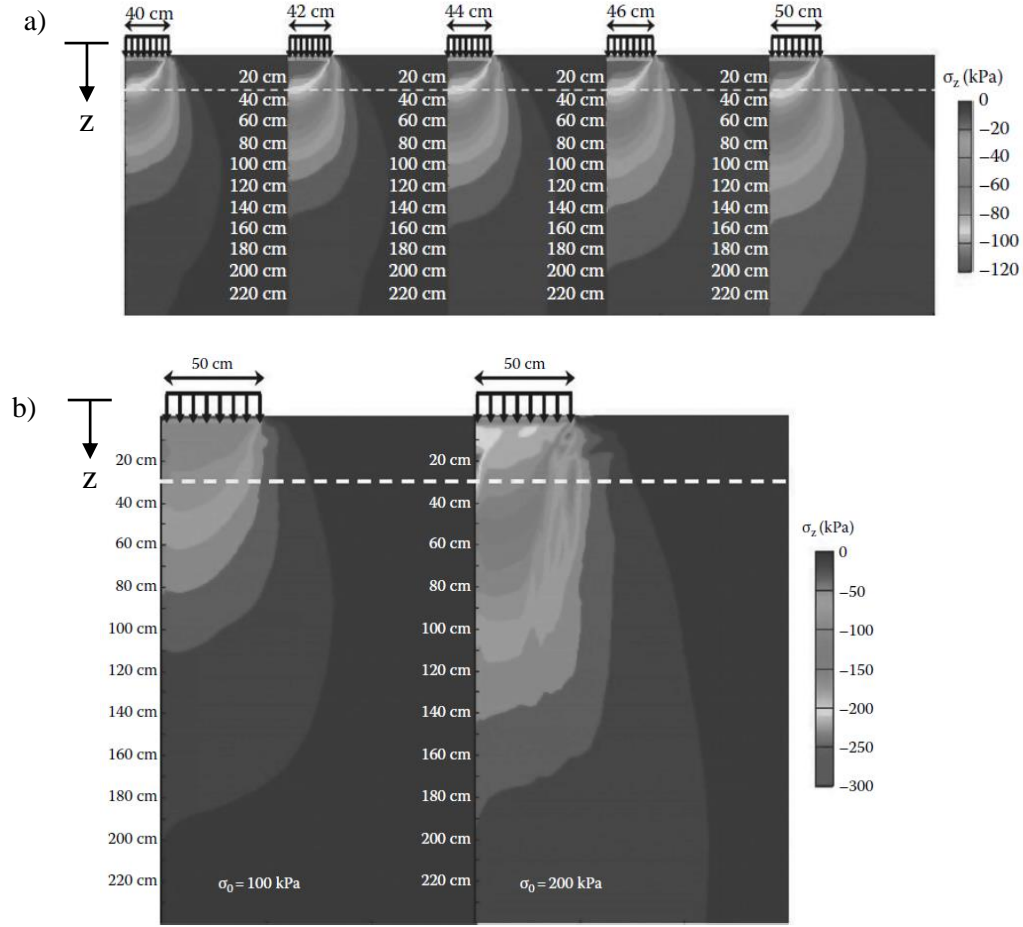


Fig. 2.8. Stress distribution under a tire a) Tire size increases from left to right, representing the increasing contact area, while the ground contact pressure (100 kPa) remains the same; b) Increased wheel load causes a higher ground contact pressure (σ_0) while the tire size (100 cm diameter) remains the same. The typical ploughing depth of 30 cm is represented by the horizontal, white-dashed line (Horn and Peth, 2011)

Among the most prevalent failure criterion for soil is the Mohr-Coulomb criterion, outlining the parameters for failure of the soil material in the plasticity area. When the shear stress adheres to the equation below, it is presumed that the soil will fail:

$$\tau = c + \sigma \tan \phi. \quad (2.1)$$

The angle of internal friction of the material is represented by ϕ , the standard stress on the shearing surface is indicated by σ , cohesion is signified by c , and shear stress is represented by τ .

The Mohr circle of stress elucidates the significance behind the Mohr-Coulomb failure criterion. Fig. 2.9 illustrates that a Mohr circle can be made upon there being a distinct state of stress on the sample of a terrain for every mode of failure. By drawing straight lines around the group of Mohr circles, where the incline of the straight line signifies the angle of the internal shearing resistance and where it meets with the shear stress axis represents the cohesion of the terrain. The failure may occurs at the point where the enveloping line crosses with a Mohr circle signifying a state of stress at a given point in the terrain (Wong, 2010).

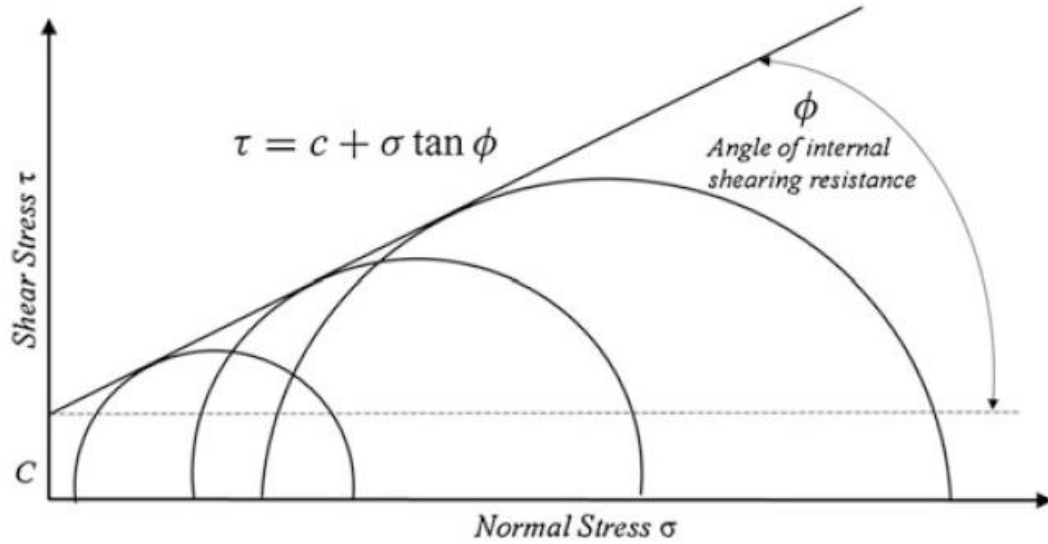


Fig. 2.9. Within a plastic region, the Mohr-Coulomb failure criterion (Taghavifar and Mardani, 2017)

2.4. Soil bearing capacity

The ability to support the loads exerted on the ground is called the bearing capacity. The maximum mean contact pressure between soil that does not generate a shear failure and the foundation represents the bearing capacity of soil. Terzaghi (1943) describes the theoretical maximum pressure that can be applied before failure of soil material as being the ultimate bearing capacity

A uniform soil layer that encompasses a great depth serves to help identify the bearing capacity of a rigid, shallow, continuous, and rough footing in Terzaghi's comprehensive theory. Moreover, When the width B is less than or equal to its depth D , the foundations is said to be a shallow foundation. Fig. 2.10 illustrates the presumed failure surface within the soil when subjected to the ultimate load.

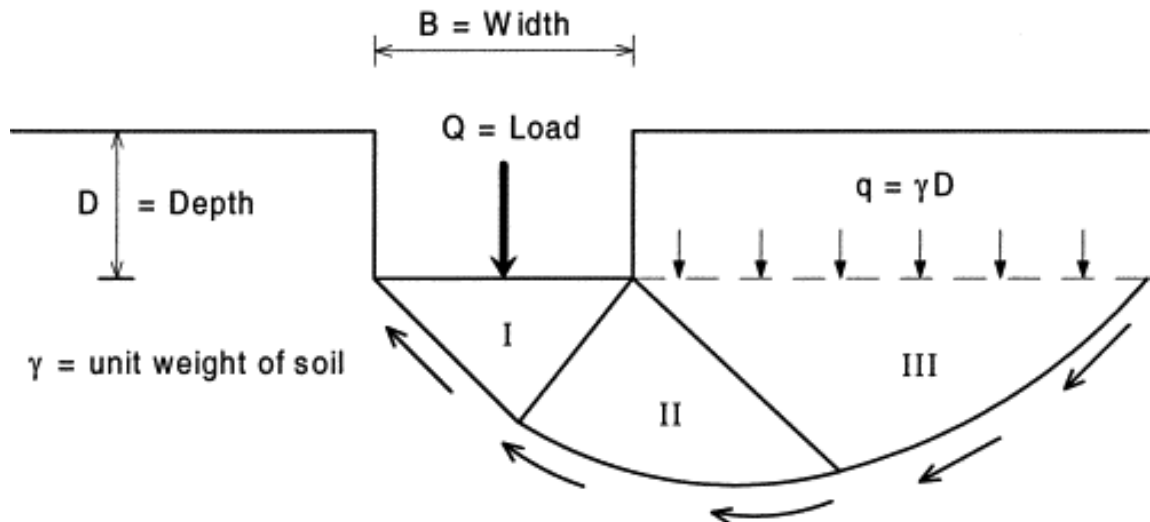


Fig. 2.10. Overall description of bearing capacity (Kulhawy and Hirany, 2003)

When the foundation is presumed to be of infinite length, the shear surface enables the calculation of the general shear mode's ultimate bearing capacity, as demonstrated in Fig. 2.9. The active Rankine zone (I) an elastic zone situated directly under the bottom of the of the footing, (II) a

radial Prandtl zone, and a passive Rankine zone (III) make up the three optimum zones respectively in the rigid-plastic medium that the shear surface soil is presumed to be (Kulhawy and Hirany, 2003). The bearing capacity of Terzaghi shown in Eq. 2.2:

$$p = cN_c\lambda_c + \frac{B}{2}\gamma N_\gamma\lambda_\gamma + \gamma N_q\lambda_q z, \quad (2.2)$$

where z is the normal distance between the place where the plate rests and the soil top surface (footing depth), c is the soil cohesion, γ is the soil unit weight, λ_c , λ_γ , and λ_q are the plate shape coefficients, and N_c , N_γ , and N_q are the bearing capacity factors which are processes of soil friction angle ϕ (Das, 2017; He et al., 2019).

It is relevant to state that loose standard soil does not align with Fig. 2.9 whose standard zones only apply to rigid bodies

Various parameters have been operated to evaluate soil bearing capacity and soil susceptibility for plastic deformation. Constitutive soil properties, which are indirectly related to soil strength, like organic matter, texture, bulk density, structure, as well as soil moisture status, have been utilized as categorizing parameters to qualitatively indicate stability of soil (Alakukku et al., 2003).

The presumption that thicknesses of the bearing stratum is infinite permeates convention theories regarding bearing capacity and shallow foundation's ultimate capacity. The unit load that the soil supports can be severely impacted by the presence of a hard layer at a particular depth under the foundation. Thus, the original bearing capacity models should be adjusted to account for this state in specifying the ultimate bearing capacity (Cerato and Lutenecker, 2006).

Yegorov (1961) suggested model for the stress and displacement of finite thickness foundation of homogenous soil (the stress distribution under a circular plate caused by a rigid layer at a certain depth shown in Fig. 2.11).

This model is applicable primarily to study the deformation of a soil layer underlain by hard layer without compaction. The model showed that deformations under the foundations, even without the underlying hard layer, are concentrated in the upper part of the massif and do not extend deeply. As a result of this, a so-called active zone is formed, within which the base is practically deformed. The core depth problem is extremely important in the practice of calculating the base of finite thickness. It can be resolved only experimentally based on measurements of layer-by-layer deformations of the building soil.

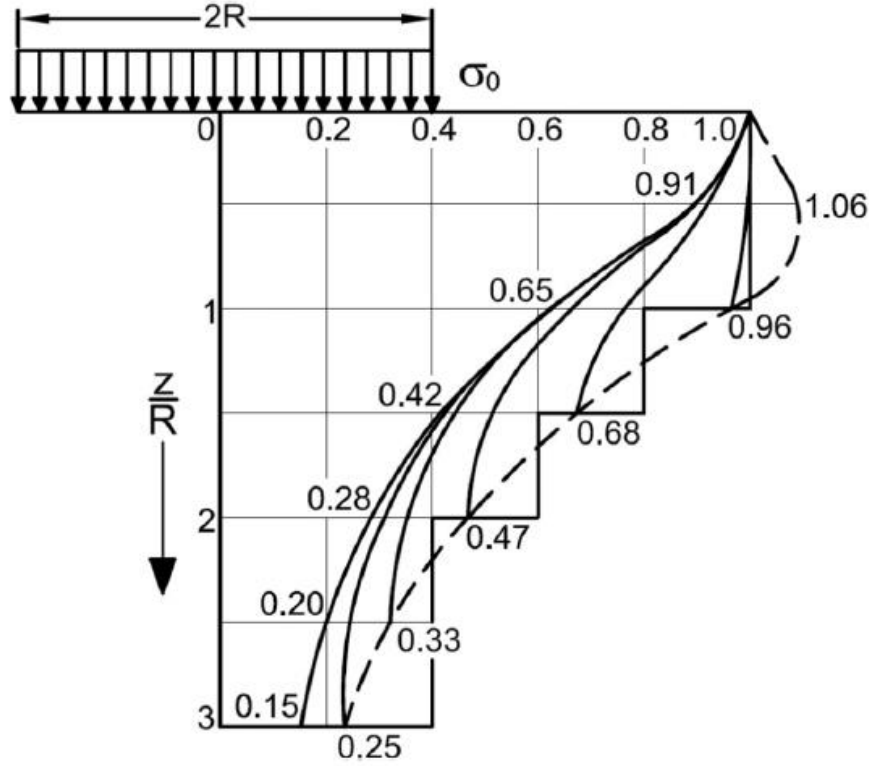


Fig. 2.11. A rigid layer at a particular depth triggers distortion of stress distribution beneath a circular plate (Sitkei, 1972, after Yegorov)

2.5. Pressure–sinkage relationship

Shearing in the tangential direction and bearing characteristics in the standard direction characterises the manner in which the mechanical properties of soils are split into. The pressure-sinkage relationship equations identified as being representative of bearing (Ding et al., 2014). Upon a particular pressure from a given pressure source being exerted upon soil, the sinkage is measured by pressure-sinkage models. The pressure can be transferred through different sources such as a rectangular plate, circular plate, or a certain running gear, such a wheel or tire (He et al., 2019). Assessing the mobility and traction of vehicles on terrain lacking infrastructure is aided greatly by the pressure-sinkage relationship (Kiss, 2003; Chen et al., 2020).

Plastic deformation and elastic deformation make up the two components involved in the sinkage process. Minute loads lead to the occurrence of plastic deformation. Thus, outlining the sinkage properties of soil with the same model is challenging. Simplified models are usually employed in research of terramechanics (Yang et al., 2018)

Numerous efforts have been made to improve empirical models that describe the pressure-sinkage relationship. Presuming that the soil is homogeneous from the surface till the depth of interest.

The first, ancient and experimentally confirmed pressure-sinkage relationship suggested by Bernstein in 1913 which finalize that if a plate penetrate to depth (z) beneath pressure (p) then an empirical curve $p(z)$ possibly fitted with Eq. 2.3 (Bekker, 1969)

$$p \cong kz^{0.5}, \quad (2.3)$$

where 0.5 is the sinkage exponent and k is inelastic deformation modulus.

2. Literature review

Eq. 2.3 was later modified when Letoshnev (Russian investigator) found that the formula could be generalized as shown in Eq. 2.4

$$\begin{aligned} dp &= knz^{n-1}, \\ p &= kz^n. \end{aligned} \quad (2.4)$$

The coefficient of ground deformation (kg/cm^{n+2}) is represented by k , which in both equations aforementioned was significantly impacted by the kind of test plate, and n was indicated by a value between one and zero.

Using D as the diameter of the loading area, the use of the dimensionless value $\lambda = z/D$ instead of z was suggested by Saakyan 1956 (He et al., 2019). Eq. 2.5 portrays the pressure-sinkage relationship for a circular plate:

$$\begin{aligned} dp &= \frac{k}{D^n} n z^{n-1}, \\ p &= k(\lambda)^n = k \left(\frac{z}{D} \right)^n. \end{aligned} \quad (2.5)$$

The impact of the angle of internal shearing resistance and the impact of soil cohesion are made into discrete parts by Bekker, as seen in Eq. 2.6. Additionally, Bekker (1969) considers, as illustrated in Eq. 2.6, the geometry of the contact patch:

$$p = \left(\frac{k_c}{b} + k_\phi \right) z^n, \quad (2.6)$$

where b is the contact patch smaller dimension, k_c is a sinkage modulus affected by soil cohesion, and k_ϕ is a sinkage modulus impacted by soil friction angle, z is flat plate sinkage, and $n \in \mathbb{R}^+$ is a deformation exponent.

A drawback of this model is that the dimensions k_c and k_ϕ are dependent upon the value of n . In the scenario where experimental data is inaccessible, the model offers the optimum method for forecasting patterns for an ample scope of soils regarding their resistance to penetration, as demonstrated by the relative precision of Eq. 2.6. The values of z and p are measured whereas the parameters k_c , k_ϕ and n are derived by means of fitting empirical data to Eq. 2.6 (Wong, 2001).

Reece constructed two models, portrayed in Eqs. 2.7 and 2.8 where the latter was designed for highly compact soils, for pressure-sinkage. The value of the sinkage component is independent from the dimension of the model parameters in Eq. 2.6, while dimensionless parameters characterise Eq. 2.8 (Reece, 1965; Onafeko and Reece, 1967)

$$p = (k_1 + bk_2) \left(\frac{z}{b} \right)^n, \quad (2.7)$$

$$p = (c\hat{k}_c + \gamma b\hat{k}_\phi) \left(\frac{z}{b} \right)^n. \quad (2.8)$$

The unit weight of the soil is indicated by γ , soil cohesion is represented by c , and the model parameters are signified by k_1 and k_2 .

Wong suggests that distinctive parameter readings can be acquired via a weighted least squares technique, thereby providing \hat{k}_ϕ , \hat{k}_c , \hat{k}_c , \hat{k}_c , and n values (Wong, 2010). Wong's technique for data

2. Literature review

processing derives the best-fitted values of terrain parameters of the pressure-sinkage by minimizing the subsequent function utilizing a weighting factor p^2 ,

$$F = \sum p^2 (\ln p - \ln k_{eq} - n \ln z)^n, \quad (2.9)$$

where: $k_{eq} = \frac{k_c}{b} + k_\phi$

The equations below are generated by minimising the value of function F via taking two partial derivatives of F where one applies to k_{eq} and the other to n .

$$\ln k_{eq} \sum p^2 \ln z + n \sum p^2 (\ln z)^2 = \sum p^2 \ln p \ln z, \quad (2.10)$$

$$\ln k_{eq} \sum p^2 + n \sum p^2 \ln z = \sum p^2 \ln p. \quad (2.11)$$

The acquisition of $\ln k_{eq}$ and n values are enabled by solving such equations

$$n = \frac{\sum p^2 \sum p^2 \ln p \ln z - \sum p^2 \ln p \sum p^2 \ln z}{\sum p^2 \sum p^2 (\ln z)^2 - (\sum p^2 \ln z)^2}, \quad (2.12)$$

$$\ln k_{eq} = \frac{\sum p^2 \ln p - n \sum p^2 \ln z}{\sum p^2}. \quad (2.13)$$

When employing two different plate sizes, a unique n is usually acquired for each. Thus, it is needed to use the average of n -values that resulting from two different plates when computing the natural logarithm of k_{eq} in Eq. 2.13. Regardless, there will be two k_{eq} values: one for bigger plate (b_1) and the other from smaller plate (b_2). Consequently, the values of k_c and k_ϕ can be specified using the following equations (Dewhurst, 1964).

$$k_c = \frac{(k_{eq})_{b_1} - (k_{eq})_{b_2}}{b_2 - b_1} b_1 b_2, \quad (2.14)$$

$$k_\phi = (k_{eq})_{b_1} - \frac{(k_{eq})_{b_1} - (k_{eq})_{b_2}}{b_2 - b_1} b_2. \quad (2.15)$$

Determining the error between the theoretical data and the experimental data was enabled by technique made by Wong. As demonstrated in Eq. 2.16, the method outlines the ratio of root mean square error to the average value of pressure and is known as the goodness-of-fit equation.

$$\varepsilon = 1 - \frac{\sqrt{\frac{\sum (p_m - p_{lc})^2}{N-2}}}{\frac{\sum p_m}{N}}. \quad (2.16)$$

The number of data points utilised for the curve fitting is represented by N , the computed pressure using the aforementioned processes is indicated by p_{lc} , and the measure pressure is represented by p_m the fit is perfect if ε is 1.

It is noteworthy that similar goodness-of-fit findings are produced when the Reece or Bekker equations are used with the same pressure-sinkage data. Moreover, equivalent values of n are found. The radius of the plate or smaller dimension represented by b is constant for a given set of data, which, in turn, produces these equivalent results. Resultantly, equivalent forms can be found in the two mentioned equations. Identical predictions of the pressure for a specific loading plate at a particular sinkage will not be generated by the two equations. The goodness-of-fit to the recorded

2. Literature review

data in the Reece and Bekker equations alongside the average values of n , k_c'' , k_c , k_ϕ'' , and k_ϕ for several mineral terrains assessed are summated in Table 2.1.

Table 2.1. Average values of the parameters encapsulating the pressure-sinkage relationships of several mineral terrains (Wong, 2010)

Terrain type	Constants for Bekker's equation			Constants for Reece's equation			Goodness-of-fit %	Wet density (kg/m ³)	Moisture content %
	n	k_c (kN/m ^{$n+1$})	k_ϕ (kN/m ^{$n+2$})	n	k_c'' (kN/m ²)	k_ϕ'' (kN/m ³)			
LETE sand	0.705	6.94	505.8	0.705	39.1	779.8	95.3	~1600	
	0.611	1.16	475.0	0.611	28.2	1066	94.5		
	0.804	3.93	599.5	0.804	16.9	879.6	93.8		
	0.728		1348	0.728	18.3	2393	88.8		
	0.578	9.08	2166	0.578	197	4365	89.2		
	0.781	47.8	6076	0.781	229.7	8940	89.8		
	0.806	155.9	4526	0.806	413.5	5420	88.1		
Upland sandy loam	1.10	74.6	2080	1.10	42.0	1833	87.7	1557	51.6
	0.97	65.5	1418	0.97	77.4	1464	92.0	1542	49.2
	1.00	5.7	2293	1.00	5.3	2283	94.8	1570	49.1
	0.74	26.8	1522	0.74	121.7	2092	95.1	1519	44.3
	1.74	259.0	1643	1.74	-0.9	763	86.0	1696	50.0
	0.85	3.3	2529	0.85	42.4	3270	87.5	1471	28.6
	0.72	59.1	1856	0.72	231.4	2323	84.2	1592	34.3
	0.77	58.4	2761	0.77	214.1	3626	86.6	1559	35.1
	1.09	24.9	3573	1.09	6.7	2982	91.9	1716	31.2
	0.70	70.6	1426	0.70	279.3	1317	94.3	1470	27.3
	0.75	55.7	2464	0.75	213.6	3244	89.4	1526	32.6
Rubicon sandy loam	0.66	6.9	752	0.66	63.3	1176	92.6	1561	43.3
	0.65	10.5	880	0.65	88.2	1358	97.0	1588	44.2
North Gower clayey loam	0.73	41.6	2471	0.73	121.2	-4.2	88.8	1681	45.8
	0.85	6.8	1134	0.85	27.0	1430	90.0	1597	52.0
Grenville loam	1.01	0.06	5880	1.01	-1.3	5814	87.4	1326	24.1
	1.02	66.0	4486	1.02	55.3	4292	89.1	1339	18.2

2.5.1. Some empirical pressure-sinkage model not based on Bernstein- Letoshnev model

With a focus on track-clay interaction, Evans put forward an empirical pressure-sinkage model involving moist soil with low bearing capacity (Evans, 1953).

$$p = 8.82 c \left(1 - \exp \left(\frac{-K \cdot z}{b} \right) \right). \quad (2.17)$$

The empirical model parameter is indicated by K , the track width is signified by b , and the clay cohesion is represented by c .

With the experimental pressure-sinkage curve serving as the basis, a semi-empirical hyperbolic law depicting the pressure-sinkage relationship of soil was founded by Korchunov. Kacigin and Guskovt (1968) note, as illustrated in Eq. 2.18, the characteristic of the pressure-sinkage curve at large sinkage where the bearing capacity of the soil is signified at the point where the pressure

draws close to an asymptote, alongside the characteristic of the pressure-sinkage curve at small sinkage, potentially signified by a linear function, are considered in this model.

$$p = p_0 \frac{1 - \exp\left(\frac{-2k \cdot z}{p_0}\right)}{1 + \exp\left(\frac{-2k \cdot z}{p_0}\right)}. \quad (2.18)$$

The coefficient of volumetric compression and the bearing capacity of the soil are represented by k and p_0 respectively.

As Eq. 2.19 portrays, an empirical sinkage-pressure model for circular plate-soil interaction was put forward by Gottenland and Bonoit (2006).

$$p = \left(\frac{C_m}{B^m} + \frac{s_m}{B^{1-m}} z \right) + \left(1 - \exp \left[-\frac{s_0}{C_m} \frac{z}{B^{1-m}} \right] \right). \quad (2.19)$$

The model parameters are represented by m , s_0 , C_m , and s_m while the plate diameter is indicated by B .

The soil types of frictional cohesive soil (silty sand), cohesive soil (silt), and frictional soil (sand), are used alongside three circular plates of diameters of 0.15, 0.1, and 0.05 m in the penetration soil test that proves Eq. 2.19. A compound function involving an exponential function of sinkage z and a linear function of sinkage z generate the model. The linear sinkage-pressure relationship for the plastic and elastic zone of the sinkage-pressure plot alike are depicted by the initial linear function. The exponential term and the second compound function represent the transition to the plastic zone from the elastic zone. The plastic and elastic behaviours of the soil are disassociated via the presence of two distinct asymptotes in the model for each of the zones respectively.

Pressure was found to be incapable of heightening sinkage at deeper depths while soil resistance to sinkage rose in tandem with rises in pressure, thus making the hyperbola a more accurate depiction of the relationship between sinkage and load (Kogure et al., 1983). In addition, instead of furthering the theory of plasticity and elasticity, an appropriate description of this procedure can be attained more effectively via the adoption of semi-empirical methods.

Emori and Schuring (1966) presented that the force needed to push a plate in the penetration test was a function of plate velocity (\dot{Z}), penetration depth (Z^\otimes), and plate acceleration (\ddot{Z}) as shown in Eq. 2.20

$$F_s = f_1(Z^\otimes) + f_2(Z^\otimes, \dot{Z}) + f_3(Z^\otimes, \ddot{Z}). \quad (2.20)$$

The soil force exerted on the plate is represented by F_s . The static force identified as the force provoked by lateral acceleration of soil viscosity and particles. The inertia force of vertically accelerated soil particles to be represented by the first, second, and third terms respectively.

2.5.2. Developing the conventional pressure-sinkage equations

The findings of bevameter tests and dimensional analysis (DA) serve as the bases for the novel pressure-sinkage model demonstrated in Eq. 2.21 (Lim et al., 2021). As a result of decreasing physical quantitative parameters, said model was suggested via the implementation of dimensional analysis. To attain an accurate pressure-sinkage relation, a novel bevameter was constructed. Three

2. Literature review

distinctly sized flat plate diameters of the bevameter were used in the generation of the novel pressure-sinkage model.

$$p = \rho_{soil} g b \left(\frac{z}{b(\alpha b + \beta)} \right)^{\frac{1}{n}}. \quad (2.21)$$

The model parameter is represented by α and β , the gravitational acceleration is indicated by g , pressure is signified by p , and sinkage and soil density are represented by z and ρ respectively

To meet the intensive requirements of autonomous wheeled vehicles, highly accurate models for terrain classification were developed by Ding et al. (2014) enabling the impacts of slips in pressure-sinkage relation, running gear or plate dimension, or normal load to be mirrored. Eq. 2.22 portrays the form of such model.

$$p = K_s z \lambda_N. \quad (2.22)$$

The dimensionless function, as illustrated in Table 2.2, and the sinkage modulus of the terrain in units of Pa/m are represented by λ_N and K_s respectively.

Slip, normal load, sinkage, and other motion state parameters alongside width, radius, and other running gear or plate parameters form part of the dimensionless function λ_N . The experimental pressure-sinkage data and the kind of soil determine the expression of the dimensionless function, hence performing a vital part with regard to model precision.

Table 2.2. Expressions of the dimensionless function λ_N (Ding et al., 2014)

Cases	λ_N	Notes
Sinkage exponents > 0.3	$\lambda_N = \left(\frac{z}{z_0} \right)^{n_0 - 1 + n_1 \left(\frac{z}{z_0} \right)}$	$z_0 = 1\text{m}$, and n_0 and n_1 are the function parameters.
Sinkage exponents < 0.3 (the plastic phase begins at small sinkage)	$\lambda_N = \left(\frac{z}{z_0} \right)^{n_0 - 1 + n_1 r}$	r is the radius of the circulate plate.
Normal loads $< 7000\text{ N}$.	$\lambda_N = \left(\frac{z}{z_0} \right)^{n_0 - 1 + n_1 r + n_2 r^2}$	$r = 25.4\text{ mm to } 152.4\text{ mm}$
Normal load (W)	$\lambda_N = \left(\frac{z}{z_0} \right)^{n_0 - 1 + n_1 W + n_2 W^2}$	

As illustrated in Eq. 2.23, the Bekker model was altered to better investigate how the pressure - sinkage of compaction soil is impacted by wheel diameter, leading to a pressure-sinkage model designed to focus upon wheel-soil interaction (Meirion-Griffith and Spenko, 2011).

$$p = \hat{K} z^{\hat{n}} D^{\hat{m}}. \quad (2.23)$$

The diameter exponent and the wheel diameter are represented by \hat{m} and D respectively. The fitting constants of $D^{\hat{m}}$, $z^{\hat{n}}$, and \hat{K} help outline the power function in the suggested model, alike to the expression by Bernstein-Goriatchkin.

2. Literature review

Three kinds of soil and between 0.1 and 0.3 m sized five-wheel diameters were used in over 150 experiments, whose findings prove the efficacy of the alteration. The curvature of the pressure-sinkage relationship as a function of diameter and sinkage alike was guaranteed via the incorporation of $D^{\hat{m}}$ in the mentioned model. As illustrated in Fig. 2.12, a vehicle-terrain testbed was utilised to prove experimental accuracy.

Meirion-Griffith and Spenko (2013) then incorporated wheel width into the model, enabling analysis of a small-diameter wheel on compacted soil, as demonstrated in Eq. 2.2:

$$p = \hat{K} z^{\hat{n}} (bl)^{\hat{m}}, \quad (2.24)$$

$$l = \sqrt{(Dz_0 - z_0)}. \quad (2.25)$$

The maximum wheel sinkage, horizontally projected length of the wheel-soil contact patch, and the wheel width are represented by z_0 , L , and b respectively.

The soil strength parameters alongside the form and size of the plate utilised were found to impact the precision of the plate sinkage analysis (Youssef and Ali, 1982). Replicating the context of being beneath a wheel or track was enabled by a constant plate penetration rate performed at speed, which were conditions thought to be necessary to acquire more accurate findings. Nonetheless, in the attempt to replicate traffic, using a very high loading rate made the application of the load challenging. The similarity between rectangular and circular sinkage plates was validated by the findings. Youssef and Ali put forward Eq. 2.26 via the alterations made to the Reece and Bekker models:

$$p = (K_1 + 0.5bK_2)\beta^n Z^n. \quad (2.26)$$

As illustrated in Table 2.3, the geometric constant contingent upon the shape of the loading surface is represented by β (Youssef and Ali, 1982).

The rise in area as a function of sinkage could only be indicated via the use of several plates if the plate dimensions were altered to fit the wheel-soil contact patch. Hence, a novel wheel diameter and a plate test at every sinkage level would be required.

Eq. 2.27 demonstrates that the modulus of soil deformation was equal to $K_0 \dot{Z}^m$ in Bekker's equation and that soil surface sinkage diminished at elevated penetration velocities when subjected to a contact load, as per Grahn (1991).

$$p = K_0 \dot{Z}^m Z^n. \quad (2.27)$$

The exponent of the penetration velocity, the static modulus of soil deformation, and the vertical velocity are represented by (m) , (K_0) , and (\dot{Z}) respectively.

The data for distinct load speeds is illustrated in Fig. 2.13. As Grahn observes, penetration speeds lower than 10 mm/min invalidate that dynamic relation, otherwise known as a static condition.

Table 2.3. Plate geometric constants, β vs. A/S (Youssef and Ali, 1982)

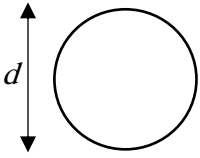
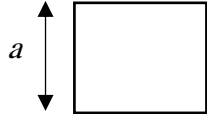
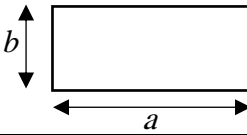
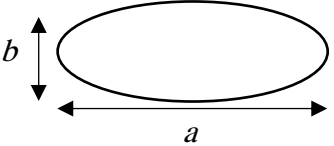
Plate shape	A/S	β_o
Circular 	$d/4$	4
Square 	$a/4$	4
Rectangular 	$\frac{a \cdot b}{2(a + b)}$	$\frac{2}{a}(a + b)$
Ellipse 	$\frac{a \cdot b}{2(a + b)}$ Min. $\frac{a \cdot b}{4\sqrt{\frac{1}{2}}(a^2 + b^2)}$ Max.	$\frac{2}{a}(a + b)$ Max. $\frac{4\sqrt{\frac{1}{2}}(a^2 + b^2)}{a}$ Min.



Fig. 2.12. Single-wheel vehicle-terrain testbed (Meirion-Griffith and Spenko, 2011)

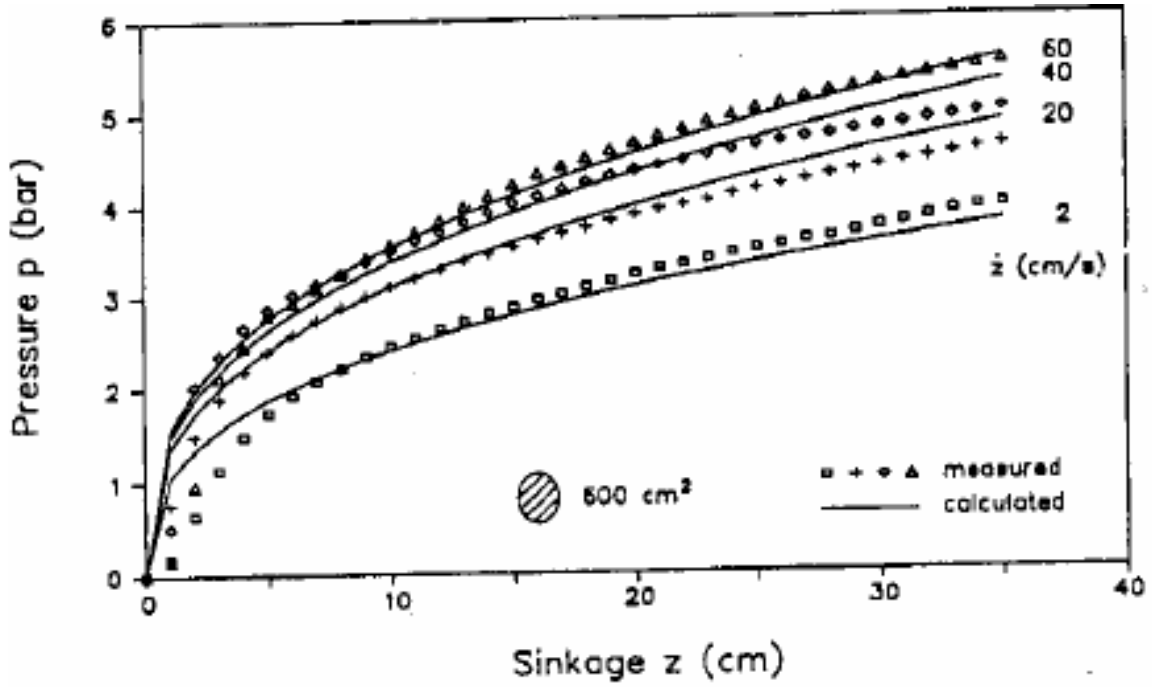


Fig. 2.13. At distinct penetration speeds when subjected to a loading surface plate of area 500 cm², the relation of calculated and evaluated pressure-sinkage curves (Grahn, 1991)

Pope (1969) investigated in the rate of sinkage and in doing so revealed its significance in influencing the pressure-sinkage relationships. It is presumed that the model put forward by Pope matches a power law of the form with regard to pressure-sinkage relationships, as portrayed in Eq. 2.29:

$$p = p_0 \left(\frac{u}{u_0} \right)^m. \quad (2.29)$$

The novel model is demonstrated in Eq. 2.30, drawing from the Reece model.

$$p = (ck_c + \gamma bk_\phi) \left(\frac{z}{b} \right)^n \left(\frac{u}{u_0} \right)^m. \quad (2.30)$$

The sinkage exponents, plate sinkage velocity, and sinkage velocity are represented by n and m , u_0 , and u respectively.

2.5.3. Soil hardpan

The shape of curves 1, 2, and 3 are contingent on the values of exponent n and as illustrated by the curves in Fig. 2.14, the rise in ground pressure occurs at the same time as a fall in monotonic sinkage, which links to the particularly relevant fact that solely homogenous soils absent of hardpan are described by Eqs. 1 to 30. As demonstrated in curves 4 and 5 in Fig. 2.13, soils with a hardpan situated at depth H frequently permit vehicle functionality in practice. Possessing a rise in ground pressure until the asymptotic value Bi , which represents soil bearing capacity, concurrently with a monotonic reduction in sinkage characterises the behaviour of soils with $H=\infty$ seen in curve 4. At a finite depth $H=\text{variable}$, soils with the hardpan at such a depth have their behaviour expressed by curve 5. The hardpan here functions to restrict the sinkage which occurs non-monotonically. The pressure-sinkage relationship of a larger contact area cannot be predicted by attaining the pressure-sinkage relationship from a smaller plate, in a non-uniform

2. Literature review

terrain, as a greater depth must be reached by the plate with a larger dimension that could possess distinct mechanical characteristics compared to a shallower layer, despite the equivalent ratio (Wong, 2001). Soil resistance is stronger and a bulb of radial stress is more significant when subjected to a larger contact area, thereby causing a plate with a smaller dimension to be penetrated more than a plate with a larger dimension, in soils with a shallow hardpan (Bekker, 1969; Wong, 2001; Lyasko, 2010).

The stress distribution in the soil body is profoundly altered by a hardpan. Many academics remain unaware of this vital finding. A homogenous half-space is found to have possess 60% less pressure than found in a hardpan, otherwise known as a firm layer. Above the rigid layer, the pressure hardly diminishes. Thus, agricultural soils tilled to a depth between 30 and 40 cm are more effectively embodied by the finite half-space (Sitkei et al., 2019; Hamada et al., 2021; Wang et al., 2021).

The impact of soil hardpan is demonstrated in Eq. 2.31, portraying the analytical pressure-sinkage model developed for such a purpose (Ageikin, 1987a, 1987b):

$$p = \frac{2EB_H z}{2Ez + \pi B_H A_0 B J Q_1}. \quad (2.31)$$

The width, radius, or geometric parameter of the plate touching the soil is represented by B while Young's modulus is indicated by E . In addition, the model parameters are presented by J , Q , B_H and A_0 are calculated via the following expression:

$$B_H = \frac{B_i}{\arctan\left(\frac{\pi(H-z)}{2B}\right)} B_i = \frac{L}{L+0.4B} \frac{\gamma g}{1000} \frac{1-S^4}{2S^5} B + \frac{L+B}{L+0.5B} 2C_0 \frac{1+S^2}{S^3} + \frac{\gamma g}{1000S^2} z, \quad S = \tan\left(\frac{\pi}{4} - \frac{\phi_0}{2}\right), \quad Q_1 = \frac{2}{\pi} \arctan\left(\frac{H-z}{A_0 B}\right), \quad J = \frac{0.03 + \frac{L}{B}}{0.6 + 0.43 \frac{L}{B}}, \quad A_0 = 0.64 \left(1 + \frac{B}{H}\right).$$

The plate length, angle of soil internal shearing resistance, hardpan depth, soil bulk density, and soil cohesion are represented by L , ϕ_0 , H , γ , C_0 respectively. The bearing capacities of soil with a finite hardpan H is indicated by B_H and the bearing capacities of soil with infinite hardpan H are signified by B_i . The hardpan depth represented by H , which is upper soil layer thickness that is comparatively soft and can be deformed beneath a normal load.

Drawbacks of the Ageikin model are highlighted by Lyasko (2010), such as the incompatibility of specific kinds of soil to function within the calculation of soil bearing capacities with infinite hardpan. In addition, mean ground pressure serves as an erroneous determinant within the analytical model of stress distribution regarding soil subjected to a plate. Eq. 2.32 portrays the analytical model proposed by Lyasko to overcome such drawbacks.

$$p = \frac{1}{\frac{D_1}{B_i} + \frac{D_2}{Bz} \omega B \xi}. \quad (2.32)$$

The calculation of the model parameters represented by B_i , ω , D_1 , ξ , and D are carried out via the following expression:

$$D_1 = \frac{2}{\pi} \arctan\left(\frac{\pi(H-z)}{2B}\right), \quad D_2 = \arctan\left(\frac{H-z}{A_0 B}\right), \quad \omega = A_0 J(1.14 \leq \omega \leq 2.15), \quad \xi = 1 + 1.86 \left(\frac{x}{2} + \frac{x^2}{3} - \frac{x^3}{5}\right),$$

$$x = (1 - \exp(-3.74B)), \quad B_i = \left[\exp(6.65 \tan \phi_0 - 1.75) \cdot \left(1 + 0.25 \frac{B}{L}\right) B + \exp(4.76 \tan \phi_0 + 0.15) \left(1 + 1.5 \frac{B}{L}\right) z \right] \frac{\gamma g}{1000} + \exp(2.32 \tan \phi_0 + 1.5) \left(1 + 0.3 \frac{B}{L}\right) C_0.$$

The variables and parameters are equivalent to the Ageikin model aside from the dimensionless contact pressure concentration coefficient being representing by ζ .

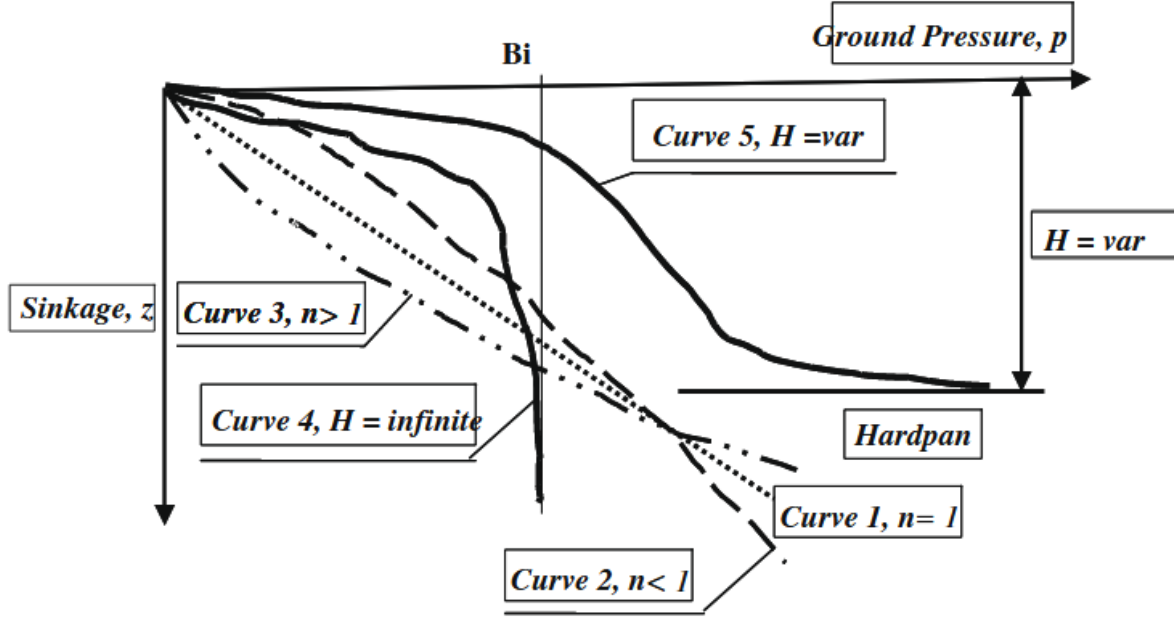


Fig. 2.14. Curves 1, 2, and 3 represent distinct kinds of soil with a standard relationship between sinkage and ground pressure, at distinct n values; curve 4 illustrates sinkage with hardpan $H = \text{infinite}$; and curve 5 represents sinkage with hardpan $H = \text{variable}$ (Lyasko, 2010)

2.6. Soil compaction

Understanding the soil deformation process is required to comprehend the effect of soil compaction on soil functions. As a result of applied hydraulic or mechanic stress, soil deformation occurs. The soil deformation and soil strength are outcomes of the propagation of stress in soil while soil stress and soil strength are outcomes of soil deformation, thus demonstrating the conjoined processes of deformation and stress (Keller et al., 2013, 2022).

The root penetration into soil diminishes, air and water infiltration are restricted, and soil structure is modified due to the physical soil degradation that soil compaction causes (Nawaz et al., 2013). The soil compaction is significantly impacted by soil properties (soil texture, soil water content, soil bulk density, soil strength), number of passes, vehicle load, soil stress, and inflation pressure (Gürsoy, 2021)

Stresses greater than the soil bearing capacity exerted by machinery traffic leads to soil compaction in cropping systems (Hamza and Anderson, 2005; Castioni et al., 2021). Subsoil compaction occurs beneath the soil tillage layers depth while surface soil compaction occurs at a 0.3 m depth, thus at the topsoil layer (Alakukku et al., 2003). Subsoil compaction takes place in cropping systems, yet the majority of compaction takes place in the topsoil layer.

Contact properties between soil compound particles and primary particles determine soil strength which, in turn, signifies that soil structure is impacted by soil mechanical properties. Similarly, soil water potential significantly impacts soil mechanical properties where a reduction in the former leads to increasing resistance in the soil. The findings are inconsistent regarding the extent to which soil compressive properties are impacted by soil texture (Keller et al., 2011).

Agricultural processing methods are influenced significantly by the compaction of agricultural bulk materials. Soil rheological properties regulate deformation and loading rates which, in turn, severely impact structural recovery and the degree of soil compaction prior to such recovery (Keller et al., 2013).

The traditional plastic-elastic concept of the stress-strain threshold where any additional stress surpassing the specific limit of stress causes plastic deformation and below such limit, the soil material responds elastically, serves to sufficiently explicate the occurrence of soil compaction. The matric potential, extent of aggregation, and soil texture are determinants of the stress limit for a particular kind of soil subjected to certain climatic conditions (Nawaz et al., 2013). Therefore, The impact of large residual deformation, relaxation and creep developments, and loading speed on stress are the principal occurrences representative of the compaction process (Sitkei, 1997).

During the period where the material remains compressed, where the velocity of compression determines the density obtainable at a particular pressure, in almost all cases, such agricultural materials are viscoelastic. A dashpot and spring element make up the multiple models that serve to account for viscoelastic properties. The relationship between the strain of the compacted material and the pressure is illustrated in Eq. 2.33 below (Sitkei, 1986)

$$p = C\gamma_o^m \left(\frac{\varepsilon}{1-\varepsilon} \right)^m. \quad (2.33)$$

The volumetric weight and the strain ($\varepsilon=z/H$) are represented by γ and ε respectively. The strain is the relation of the sinkge (z) with the thickness of a soil.

Laib (2002) applied compaction equation (Eq. 2.33) for different densities, as a result Eqs. 2.34 (soil density of 1.218 g/cm³) and 2.35 (soil density of 1.5 g/cm³) were obtained

$$p = 3.89 \left(\frac{\varepsilon}{1-\varepsilon} \right)^{1.9}. \quad (2.34)$$

$$p = 11.8 \left(\frac{\varepsilon}{1-\varepsilon} \right)^{1.55}. \quad (2.35)$$

In addition, the compaction process was outlined through the use of a non-linear viscoelastic-plastic rheological model (Sitkei, 1997). A numerical solution is the only possible answer for the model's differential equation. Said answer is restricted to the constant loading velocity, between zero and infinity. The model was validated via the use of soil, silage, sawdust, and other such bulk materials to provide experimental findings.

2.6.1. Bulk density and moisture content

Total porosity and dry bulk density are among the most commonly used parameters to represent the compactness state of a soil layer. Compaction is detected via the basic physical assessment of bulk density. Alterations to penetration resistance, structure, bulk density, matric suction, and other

properties often occur concurrently. Upon an analysis of distinct soil texture, assessing the influence of traffic through soil bulk density is inadequate, despite modifications to volume being quantified by soil bulk density. The alterations to texture that occur from the range of bulk density is the cause. The influence of external loads can more accurately be quantified in the case where compactness is relativised (de Lima et al., 2017) .

Alterations in soil strength, as a function of depth provoked by tillage, are embodied by the use of the cone index, which is a gauge of compaction, as an expression of soil penetration resistance. As per Kogelbauer et al. (2013), the sensor-based cone penetrometer, which serves as a mechanical indicator, is frequently utilised to measure the cone index of soils in the field. Jabro et al. (2015) note that the kind of soil, bulk density, and moisture content are primary factors affecting such quantification of the level and depth of soil compaction.

When soil water potential diminishes, penetration resistance rises due to soil vulnerability to compaction being impacted most significantly by the soil moisture content. More specifically, a reduction in the admissible ground pressure and soil load support capacity occurs due to the decrease in macropore spaces that the increase in soil moisture content causes.

Furthermore, the contact area between tyre and soil, precompression value, deformability of soil, and the stress propagation capability are determinants of the influence the soil water content has upon soil compaction. Soil becomes progressively more incompressible and plastic upon soil compaction diminishing as a result of the optimum soil moisture limit being surpassed. This limit is the particular value of available soil moisture that determines the amount of soil compaction. Shah et al. (2017) state that soil structures experience less deformation and stress transformation as a result of the soil being more arid. Elevated levels of structural deformation and low structural porosity occur due to high moisture content that regulates the width and depth of the compacted area. Medvedev and Cybulko (1995) note that crop production is enabled via diminished admissible ground pressure of agricultural vehicles that, in turn, is provoked by a rise in soil moisture content and a concurrent reduction in bulk density.

Gysi (1999) observes that upon the application of 130 kPa of ground pressure, marginal alterations were witnessed at a depth between 52–57 cm and 32–37 cm in the soil structure, whereas a drastic reduction in microporosity and air permeability and a drastic rise in bulk density occurred at a depth between 12–17 cm upon the application of 160 kPa of ground pressure. The general pressure distribution when subjected to a loading surface is evidently adhered to in this example. The physical-mechanical characteristics of soil are not embodied solely by its moisture content. At diverse levels of moisture content, distinct soil behaviour of myriad soil kinds was observed due to the specific surface area (m^2/g) and the particle size distribution. The incorporation of the matric potential, otherwise known as the water potential, occurred to resolve the mentioned challenge.

2.6.2. Soil organic matter

Soil biological activities are sustained in large part due to organic matter within the soil material. Vulnerability to compaction is diminished by the heightened resistance to deformation and elasticity that organic matter provides. In addition, reductions in bulk density and increased porosity take place as organic matter tends towards aggregation. The soils that have experienced intensive physical degradation processes benefit immensely when organic matter is introduced (Paradelo and Barral, 2013).

A primary feature of conservation tillage systems are residues on the soil surface, which can function to enable the investigation of the theoretical preventative effect of organic matter. The formation of voids in the soil can be averted through the pressure applied by the high axle load being absorbed by such residues. The impact of soil compaction is mitigated by organic matter on the surface of soil (Hamza and Anderson, 2005).

When the traffic of heavy machinery has passed, the structure and form of surface crop residues can be maintained despite the majority of such a layer potentially being compressed by said vehicles. The return to original form after being compressed likens organic matter to sponges. Nonetheless, soil stirring actions of tyres or tyres slipping can lead to the breakdown of organic matter from the excessive compressive action applied. Soil averts compaction by the pressures of heavy machinery due to the binding of macro and micro soil aggregates to organic residue that is linked to soil particles such as clay and this occurs more frequently at greater depths in the soil profile. The extent of soil compaction is substantially impacted by organic matter in the soil, thereby highlighting the significance of organic matter. The increased compaction in the presence of organic matter would be attributed to compaction vulnerability in the soil (Shah et al., 2017).

2.6.3. Tillage operation

Tillage has been deemed one of the most significant agronomic approaches that can modify properties of soil and create a complicated soil ecosystem (Jabro et al., 2015; Kim et al., 2020). Soil manipulation, disturbance, and losing are outcomes of the practice of tillage. The kind of tillage practice, soil moisture, soil texture, and organic matter are determinants of the extent to which soil overturn and loosening occurs. Moreover, in comparison with untilled soil, more profound chemical movement, greater rooting development and depth, and enhanced aeration and water movement all occur as a result of the soil manipulation and loosening that deep till enacts. The storage in soil, aggregate stability, soil bulk density, water movement, and other physical characteristics of soil are all altered by the enactment of tillage (Jabro et al., 2016).

It remains uncertain, to this day, how much bulk density and soil strength are impacted by tillage. Overall, bulk density and soil strength are diminished by tillage operations. Afzalnia and Zabihi and Peralta et al. (2014; 2021) discovered, on the other hand, that the bulk density and soil penetration resistance in tillage systems displayed no alterations. Blanco-Canqui and Ruis and Jabro et al. (2014, 2016; 2018) observed, in comparison to traditional tillage systems, that diminished or no-tillage operations demonstrated higher levels of bulk density and soil strength. Another academic work found that elevated quantities of organic matter and residue led to diminished soil bulk density when subjected to no tillage (Amuri and Brye, 2008)

Distinct local load carrying capacities at distinct depths are generated by tillage operations and the settling that follows. When subjected to several tillage conditions, the distributions on sandy loam soil, assessed via a cone penetrometer, is demonstrated in Fig. 2.15. A low load carrying capacity was found in the upper loose layer while the deeper layers possessed greater capacity. In addition, the tillage operation determined the load carrying capacity in deeper layers. As seen in line 4 of Fig. 2.15, the surface pressure applied progressively diminishes as a function of depth, in adherence with Boussinesq's theory. The relative depth, represented by the dotted lines, is linked to the pressure distribution which alters when at a particular depth within a rigid layer. The force divided by the cone cross-section signifies the cone penetrometer resistance, as per the CI (Sitkei et al., 2019).

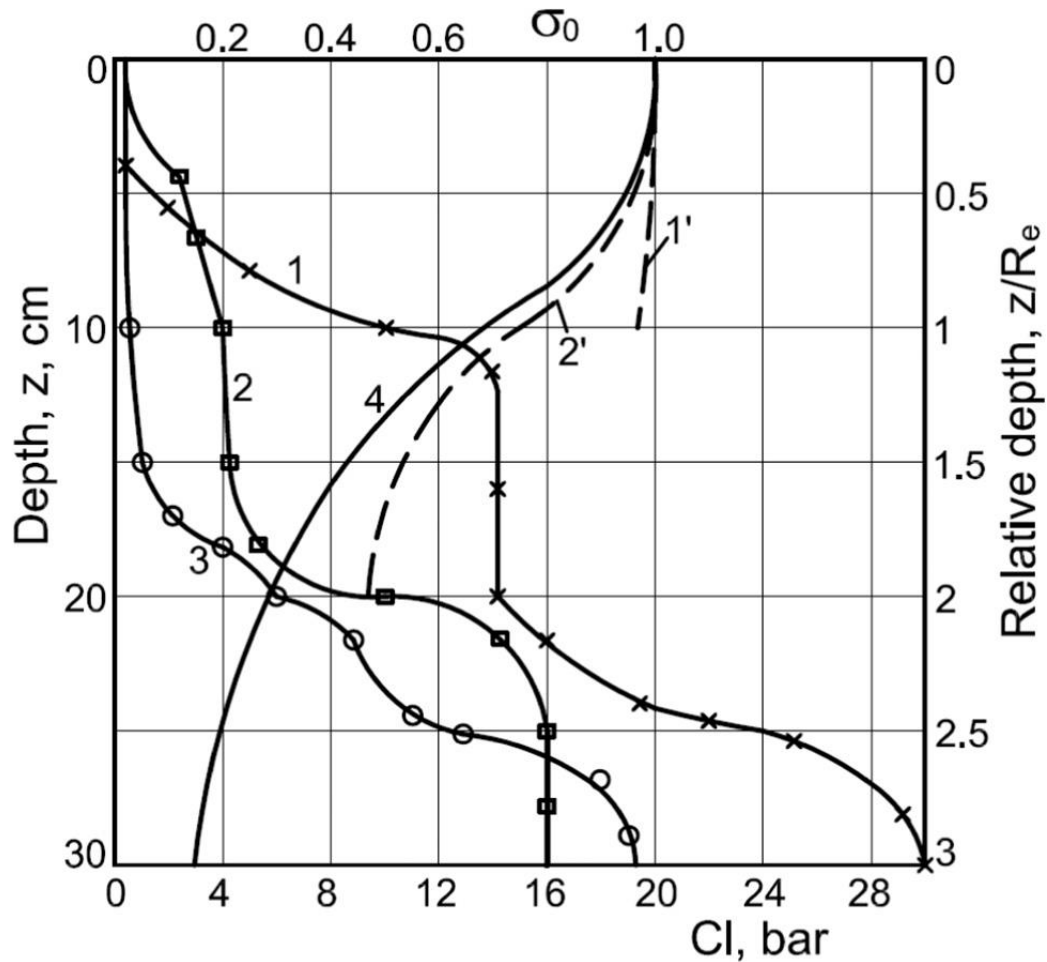


Fig. 2.15. Following several tillage operations, hardness distribution in soil: 1 – stubble field; 2 –disc harrowed; 3 – chisel tilled; 4 – homogenous half-space pressure distribution; 1' and 2' forecasted stubble field pressure distribution and following disc harrowing (Sitkei et al., 2019)

2.6.4. Mapping of momentary soil properties

The action of tillage equipment and the traffic distribution and intensity of agricultural machines determines the extent of compaction in a field, producing spatially variable results. Alaoui and Diserens (2018) observe that a long memory effect is signified by the duration of subsoil compaction of agriculturally utilised fields surpassing decades, despite climate variables and season land management operations causing short-term alterations in topsoil properties. Beckett et al. (2018) state that a dynamic penetrometer forced into the ground by recurrent hammering can measure soil penetration resistance at the field scale. Similarly, Vaz et al. (2011) note that a static cone penetrometer forced into the ground at a constant velocity can measure this as well

Through the use of regression equations, plasticity, matric potential (ψ), porosity (ϕ), soil texture, water content (θ), bulk density (ρ_b), and other soil parameters were correlated with penetration resistance (PR) in several field and laboratory-based investigations. Organic matter, particle density and shape, particle size distribution, and soil mineralogy are among the soil properties approximate constant over time that demonstrate intensive spatial heterogeneity as they alter with PR . Conversely, total porosity, matric potential, water content, bulk density, and other highly spatially and temporally dynamic soil properties alters with PR . Vaz et al. (2011) determine that an inverse correlation to soil water content and a direct relationship to bulk density is demonstrated by PR , as per experiments involving several kinds of soil.

A fraction of a threshold value served to express the calculation of the relative porosity and relative bulk density via evaluations of the clay content, bulk density, organic matter content, and relative porosity (Brus and van den Akker, 2018). Through a multiple regression analysis, plot-assessed values for a cartographic depth-to-water index (DTW), soil depth, density, organic matter content, slope, texture, elevation, and soil moisture were aggregated with *PR* measurements to provision delineated maps of *PR* (Campbell et al., 2013). Specific soil map data served as a basis to compare the load bearing capacity to the soil stress provoked by agricultural machinery, as per differential GPS data (Duttmann et al., 2014). A higher soil stability seemed to balance the overestimation of vertical stress upon assessing the elevated values of soil hardness.

The impacts on soil hydraulic characteristics by the spatial element of soil compression throughout a year remain deficient, despite novel outlooks in the evaluation of spatial distribution of soil compaction. Furthermore, assessing the risk for compaction when there is traffic in the field lacks a widely accepted method to accurately evaluate mechanic properties.

2.7. Deformation under loading surface

The wheeled vehicle mobility is principally dependent upon soil deformation in off-road terrain (Jang et al., 2016). The expulsion of air, otherwise known as compaction, is outlined by the collective term, deformation (Earl, 1997). The dry soil bulk density seemingly increases due to the decrease in soil permeability and porosity alongside the physical degradation of soil leading to compaction, within the process of soil compaction (Moinfar et al., 2021).

As illustrated in Fig. 2.16, very heavy loads provoke an intriguing form of soil deformation. The shear stress concentration in the plough pan can lead to the platy structure rupturing and the subsequent destruction of a priorly formed rigid plough pan layer on top of a weaker subsoil when a first-time wheeling event occurs with a sugar beet harvester (35 Mg). The subsoil compaction can be exacerbated as a result of the deeper stress penetration induced by recurrent wheeling at such a location (Horn and Peth, 2011).

Earl (1997) states that motion of the soil beneath the plate as well as lateral and vertical compaction make up the deformation that takes place in a plate sinkage test. Pillinger (2016) employed the cone penetrometer in a field to determine the soil density distribution in deeper layers of sandy loam soil. As demonstrated in Fig. 2.17 (a) and (b), Pillinger draws attention to two deformation zones, the stationary zone with constant resistance, and the build-up zone with rising resistance, comprise the two deformation zones usually found in the field.

The pressure rises to critical depth within the build-up zone, where values of 2 to 12 cm depth were deduced for the critical depth. Soil density and moisture content determined such values. Subsequently, within the stationary zone, the pressure maintains a constant level. The plate sinkage test enables the observation of this occurrence. The expanding deformation zone is linked to the sinkage as dry bulk density rises as a consequence of the expulsion of air, following the rearrangement of soil particles and aggregates in the build-up zone once loading begins. The deformation zone stays constant when the soil under the plate undergoes no additional compaction at the critical relative depth, upon the plate sinking when the load is heightened further. Resultantly, as Earl (1997) notes, lateral displacement of compaction and soil largely induce sinkage, demonstrated by the lateral compaction and deformation provoked by the formation of a conical mass that move with the plate.

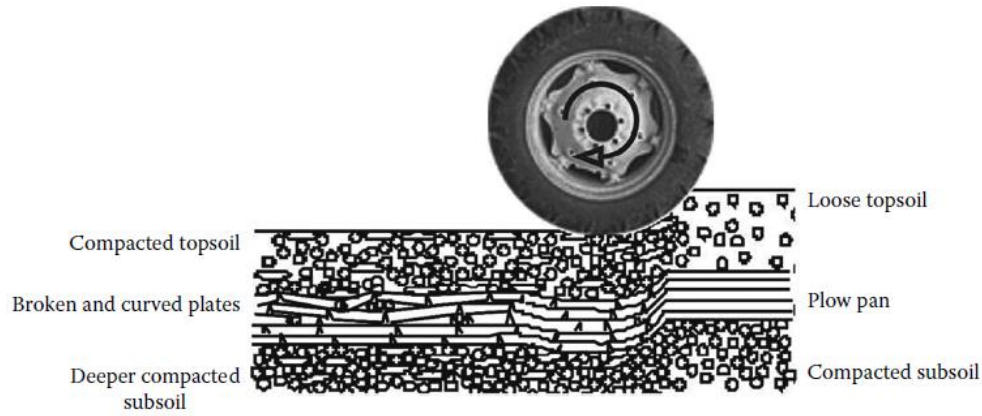


Fig. 2.16. Schematic sketch of the original wheeling with a heavy sugar beet harvester and the outcome of stress-induced alterations in the plough pan layer (Horn and Peth, 2011)

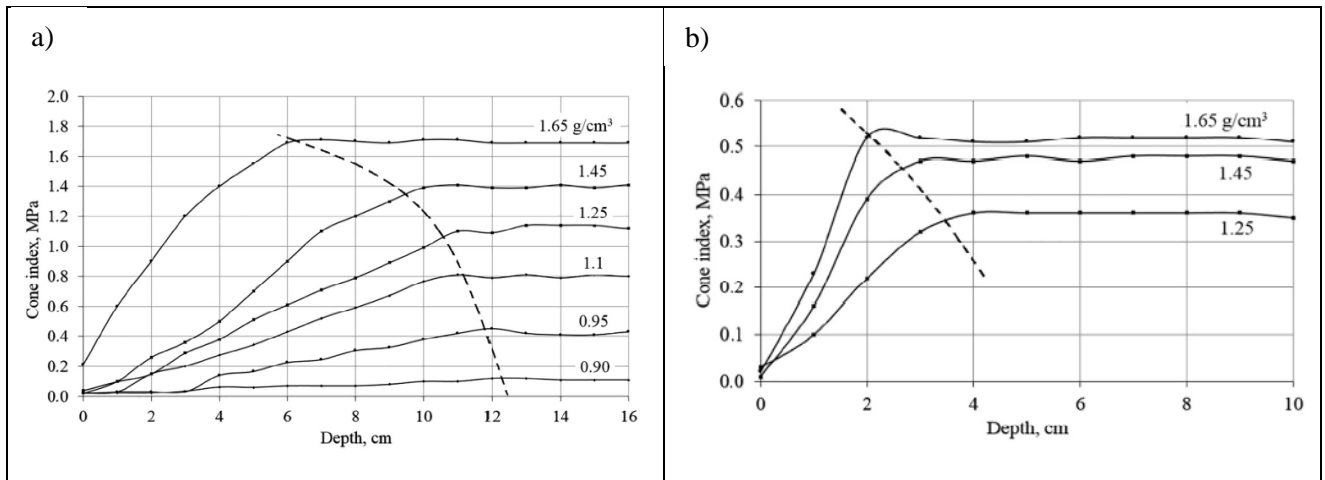


Fig. 2.17. Penetrometer measurements of cone (2 cm^2 and 60°) for various soil densities a) Moisture content M.C. = 9% and b) Moisture content M.C= 15% (Pillinger, 2016)

2.8. Dimensional analysis

Only when independent variables are used to represent the elements that impact physical processes, can such processes, regulated by natural laws, be comprehended. For a given process, deducing every single parameter involved in the process to thereby enable analysis is not only the most vital aspect but is also frequently the most challenging. The conversion into a dimensionless form of a differential equation is an ideal beginning in attaining the necessary parameters. Acquiring the principal governing variables via a physical analysis of the procedure is beneficial if there is a lack of understanding in the governing of equations, which is highly useful. Langhaar and Sitkei et al. (1951; 2019) observe that dimensional analysis leads to the similarity of number being determined.

Oyama (2011) notes that the behaviour of a system is described by the sets of variables that provision order-of-magnitude estimates, forming dimensionless numbers used in multiple fields of engineering. The total physical dimension is equal to unity, in the powers of physical quantities represented by the denominator and numerator alike, within the fractions, otherwise called algebraic expressions. Multiple aspects benefit from the use of dimensionless numbers, for example, the quantity of variables necessary for the outlining of an issue is diminished. In addition, favouring large terms over small terms and converting governing equations into a dimensionless

form simplifies such equations. Ruzicka (2008) states that significant physical quantities with regard to valuable scale estimates are also generated by dimensionless numbers.

Hegedus (1965) was one of the first to process and outline plate-sinkage parameters via dimensionless numbers in the field of terramechanics.

The nonlinear segment of the sinkage exponent is mirrored by the dimensionless function (λ_N) in an academic work (Ding et al., 2014). The curve of the pressure-sinkage relationship can also be modulated by said function. Length, width, radius, and other plate parameters are represented by the parameter (λ_N) as a function of several elements. Ding et al. (2014) observe that velocity, sinkage, and load are examples of motion state parameters.

Within a dimensionless form, the contact surface of tyres F could be estimated, as per Sitkei (2015). In said study, the mean pressure was attained via the incorporation of the equivalent diameter of the contact surface with the dimensionless form. As demonstrated in Eq. 2.36 below, the implicit equation for z/D was formed by the analytical relation between the widely acknowledged dimensionless quantities which, in turn, were enabled by the application of an equilibrium between the mean soil pressure and the mean tyre pressure:

$$\frac{z}{D} = \sqrt{\frac{4b}{\pi D}} \left[0.18 + 0.75 \left(\frac{z}{D} \right)^{0.8} \right]^{\frac{n-2}{2n}} \left(\frac{G}{bkD} \right)^{\frac{1}{n}}. \quad (2.36)$$

The load carrying capacity factor, wheel width, vertical soil deformation, wheel diameter, and nominal load are represented by k , b , z , D , and G respectively.

Furthermore, as portrayed in Eq. 2.37, an explicit equation directly correlated to the relative wheel sinkage was established via the determination of an additional correlation for the coefficient of rolling resistance (f) (Sitkei, 2015).

$$f = 0.03 + 0.97 \left(\frac{z}{D} \right)^{0.76}. \quad (2.37)$$

Sufficient precision is enacted by the theoretical approximation of the rolling resistance of tyres. Nonetheless, dependable values for the exponent n and the load carrying capacity factor k are required to meet the necessary conditions n .

2.9. Summary of literature review

In a given terrain, the traction properties and mobility of a vehicle are dependent upon the load bearing capacity, otherwise referred to as the pressure-sinkage relationship, as per the literature review. Multiple loads bearing capacity models have been put forward since the 1950s. Nonetheless, the complete categorisation of the load bearing capacity of distinct soils has yet to be determined. Within the field of terramechanics, the most challenging area is the establishment of the load bearing capacity factor. Such challenges often result from: the hardness distribution in a finite half-space; the impact on mechanical properties by the distribution of moisture content; the very high variability of soil texture; and the interaction of a surface loading area with finite half-spaces of distinct thickness alongside the behaviour of a finite half-space when subjected to a vertical load.

Studies have failed to examine the mentioned challenges, hence, further investigated of such areas is recommended and merited. Furthermore, knowledge regarding validated values for physical-mechanical properties with regard to soil structure and type was lacking. The challenges that soil classification confronts includes: the distribution of depth, in field conditions, and the mapping of momentary soil properties; settling in time, evaporation, dynamic moisture content distribution, precipitation, wind, and other environmental effects; the differences in the properties in time and space of unquantifiable kinds of soil with organic matter and particle size distribution; the absence of a dependable working correlations between mechanical properties and fundamental soil properties; and the impact on mechanical and structural properties by tillage operations.

The research objective of this work, namely, overcoming the aforementioned challenges could be fulfilled by systematically enacting the following measures: adoption of integrated variables and dimensionless numbers to diminish the number of variables; clarifying fundamental soil reaction to surface loading, utilising a diverse scope of finite soil thickness and soil characteristics for homogenous soils followed by non-homogenous soils, performed meticulously in a laboratory; analysing and accounting for the variability of potential real physical conditions as a function of depth. In so doing, each significant physical phenomena that impacts soil behaviour could be comprehensively investigated.

The history of load bearing capacity establishment spans circa a century, as per the examination of the literature. Nevertheless, the complete classification of the load bearing capacity of soils has yet to be determined. Hence, this study has explored the manner in which load bearing capacity as a function of thickness is impacted by loading surface diameter and the behaviour of finite half-spaces in order to address the gaps in the literature. Consequently, this work was able to fulfil its stated aims of providing solutions and data regarding the challenges and gaps present within the literature.

3. MATERIALS AND METHODS

This chapter presents the materials, procedures, and processes used in the research, including the scientific methods involved in the experimental measurements and the description of the test systems to obtain the set research objectives.

3.1. Bevameter parts design

This section presents the design and construct a bevameter instrument that can be used to simulate the finite thickness soil.

3.1.1. Mechanical structure

The overall dimensions of the apparatus are 200 cm in length, 100 cm in width, and 120 cm in height. The experimental device includes fixed as well as movable parts. The fixed part (shown in Fig. 3.1a) is the frame that contains the soil bin and is formed of two longitudinal rails, steel bars supporting the base of the bin, four corners of angle steel with a groove that can carry the wood pieces forming at the sides of the soil bin, four fixed horizontal steel bars that can support the sides, and three fixed vertical steel bars for the length sides that can support the sides while pushing the soil. Mild steel hollow rectangle sections are used to construct sides and the supporting base while angle steel with some adjustments to make it more suited to carry the sides are used to construct the corners. The moveable parts (illustrated in Fig. 3.1b) form a frame established of three parts, two vertical and one horizontal (it has rail from two sides). Pairs of threaded rods M10 of 97 cm length were assembled with the vertical part of the mobile frame to provide stability for the vertical movement. The mobile frame moves longitudinally inside the fixed longitudinal rail, and this movement is guided with rollers that prevent any rotation or lateral movement. The other movable parts are steel bars linked to the corner of the fixed frame using a hexagon head bolt to add more height to the soil bin and support the wood pieces. The hydraulic cylinder, force, and displacement sensors are carried using a holder on the mobile frame's longitudinal part. This holder can move transversely on the rails and is directed by a roller. As the mobile frame moves in two directions, any point on the entire soil surface can be tested. Supplementary parts are also used to support the tubes that carry the hydraulic fluid to the hydraulic cylinder.

Soil bin was developed with a steel sheet base of 20 mm thickness and rectangular wood plates with a 10 cm thickness placed inside the corners of the fixed part to set up the sides. Of these, three sides are changeable, and one is fixed. Numerous wood plates were used to alter the bin's height and examine different soil thicknesses.

The instrument box contains the hydraulic parts and the electric switch and was with 86 cm height, 41 cm width, and 65 cm length. The box was placed behind the fixed side of the soil bin.

3. Materials and methods

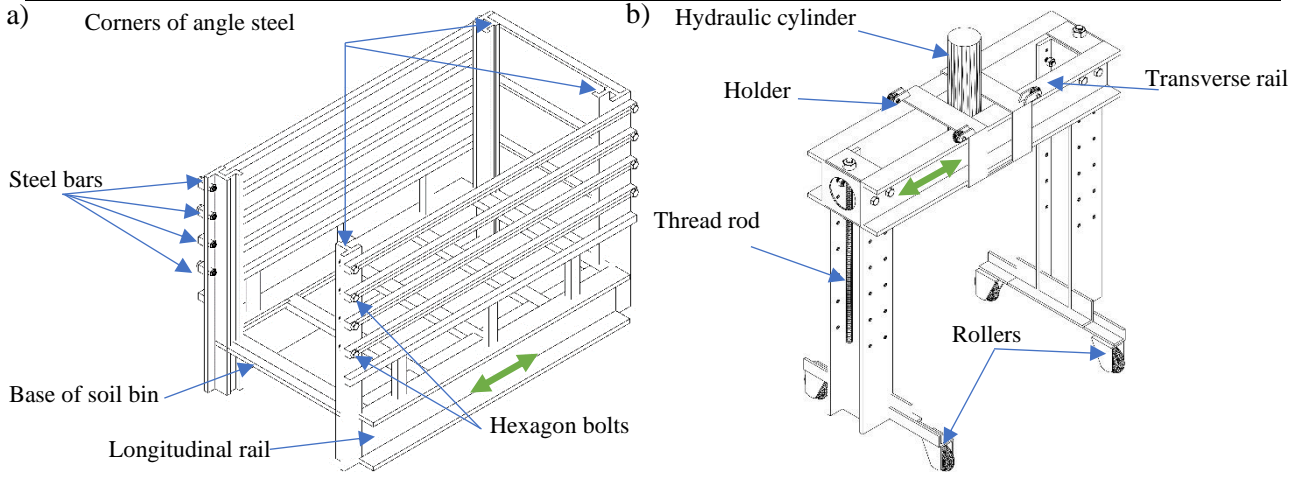


Fig. 3.1. The mechanical structure of the bevameter device: a) fixed part and b) mobile part

Further, the sinkage plates were formed of a circular shape steel and three different diameters (10 cm, 15 cm, and 20 cm) and 10 mm thickness. The sinkage plates were joined using a thread into the load cell that was connected with the displacement sensors to the end of the hydraulic cylinder. These parts are all displayed in Fig. 3.2 from the front, side, and top views as well as the isometric view. Fig. 3.2 depicts the device including all parts after manufacturing and assembling. Fig. 3.3 shows the bevameter instrument.

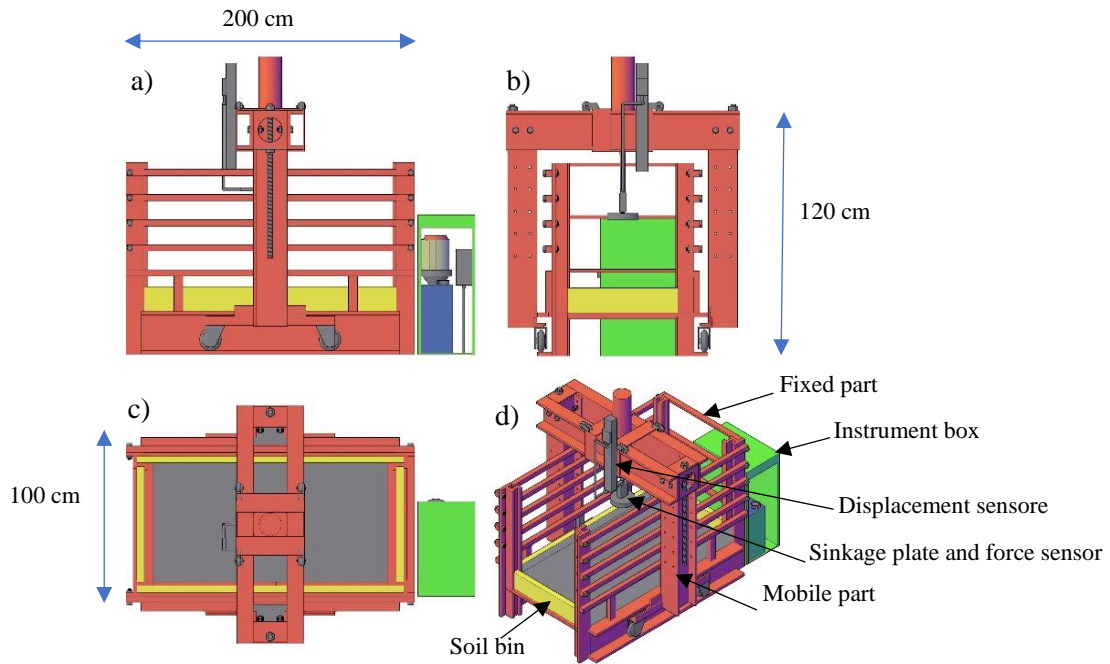


Fig. 3.2. The assembled parts of bevameter device including the mechanical structure, the soil bin and instrument box: a) Front view, b) Side view, c) Top view and d) Isometric view



Fig. 3.3. Bevameter instrument

3.1.2. Control system

Fig. 3.4 shows a schematic diagram of the bevameter's control system and includes a hydraulic system, measurement sensors, and data collection unit.

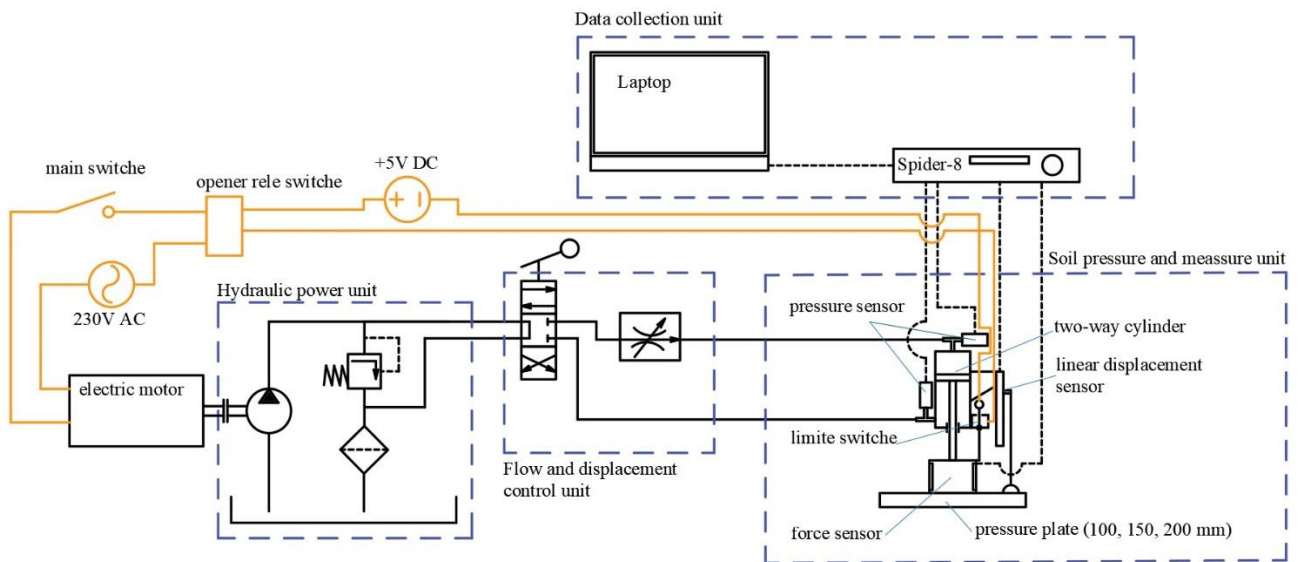


Fig. 3.4. The control system of the bevameter device

Hydraulic system

The hydraulic unit was used to apply force on the sinkage plates and was formed of the following parts with appropriate fittings:

1. A hydraulic cylinder that was made of stainless steel to apply vertical force on the sinkage plates. It was designed and manufactured in Fatér Hidraulika Kft, Hungary. It is a front-flange mounted hydraulic cylinder with specifications such as double-acting hydraulic

- cylinder, maximum pressure of 80 bar, a max stroke of 300 mm, piston diameter of 75 mm, and piston velocity speed between 20 and 30 cm/min.
2. A pressure flow control valve (2FRM5-32/3 Q, Ponar wadowice, Poland) that is a two-way flow control valve that establishes the fluid flow constant in one direction and allows free flow in the opposite direction. That is, it controls the piston's speed by regulating the flow rate of the hydraulic fluid that enters the hydraulic cylinder. This valve can also adjust the sinkage plates' penetration rate up to 3 cm/s.
 3. A directional control valve (P40, Hydro-pack, Europe) that directs the fluid flow to the required line. It is manually controlled with four-ports. Three-positions type of the directional control valve was used.
 4. A filter (HF502-20.122-AS-FG02, Ikron, Italy) that was used to protect the system components from the fluid's contaminant particles.
 5. A pump (C1.25x1T1B, Industrialtechnic SC, Bulgaria) was used to deliver the hydraulic liquid to the hydraulic system. Hydraulic pipes were also employed for transmitting the hydraulic fluid to the hydraulic cylinder so that the sinkage plate could apply force on the soil surface. A pressure gauge with a 25 MPa capacity was used to monitor the pressure level. All the hydraulic parts mentioned above (except the hydraulic cylinder) as well as the electric motor and the main switch were assembled in the instrument box.

Measuring unit

The measuring unit, as shown in Fig. 3.4, consists of an S-beam load cell (HBM, Germany) made of stainless steel with 30 kN capacity to measure the applied vertical load. Analogue displacement encoder (MLO-POT-0360 -TLF, FESTO, Germany) with a 300 mm stroke was also included to measure the vertical displacement (sinkage). The slider of the displacement sensor was connected to the end of the hydraulic cylinder rod and was simultaneously moving.

Data collecting unit

The data collecting system, as shown in Fig. 3.4, includes strain gauges (Spider 8) that work with the software Catman version 5.1. The inputs to the spider 8 include the electric power and the signals from force and displacement sensors, whereas the output was connected to a laptop where the input signal of the applied force and displacement is analysed using the Catman software. Consequently, the pressure and sinkage can be calculated from these data.

3.2. Soil preparation

Soil about 1000 kg was collected from one of the fields that belong to Szent Istvan Campus, MATE University, Hungary, and transferred to the laboratory as shown in Fig. 3.5a. To prepare the soil, the soil was sieved utilizing a 5 mm mesh to eliminate the coarse parts and plant roots as shown in Fig. 3.5b. The purified soil shown in Fig. 3.5c. Next step was storing the soil in place where the soil does not dry as shown in Fig. 3.5d.

3. Materials and methods



Fig. 3.5. Soil preparation: a) Soil brought from the field, b) Sieving the soil, c) Purified soil and d) Stored the soil

The same soil from the same field was used by previous researchers (Máthé, 2014; Pillinger, 2016), the soil was classified as a sandy loam with a composition analysis of clay (<0.002 mm), sand (2–0.05 mm) and silt (0.05–0.002 mm).

3.3. Experimental procedure

The tests were conducted on bevameter under controlled condition inside laboratory as shown in Fig. 3.6a. The first step, running the bevameter from the main switch. Then, moving the sinkage plate to be near to the soil surface by the directional control valve. After that, regulating the penetration speed through the pressure flow control valve via controlling the fluid flow. The directional control valve as well as the pressure flow control valve are shown in Fig. 3.6b.

Different soil thicknesses and bulk densities used in the tests. With each thickness and bulk density, the soil bin was filled with soil up to specific thickness in layers, each layer of 5 cm. For getting different bulk densities, different way to compress the soil was employed. For example, with soil

density 1.2 g/cm^3 the soil bin filled up with the soil without any compressing, while for soil density 1.3 g/cm^3 the soil compressed by using light metal plate. Moreover, with soil density 1.4 g/cm^3 , the soil compressed with using wood plate. With higher bulk density like 1.5 g/cm^3 or more, the soil compressed by using wood plate with additional weight on the plate. Fig. 3.6c shows compressing each layer by using wood plate. The soil surface was levelled precisely to limit the stress concentration on conglomerated points at the soil surface below the loading plate, as shown in Fig. 3.6d. Three different circular sinkage plates of 10, 15 and 20 cm diameter was used for the purpose of applying load. The sinkage plate attached to the force sensor and brought close to the soil surface by running the bevmeter. The S-beam load cell and analogue displacement encoder that are shown in Fig. 3.6e were employed to measure the vertical force and displacement, respectively. The experiments of the current work were performed at a 3 cm/s penetration rate of the sinkage plate. The penetration points were achieved where the soil bin walls could not affect the data. The force and displacement sensors were transferring the signals to Spider 8 (strain gauge measurement device) which is shown in Fig. 3.6f. After that, the Spider sent the measured data to a computer where the Catman software was utilized for evaluating and forming the force-time and displacement-time graphs. The displacement and force data received from the computer were used to represent the relation of pressure-sinkage curves.



Fig. 3.6. Soil preparation: a) Performing bavameter equipment, b) Directional and pressure flow control valves, c) Compressing soil with wood plate, d) Levelling soil surface, e) S-beam load cell and analogue displacement sensors and f) Spider 8 (strain gauge measurement device)

3.4. Determining moisture content and bulk density of the soil

The moisture content and the bulk density determined by the sampling method (core sampler apparent in Fig. 3.7a and b) where several soil samples were taken during and after the tests. The samples were weighed by using scale (Waage Bizerba GE 3001-23, 400/3000 g with accuracy 0,01/0,1g) as shown in Fig. 3.7c and d before and after drying to define the bulk density and moisture content. These samples were dried in the oven at 110 °C for 24 hours as shown in Fig. 3.7e and f.

3. Materials and methods

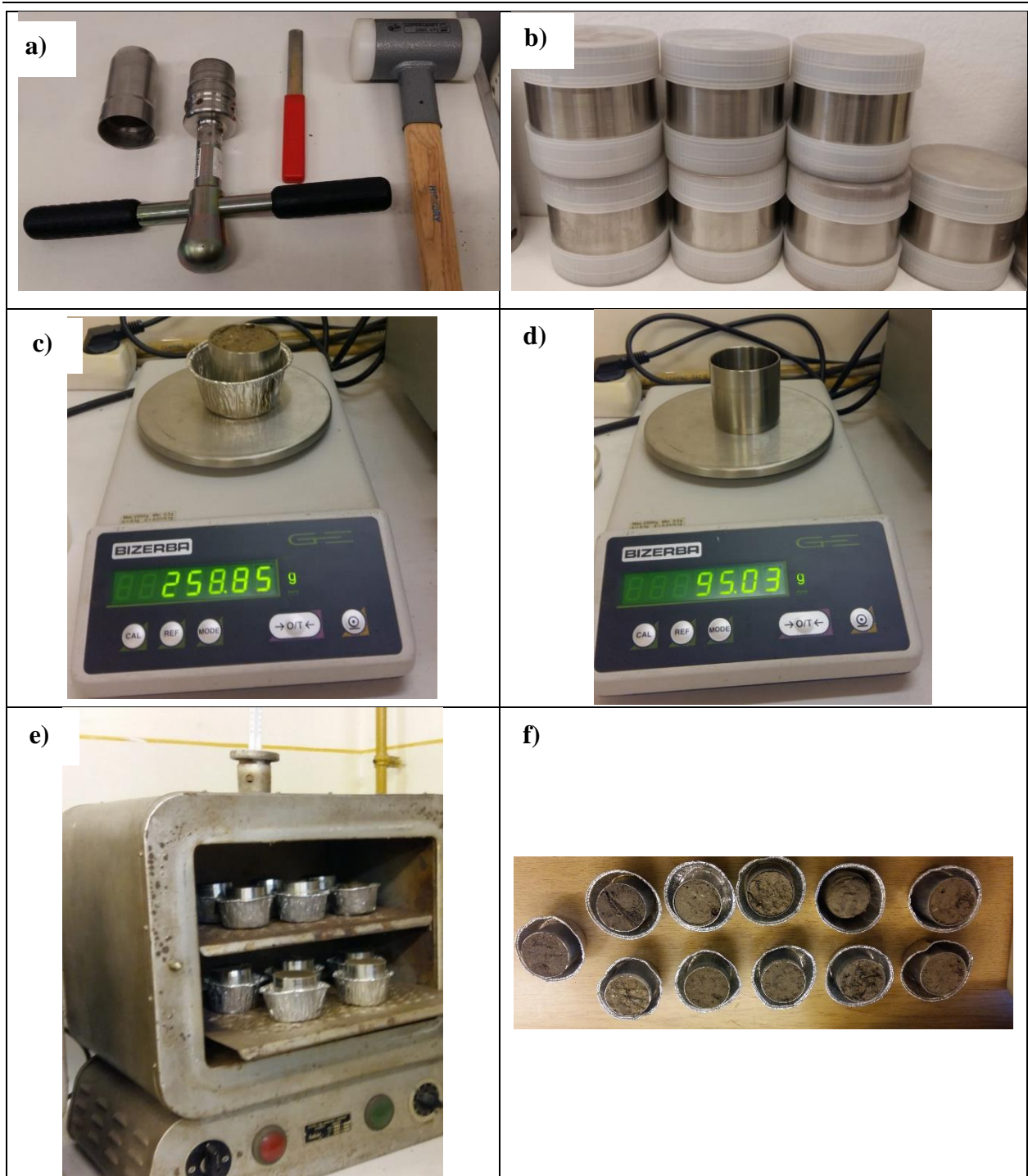


Fig. 3.7. Soil sample: a) Soil core sampler, b) Standard stainless-steel cylinders, c) Weighting with cylinder, d) Weighting empty cylinder, e) The samples inside the oven, and f) The samples after drying

3.5. Confined compression test

The confined compression test was performed in small soil bin shown in Fig. 3.8a. the load applied on the soil surface by performing the big sinkage plate of bevameter as shown in Fig. 3.8b. This circular small bin was designed and constructed with a diameter, height, and wall thickness of 120 mm, 200 mm, and 3 mm, respectively. The material that was used for the construction is steel. A rectangular steel plate (with dimensions of 0.5 m by 0.5 m) was welded beneath the base of the bin on firm ground.

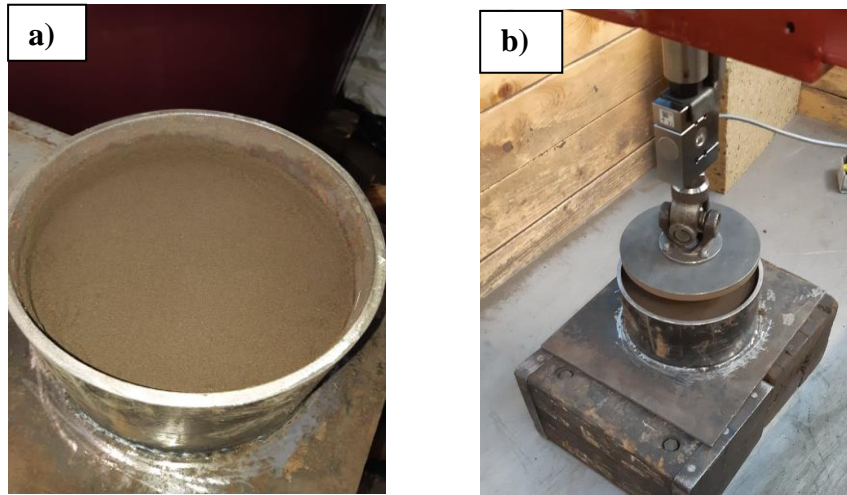


Fig. 3.8. Small soil bin: a) Filled with soil and b) During the test

3.6. Direct shear test

The direct shear box is the simplest well-known laboratory apparatus used to measure soil shear strength properties. In this study direct shear apparatus (ELE Direct/Residual Shear Test Set 110vAC) which is displayed in Fig. 3.9a, b and c used to measure the shear strength characteristic.

Each sample was placed within two square rings. During each test, a normal pressure was applied to the upper part of the soil where the samples vertically confined by pressure pad placed on top of soil box, while the bottom part was moved horizontally. The relative displacement versus shear force was plotted and the soil shear strength properties were estimated based on the Mohr–Coulomb criterion. The horizontal shear was applied with a constant shear rate of 0.6 mm/min (1% per min) for 1000 s (final horizontal displacement is 10 mm). The horizontal load and horizontal displacements were obtained automatically every 10 s using a load cell (force sensor) and displacement sensor.

Five tests were carried out at mass load of 10, 20, 30, 40 and 50 kg in order to estimate the mechanical properties for a given initial dry bulk density. Three measurements were done for each mass load. The measurements were done at moisture content 8%.

3. Materials and methods

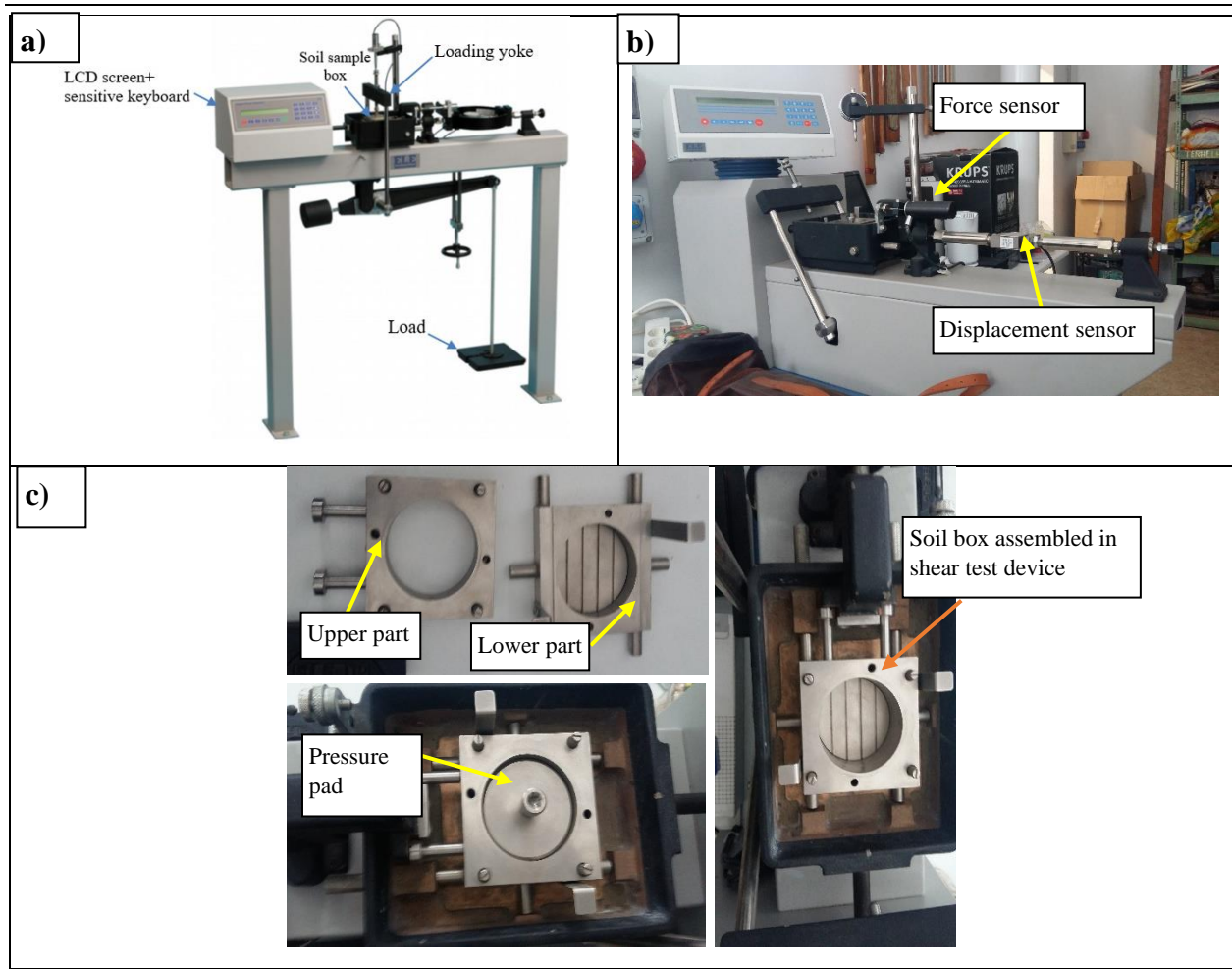


Fig. 3.9. a) Direct shear test apparatus, b) Force and displacement sensors and c) Soil sample box

4. RESULTS AND DISCUSSION

This chapter presents the results obtained from the experimentations and the discussions highlighting the new scientific findings. These include analysing the load bearing capacity of finite half-space by defining the interaction of the compact zone with the effect of a rigid layer. In addition, generalizing the pressure-sinkage relationship by considering the effect of the soil thickness. Moreover, modifying the load bearing capacity factor (k), validation of generalized pressure-sinkage relationship, and studying the behaviour of shallow homogeneous upper layer soil are presented. A bigger plate, due to its more equalizing ability, gives always more reliable results and, therefore, the results for 20 cm plate diameter are taken as more definitive.

4.1. Effect of finite half-space on the pressure distribution under tire

The presence of a rigid boundary within the zone of soil developing bearing capacity increases the unit load supported by the soil. It can have a substantial effect on the pressure distribution, as well as the load bearing capacity, of the soil. The hard boundary on the rigid surface mainly alters the soil's pressure distribution because the pressure is 60% greater compared to that in a homogeneous half-space.

The derived model of Yegorov (Yegorov, 1961) for the stress and displacement of finite thickness foundation of homogenous soil was idealized in understanding the effects of the rigid layer and developing the new model of pressure-sinkage relationship.

By employing model of Yegorov (Fig. 2.11) to consider the finite thickness at relative sinkage (z/R) or relative depth (H/R) of 2, pressure bulb under the load can be plotted as shown in Fig. 4.1. The modification of pressure distribution under the plate due to the finite half-space with rigid layer also shown in the Fig. 2.11 where the pressure of finite half-space is 0.47 and infinite half-space is 0.28. As can be seen the rigid layer raised the pressure as well as the stress under the plate.

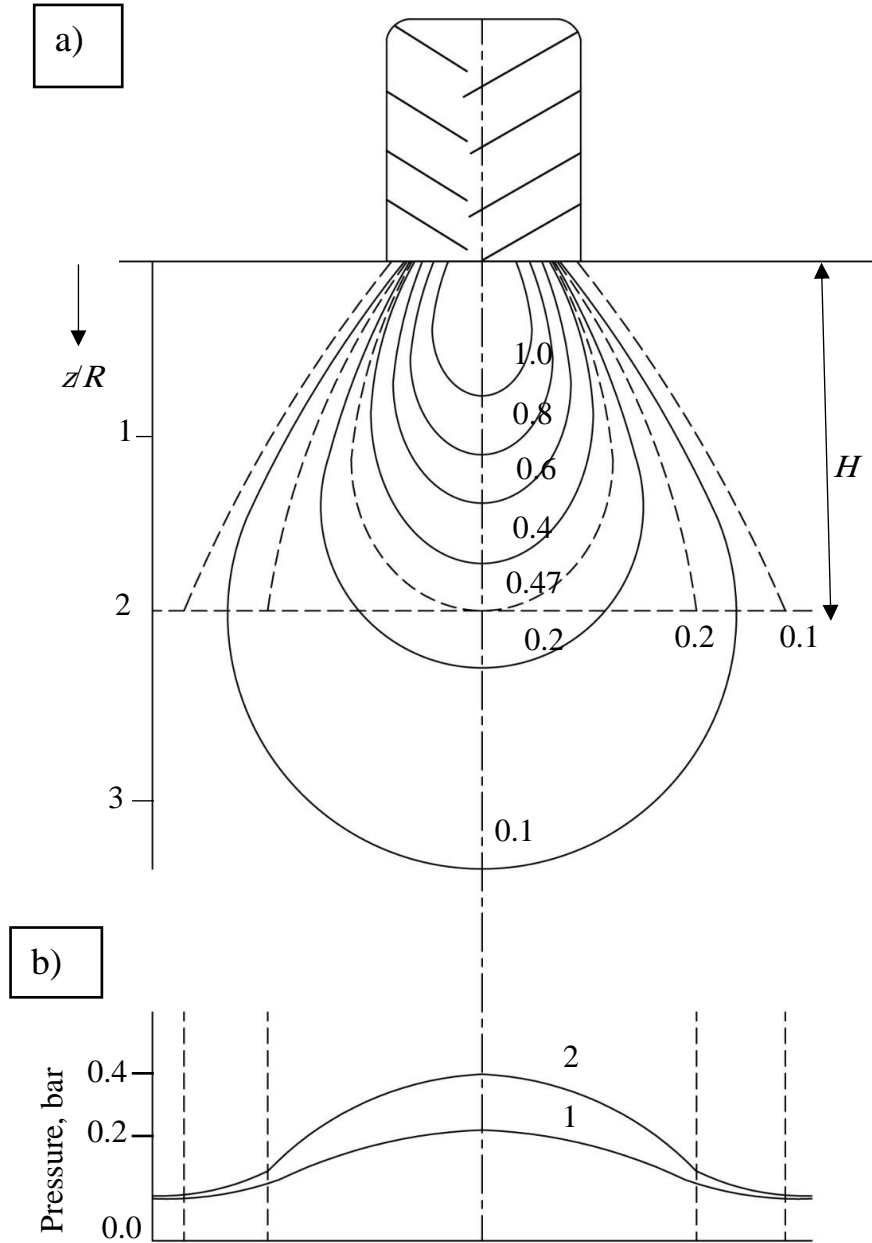


Fig. 4.1. a) Pressure distribution under a tyre concerning infinite and finite half-space and b) Pressure distribution under the load at $z/R=2$, curve 1 represents the pressure with infinite half-space and curve 2 shows the pressure with rigid layer at $H/R=2$

4.2. Deformation under pressure plate as a function of depth/ diameter ratio

Deformation refers to compaction, the deformation in the plate sinkage test involved vertical and lateral compaction, along with soil movement under the plate (Earl, 1997). There are typically two deformation zones in the field Pillinger (Pillinger, 2016) specified the two deformation zones by utilizing cone penetrometer in a field to identify the soil density distribution in the deeper layers of sandy loam soil. The deformation zones are the build-up zone that has an increasing resistance, and the other one is the stationary zone with constant resistance. Their study explained the deformation zones in another study's results (Sitkei et al., 2019). The pressure in the build-up zone can elevate to severe relative depth (z_o/d). In the stationary zone, the pressure remains constant to an extent.

4. Results and discussion

According to Yegorov (Yegorov, 1961), however, if a hard layer is present at a certain depth under the footing (circular or rectangular), it can have a substantial effect on the pressure distribution, as well as the load bearing capacity, of the soil. The hard layer mainly alters the soil's pressure distribution, and the pressure is greater compared to that in a homogeneous infinite half-space. As a result, the interaction of the compact zone with the effect of a rigid layer increases compaction and pressure.

The plat-sinkage test can help observing this phenomenon. Once loading begins in the build-up zone, soil aggregates and particles rearrange while air becomes expelled, which increases the density of the dry bulk. Thus, sinkage mainly results from compaction below the plate. If the plate keeps sinking and the load is increased, then the soil immediately under the plate can no longer compact at the critical relative depth. Because of this, a conical mass is developed that moves by the plate and leads to lateral deformation and compaction; that is, sinkage is largely caused by soil becoming laterally displaced (Earl, 1997).

The soil deformed into three zones under loading surface according to Terzaghi soil bearing capacity theory as shown in Fig. 4.2, which are (I) the wedge-shaped (active zone) zone located beneath the loaded surface, in which the major principal stresses are vertical, two zones (II) of radial shear, and two passive Rankine zones (III). This theory applicable for foundation in infinite half-space. In our case the load is applied from wheel of a vehicle, this loading for short time so the most important zone is the deformation under the loading surface without counting the other zones. Therefore, this study presents the deformation zones of plate sinkage test by considering the active zone under loading surface in addition specified the interaction zone between them which mentioned as transition zone (breaking points) as shown in Fig. 4.3. This section primarily aimed to display the breaking point as critical relative sinkage (z_o/D) by assessing the plate sinkage test's characteristics. The interaction of the compacted soil cone with the bottom rigid layer can be calculated in the following way.

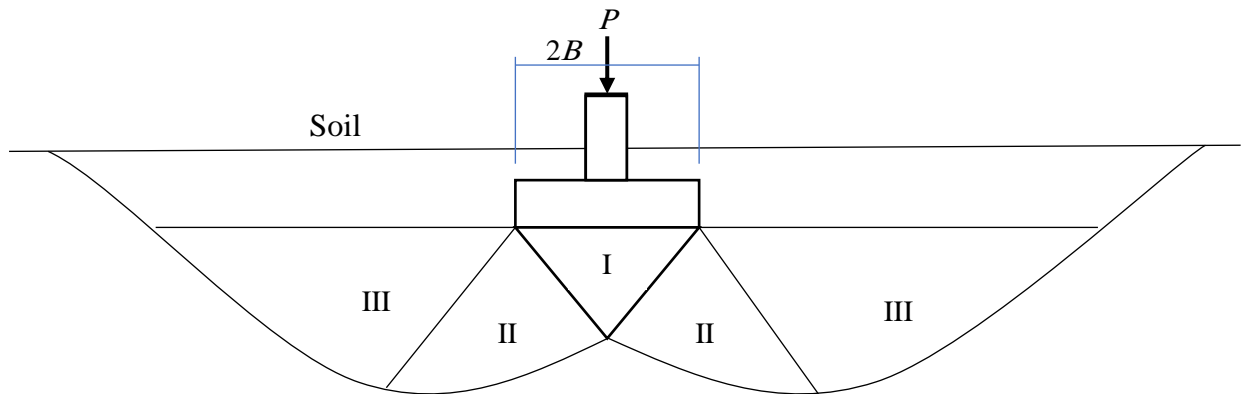


Fig. 4.2. Zones of plastic flow after failure of earth support of continuous footings (Terzaghi, 1943)

The height of the cone is given as (Terzaghi, 1943)

$$\tan\left(45^\circ + \frac{\phi}{2}\right) = \frac{2h}{D} \text{ and } h = \frac{D}{2} \tan\left(45^\circ + \frac{\phi}{2}\right) \cong D. \quad (4.1)$$

For the limit position of the plate (transition), when the compacted cone contacts the rigid, we may write

$$z_o + h = H \text{ or } z_o + D = H. \quad (4.2)$$

Divided by D , yields

$$\frac{z_o}{D} = \frac{H}{D} - 1. \quad (4.3)$$

If the friction angle ϕ is slightly changed then the constant one may also change, mostly in the range of 1 to 1.07.

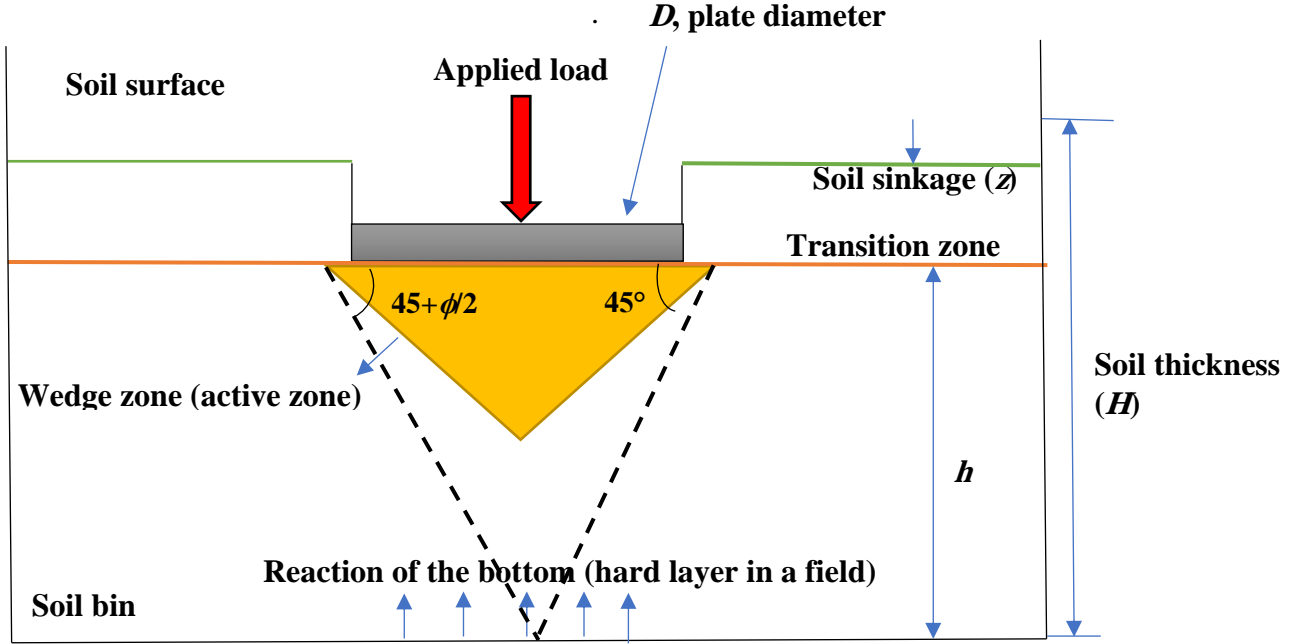


Fig. 4.3. Schematic of the plate sinkage test

4.3. Similarity numbers

A correct similarity number for soils and finite half-space can hardly be derived. The load bearing factor k , for given soil, depends on the soil density (ρ) or specific weight (γ) and plate diameter (D). This dependency concluded from Boussinesq theory for infinite half-space. By considering these quantities k , $\Delta\gamma$ and D , a dimensionless number (Π) can be drawn as shown in the below equation,

$$\Pi = \frac{k}{\Delta\gamma \cdot D}, \quad (4.4)$$

where $\Delta\gamma = \gamma - \gamma_1$, $\gamma_1 = 11000 \text{ N/m}^3$.

The use of $\Delta\gamma$ is supported by the fact that the feasible range of stable soil density is generally over 1000 kg/m^3 , but for sandy soils it is at 1100 kg/m^3 .

In the similarity number we use N and m dimensions. The load bearing capacity factor (k) is calculated with relative sinkage (z/D) ratio (Boussinesq theory). The additional compaction of soil under the plate depends on the strain ($\epsilon = z/H$). Therefore, a change in depth (H) modifies the strain as well as the compaction for the same deformation (z). Consequently, with increasing depth (H), the strain and the compaction decrease. Less additional compaction means lower load bearing capacity factor (k) which is shown clearly in Fig. 4.4.

4. Results and discussion

Fig. 4.4 represent the model of relation between load bearing capacity factor (k) and the soil density (ρ) which is calculated and drawn according to similarity relation. As can be seen in Fig. 4.4 that the soil under density 1.1 g/cm^3 is not stable and has no load bearing capacity factor (k).

An approximate similarity can be characterized by two similarity numbers (Π) and (H/D), the (Π) number represent the infinite thickness and (H/D) represent the finite thickness therefore to combine the effect of the infinite and finite half-space these numbers multiplied with each other as shown in Eq. 4.5. this equation is restricted for plate diameter of 20 cm and relative depth $1 < H/D < 2$

$$\frac{k \cdot H}{\Delta \gamma \cdot D^2} = 1150, \quad (4.5)$$

where $\Delta \gamma = \gamma - \gamma_1$, $\gamma_1 = 11000 \text{ N/m}^3$.

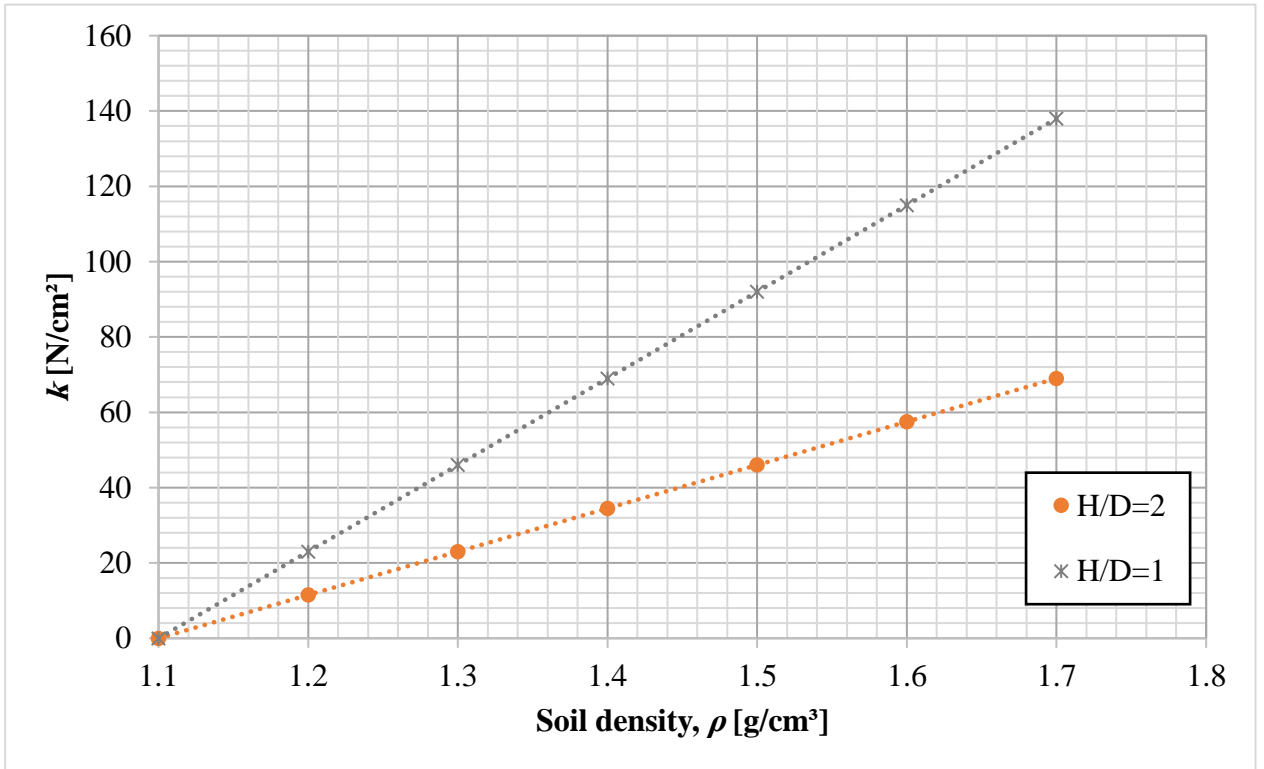


Fig. 4.4. The model relation of k and ρ

The behavior of the finite half-space and the changing hardness of soil within the finite thickness present the greatest difficulties for generalizing the experimental results. In the following, new experimental results in generalized form are presented using similarity equations.

By replacing load bearing capacity factor (k) of Eq. 2.4 with load bearing capacity factor (k) of Eq. 4.5 the following equation can be derived,

$$\frac{p}{\Delta \gamma \cdot D} = 1150 \frac{D}{H} \left(\frac{z}{D} \right)^n. \quad (4.6)$$

Eq. 4.6 represents the generalized pressure-sinkage equation in dimensionless form considering the effect of soil density and the finite depth. The constant 1150 is valid only for the used soil but the form of Eq. 4.6 is generally valid. The H/D ratio is varied between 1 and 2 which is mostly the

4. Results and discussion

case in the practice. In practice, the average loading surface diameter is around 30 cm and for $H/D=2$, the homogenous soil depth should be 60 cm which is hardly the reality. The use of H/D ratio is an approximation for the given limited ratio, and it is not valid for the infinite half-space turns the equation to zero which would mean zero load bearing capacity.

Fig. 4.5 represents the relation between relative sinkage (z/D) and the pressure number ($p/\Delta\gamma \cdot D$) which is calculated and drawn according to Eq. 4.6. This equation is plotted for plate diameter of 20 cm and relative depth $1 < H/D < 2$.

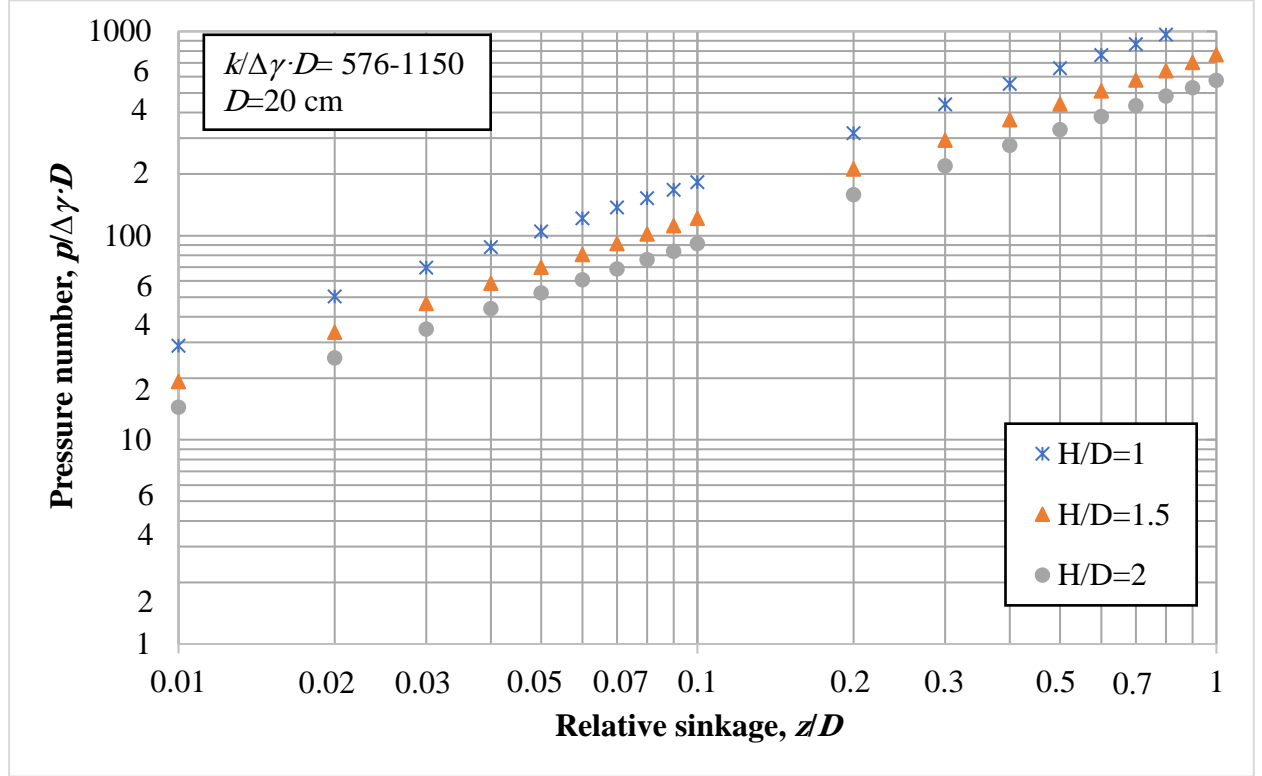


Fig. 4.5. Model of generalized pressure-sinkage relationship for sandy loam soil, no bottom interaction

In order to seek and find general regularities, it is important to use coherent processed values. The typical exponent n for the used sandy loam soil with moisture content in the range of 8-10 % is generally 0.8. we do not examine here the effect of exponent n and, therefore, if a measured plate-sinkage curve shows some deviation from $n=0.8$ then it is purposeful to make a correction based on the equality of measured pressure and relative sinkage in the following form:

$$p = k_x \left(\frac{z}{D} \right)^{n_x} = k \left(\frac{z}{D} \right)^{0.8}, \quad (4.7)$$

from which we get

$$k = k_x \left(\frac{z}{D} \right)^{n_x - 0.8}. \quad (4.8)$$

Obviously, if $n_x=0.8$ then $k_x=k$. for correction we use a measured point near to the breaking point.

4.4. Direct shear test

Using different values of pre-compressing vertical loads, the shear failure line ($\tau = c + \sigma \tan \phi$) of the soil sample has been determined as shown in Fig. 4.6. The figure presents the result of direct shear test with different mass load (10-50 kg). As a result, the value of cohesion of the soil (c) is 54.91 kPa and the value of friction angle is 38° . The values of cohesion and friction angle are comparable with range of results mentioned in literature (Mouazen, 2002; Horn and Fleige, 2003).

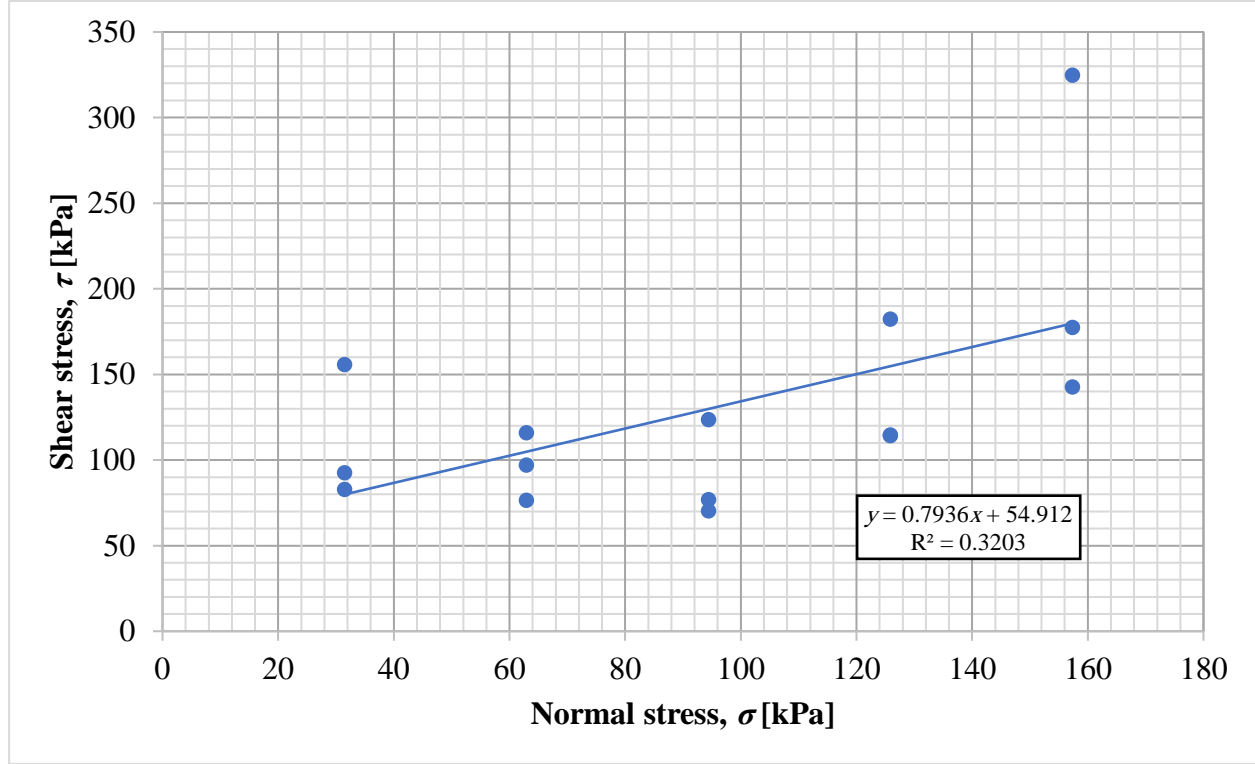


Fig. 4.6. Shear and normal stress for 10 -50 kg mass load

4.5. Interaction of the compact zone with the effect of a rigid layer

As explained in the theoretical chapter there are typically two deformation zones in the field. The first is the build-up zone that has an increasing resistance, and the second is the stationary zone with constant resistance as shown in previous study of Pillinger (Pillinger, 2016), provided that the homogeneous layer is deep enough.

The assessment of Pillinger's measurements shown in Fig. 4.7, where the critical relative depth as the soil density function was plotted. Their z_o/d ratio measured between 2–7 in depth. This value is based on the soil density and moisture content. As can be seen from Fig. 4.7, the critical relative depth (z_o/d) strongly decreases at high moisture content levels, as the soil tends to exhibit plastic flow behaviour. Hence, the experiments conducted in this study considered moisture content levels between 7% and 9%. This section shows the experimental results of plate sinkage test through showing the deformation zones, the interaction of the compact zone with the effect of a rigid layer (transition zone) and critical relative sinkage (z_o/D), called the breaking point.

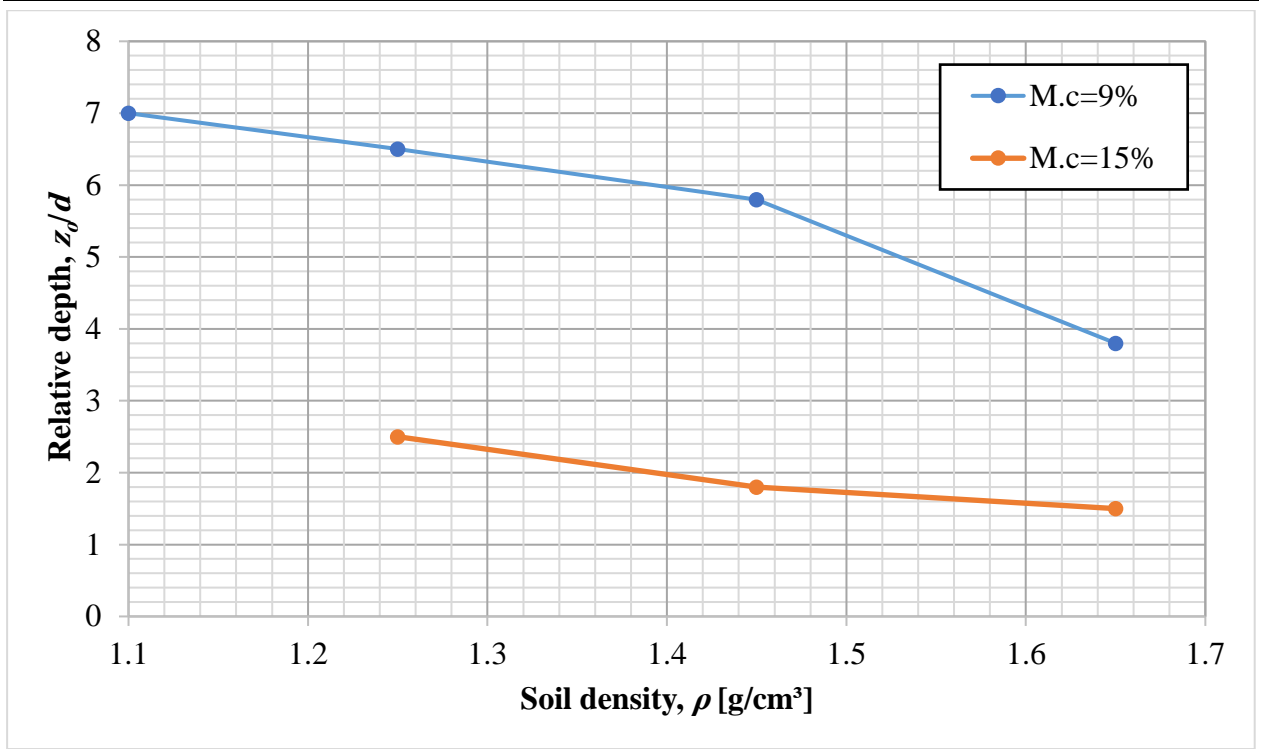


Fig. 4.7. Relative depth (z_0/d) with soil density at a moisture content level of 9% and 15% for a penetrometer cone of 1.6 cm in diameter

The results of applying the derived Eq. 4.1 are shown in Table 4.1 which presents the critical relative sinkage (z_0/D) values of sinkage plates, gathered from the experiments involving varied soil thickness.

Figs. 4.8-4.10 present the results of pressure–sinkage on a logarithmic scale for 18, 30 and 40 cm soil thickness levels, respectively, considering 10, 15 and 20 cm sinkage plate diameters. The measurements were carried out at densities (ρ) and moisture content as shown in Table 4.2. The rest of the results are shown in the appendices A4.

The larger plate's isobars of significant pressure extend deeper; however, the larger plate sense the rigid layer sooner than the smaller plates as can be clearly seen in the figures. The curves clearly exhibited the transition zone before and after the breaking point for the plate sinkage test. As shown in the figures, the pressure–sinkage curves include two parts. The first part is prior to the breaking point that conveys the build-up zone. In this part of the curve, the plate acts upon a homogenous soil, where the effect of the hard layer does not exist, and the increasing soil strength is not yet significant. The soil deformation increases constantly, and the soil under the plate behaves similarly to when it is in the infinite thickness (without a hard layer or a specific depth). The pressure continuously intensifies with the relative sinkage, and the relationship between them is almost linear. The second part is following the breaking point that indicates the compaction zone or the zone of the soil bin bottom (the hard layer in a field) effect. Here, the compaction, as well as the deformation, increases rapidly. Further, above the rigid layer, the pressure almost does not decrease, because this layer modifies the pressure distribution in the soil body.

Table 4.1. Values of critical relative sinkage (breaking point) according to Eq. 4.1

H (cm)	D (cm)	H/D	$z_o/D=H/D-1.05$	$z_o/D=H/D-1.06$	$z_o/D=H/D-1.07$
18	10	1.8	0.75	0.74	0.73
	15	1.20	0.15	0.14	0.13
30	10	3	1.95	1.94	1.93
	15	2	0.95	0.94	0.93
	20	1.5	0.45	0.44	0.43
40	10	4	2.95	2.94	2.93
	15	2.67	1.62	1.61	1.60
	20	2	0.95	0.94	0.93

This extended portion from the transition zone to the specific depth has a varied load bearing capacity. Eq. 2.5 can be applying for the first part of the pressure–sinkage curve. A power regression analysis was carried out to determine the relationship between the applied pressure (p) and the relative sinkage (z_o/D) for soil thicknesses levels with diverse densities, as per Eq. 2.5. the Eq. 2.5 parameters results n and k shown in Table 4.2. The data were fitted to the power model with a high coefficient of determination (R^2).

The exponent n characterizes the deformation and compaction behaviour of soil under vertical loading. It is mainly influenced by the moisture content and particle size distribution of soil. The sinkage modulus (k) mainly depends on the soil type, density, and moisture content. According to Sitkei et al. (2019), at optimum moisture content, the exponent n has an average value of 0.8 and it decreases with increasing moisture content. In the current study the typical value of exponent n between 0.7-0.9 with some abnormalities as can be seen in Table 4.2, because the soil filled up in the soil bin as layers and not easy to control all the layers. Due to the equalizing ability of bigger plates, the results of 20 cm diameter plate are concerned as more definitive. The use of these data to establish generally valid relationships requires to reduce k -value to a common exponent $n=0.8$ as outlined in section 4.2.

4. Results and discussions

Table 4.2. Data of measurements and parameters of Eq. 2.5

Soil thickness, H (cm)	Density, ρ (g/cm ³)	Moisture content (%)	D (cm)	n	k (N/cm ²)	(R^2)
18	1.26	7.6%	10	1	8.552	0.97
			15	0.9	9.334	0.99
	1.36	7.3%	10	0.6	37.48	0.99
			15	0.7	42.14	0.99
30	1.16	8%	15	1.1	12.89	0.97
			20	1.1	18.24	0.98
	1.32	8%	15	0.7	24.81	0.97
			20	0.7	30.28	0.99
	1.54	8.3%	15	0.9	28.46	0.97
			20	0.7	30.055	0.99
	1.4	8%	20	0.7	13.56	0.99
	1.5	8%	20	0.7	17.96	0.99
40	1.16	8%	15	1	10.14	0.93
			20	1.2	16.91	0.97
	1.38	8%	15	0.7	25.27	0.95
			20	0.8	29.8	0.97
	1.5	8%	15	0.7	15.77	0.9
			20	0.7	22.94	0.93
	1.3	8%	20	0.9	10.43	0.97

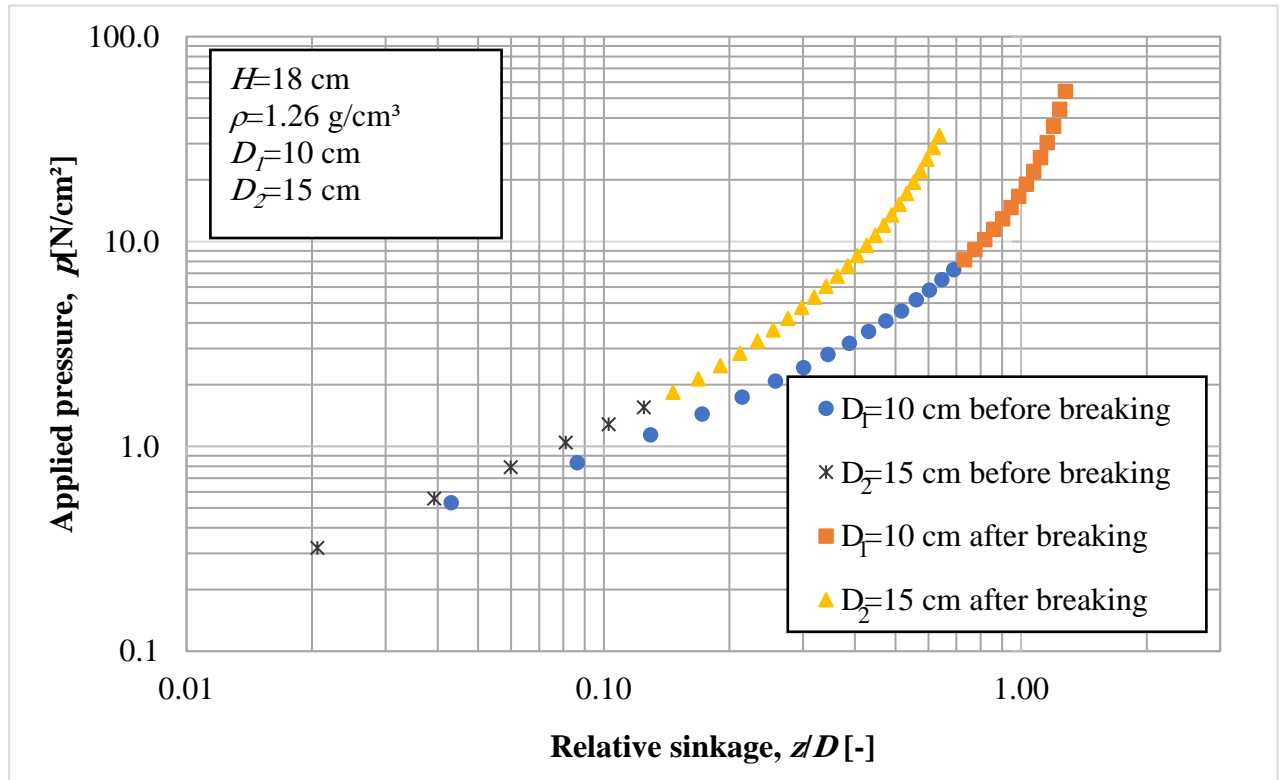


Fig. 4.8. Pressure-sinkage curves of soil thickness of 18 cm at density of 1.26 g/cm³

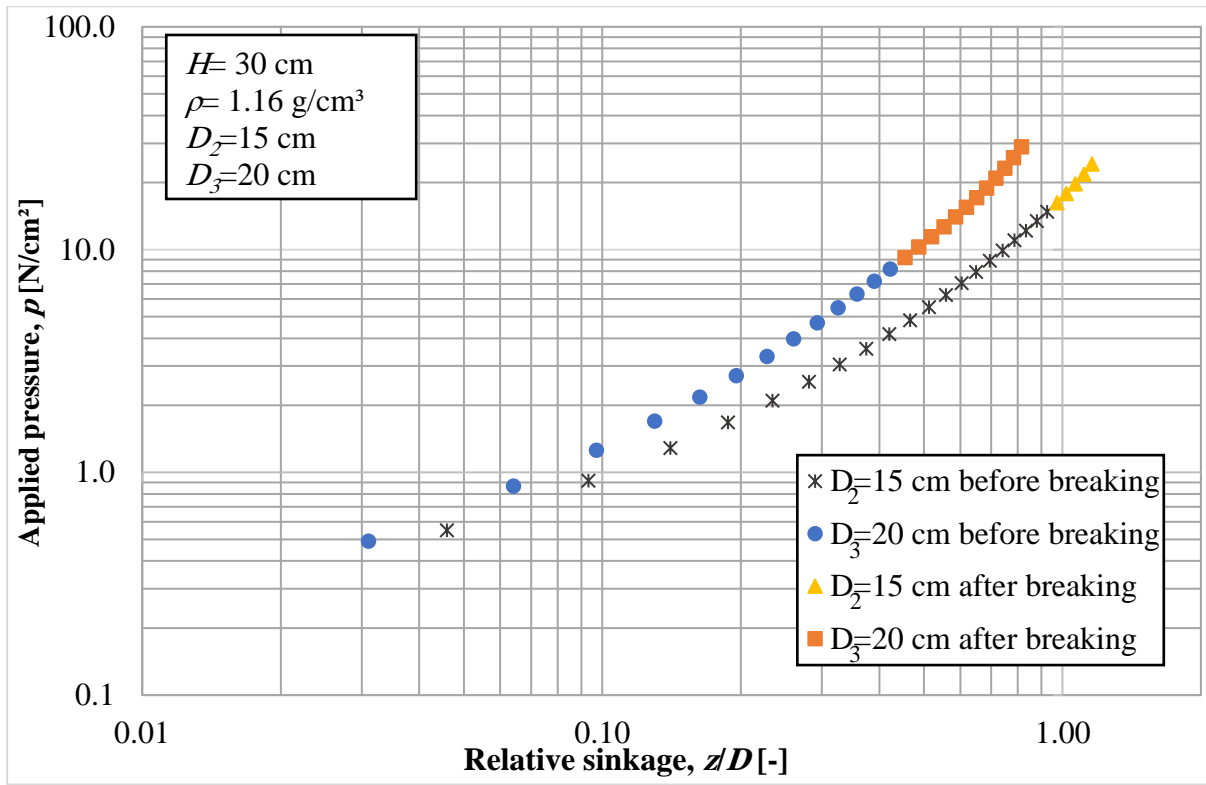


Fig. 4.9. Pressure-sinkage curves of soil thickness of 30 cm at density of 1.16 g/cm³

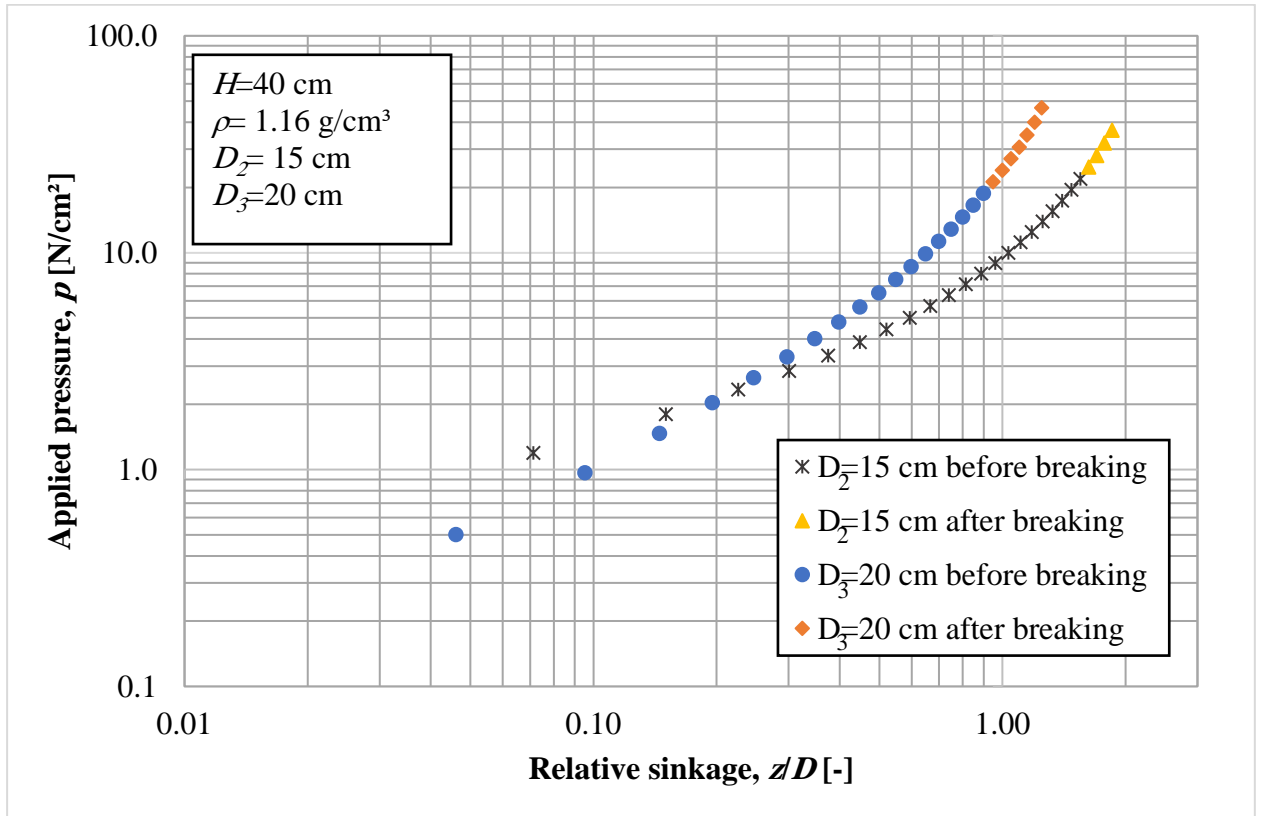


Fig. 4.10. Pressure-sinkage curves of soil thickness of 40 cm at density of 1.16 g/cm³

4.6. New pressure-sinkage relationship equation

The conventional pressure-sinkage models can be used for homogenous, infinite soil thickness when an examination of the impact of the hard layer is not required. It was intended that certain

proposals would be made for models that would consider the effect of the hard layer, but the models were too complicated and could not be applied. Hence, this section's main aim is to improve a simple pressure–sinkage model (shown in Eq. 2.5) to assess the affection of the rigid layer.

Most proposed pressure–sinkage models have tried to develop the sinkage modulus (k) as functions concerning the plate dimensions or wheel dimensions. These models have also regarded the sinkage exponent as a constant soil parameter that is not impacted by other factors. The exponent (n), as well as the sinkage modulus (k), remain constant in the present study for the first part of the pressure–sinkage curve. These soil parameters, however, do not remain constant for the second part, because the bottom of the soil bin impacts the pressure distribution while increasing compaction.

As an example, Fig. 4.11 shows measured pressure curve and the calculated load bearing factor k with breaking point as a function of relative sinkage. After the breaking point the curve steeply increase and do not follow a simple power function. The chosen exponential function gave a good approximation, and, at the same time, the use of a relatively simple evaluation method was possible. The calculation of breaking point gives a reliable orientation, but its actual position should always be checked. An error in breaking point estimate causes uncertainty in calculation of k -values just after the breaking point to the small differences in Δk .

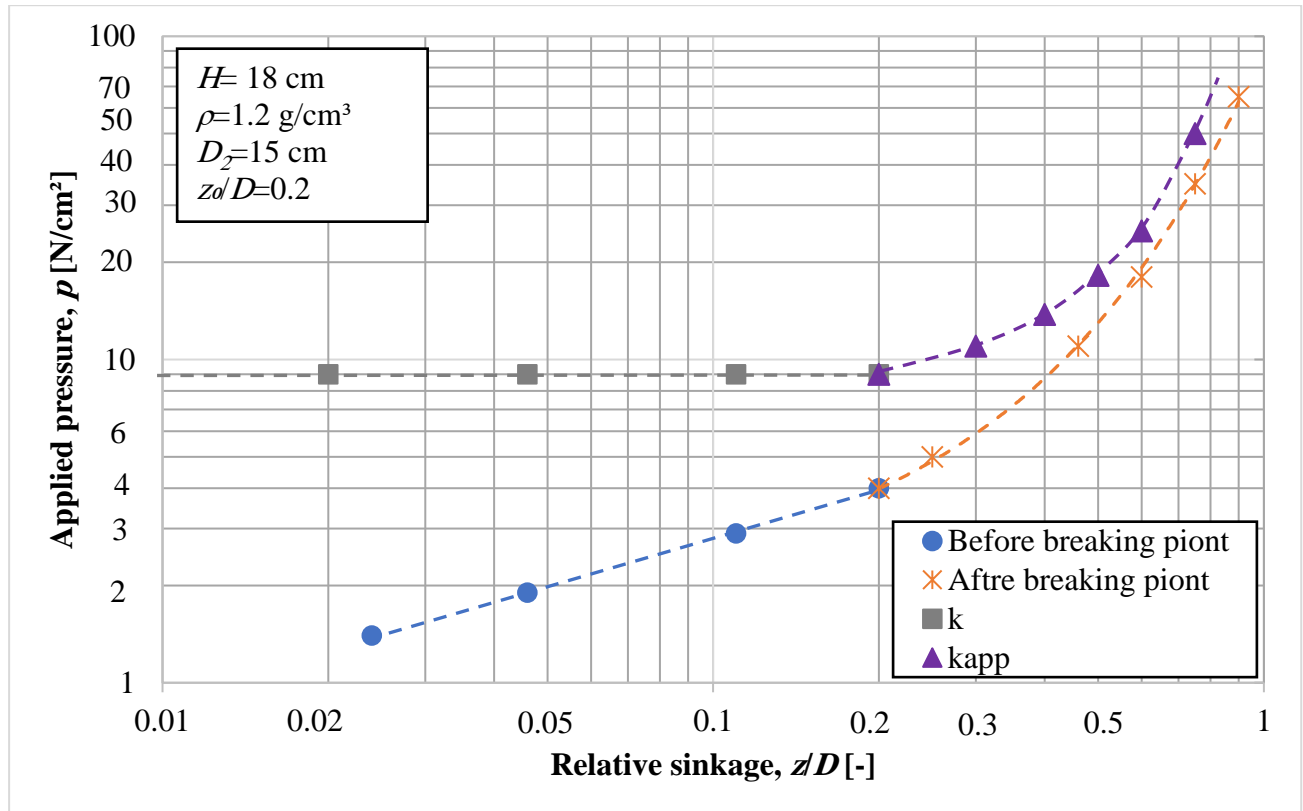


Fig. 4.11. Measured pressure curve before and after the breaking point ($z_0/D=0.2$) and the calculated load bearing factor k as function of relative sinkage

The experimental results concerning the three soil thickness levels at varied bulk densities show that a new pressure–sinkage model is possible by presenting a new sinkage modulus consisting of the affection of the soil's hard layer but retaining common plate-sinkage equation:

$$p = k_{app} \left(\frac{z}{D} \right)^n, \quad (4.9)$$

$$k_{app} = k + B \left(e^{c \left(\frac{z}{D} - \frac{z_o}{D} \right)} - 1 \right), \quad (4.10)$$

where k_{app} is the apparent sinkage modulus in unit N/cm², and B and c are constant.

For applying Eq. 4.10 there are two cases:

1. For the first part of pressure-sinkage curves before breaking points where $z/D < z_o/D$, the apparent sinkage modulus equals the common modulus:

$$k_{app} = k. \quad (4.11)$$

2. For the second part of pressure-sinkage curves after breaking points where $z/D > z_o/D$, the apparent sinkage is as seen in Eq. 4.10.

To simplify Eq. 4.10, we use the following notations:

$$\Delta k = k_{app} - k, \quad (4.12)$$

$$\Delta \left(\frac{z}{D} \right) = \frac{z}{D} - \frac{z_o}{D}, \quad (4.13)$$

By substituting these two Eqs. in Eq. 4.10, the following equation can be gotten:

$$\Delta k = B \left(e^{c \Delta \left(\frac{z}{D} \right)} - 1 \right). \quad (4.14)$$

The constants B and c can be determined by two measured points on the pressure-sinkage curve and by taking logarithm on both sides of Eq. 4.14, implicit equation can be gotten as seen in Eq. 4.15. By using implicit equation solver or Matlab program the constants B and c can be obtained.

$$\ln \left(\frac{\Delta k}{B} + 1 \right) = c \cdot \Delta \left(\frac{z}{D} \right). \quad (4.15)$$

An example shows the calculation way of constants B and c . The data of the example are tabulated in Table 4.3.

Table 4.3. The example data for finding B and c

z_o/D	Measured z/D	$\Delta(z/D) = z/D - z_o/D$	$k[\text{N/cm}^2]$	Measured k_{app}	$\Delta k = k_{app} - k$
0.2	0.3	0.1	9	11	2
	0.6	0.4		24.5	15.5

Substituting these data in Eq. 4.15, the following equations are obtained:

$$\ln \left(\frac{2}{B} + 1 \right) = 0.1 \cdot c, \quad (4.16)$$

$$\ln \left(\frac{15.5}{B} + 1 \right) = 0.4 \cdot c. \quad (4.17)$$

By using Implicit equation solver, the constants found to be $B=4.306$ and $c=3.815$.

For simplifying and reducing error in Eq. 4.14, a relation of Δk and $\Delta(z/D)$ shown in Fig. 4.12 proposed after many iterations of calculations. It is clearly seen the flexibility of the Eq. 4.10 at different values of B and c but convergent values at $\Delta(z/D) = 0.5$ where $\Delta k = 30$ [N/cm²]. Problems may arise if the reading of z_0/D is not accurate and if the first $\Delta(z/D)$ point is near to the breaking point.

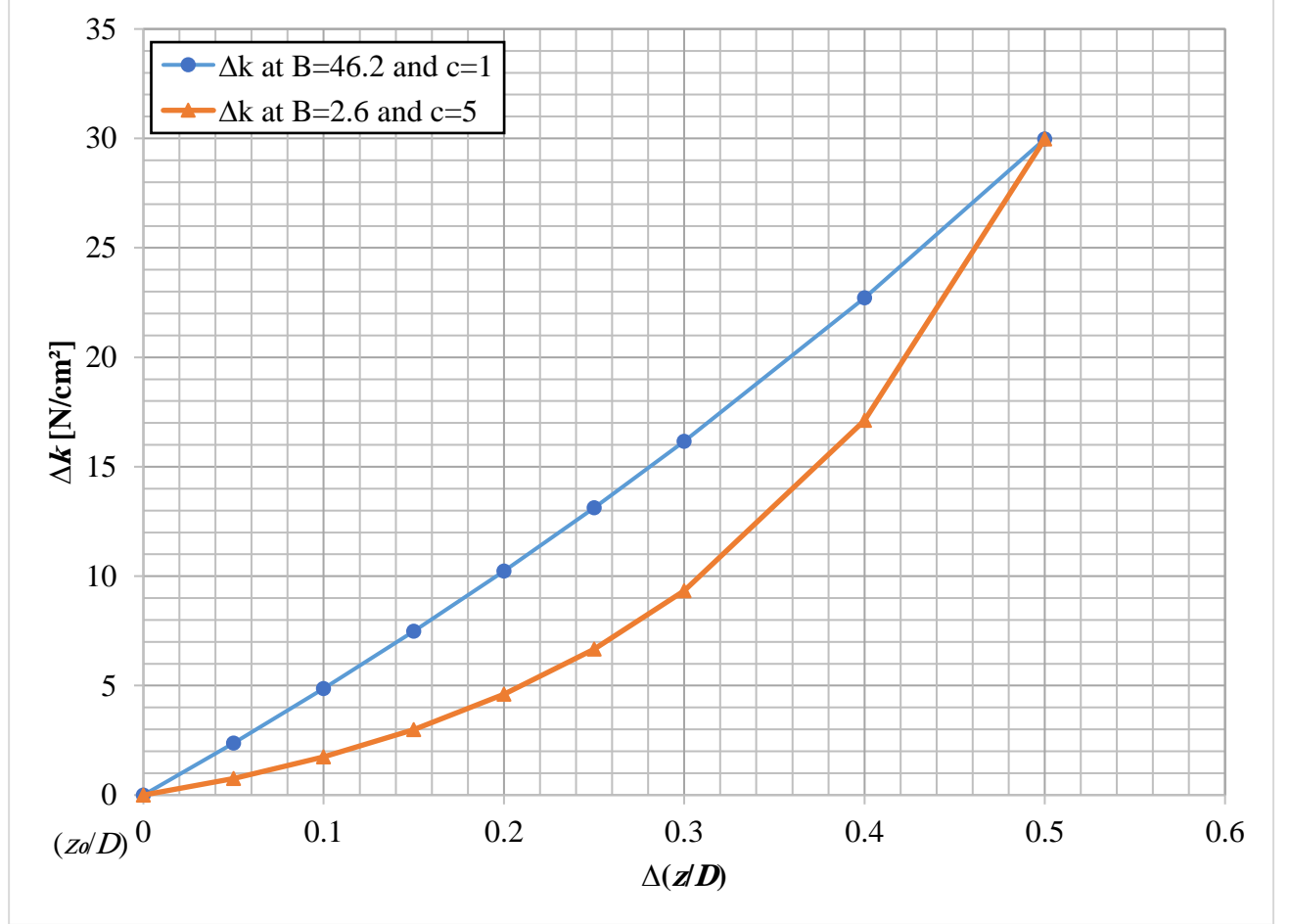


Fig. 4.12. Relations of Δk versus $\Delta(z/D)$ for the chosen function

Taking the range of B between 2 to 50 and c between 1 to 5, and $\Delta(z/D) = 0.5$ is considered as a fixed point for finding the feasible range for B and c . A relation of B and c shown in Fig. 4.13 can be deduced to define their range which is good in the calculations having different Δk values.

The processing of pressure-sinkage curves and k_{app} curves for diver's sinkage plate diameters at soil thicknesses of 18, 30 and 40 cm are shown in Figs. 4.14-4.23, The rest of the figures are shown in appendices A5.

In the first part of the pressure-sinkage curves, the build-up zone is subjected to Eq. 4.9. The equation's parameters were determined by applying regression analysis (listed in previous section in Table 4.2). As can be seen, the sinkage exponent (n) and sinkage modulus (k) did not change in the first part of the curve (before the breaking point). First term of Eq. 4.10 is applied for this part. The pressure increases as function of relative sinkage, as the logarithmic scale used to show the relation, thus, the relation between the pressure and relative sinkage is linear.

4. Results and discussions

The second part of the curves displays the interaction of compact zone with the rigid layer. As the deformation increases, the pressure is increasing with relative sinkage exponentially. The second term of Eq. 4.10 applied for this part. As can be seen in the Figs. 4.14-4.23 the values of k_{app} and the applied pressure are converging. Therefore, as the pressure increasing, the sinkage modulus k_{app} also increases, which means the load bearing capacity of soil is increasing as well.

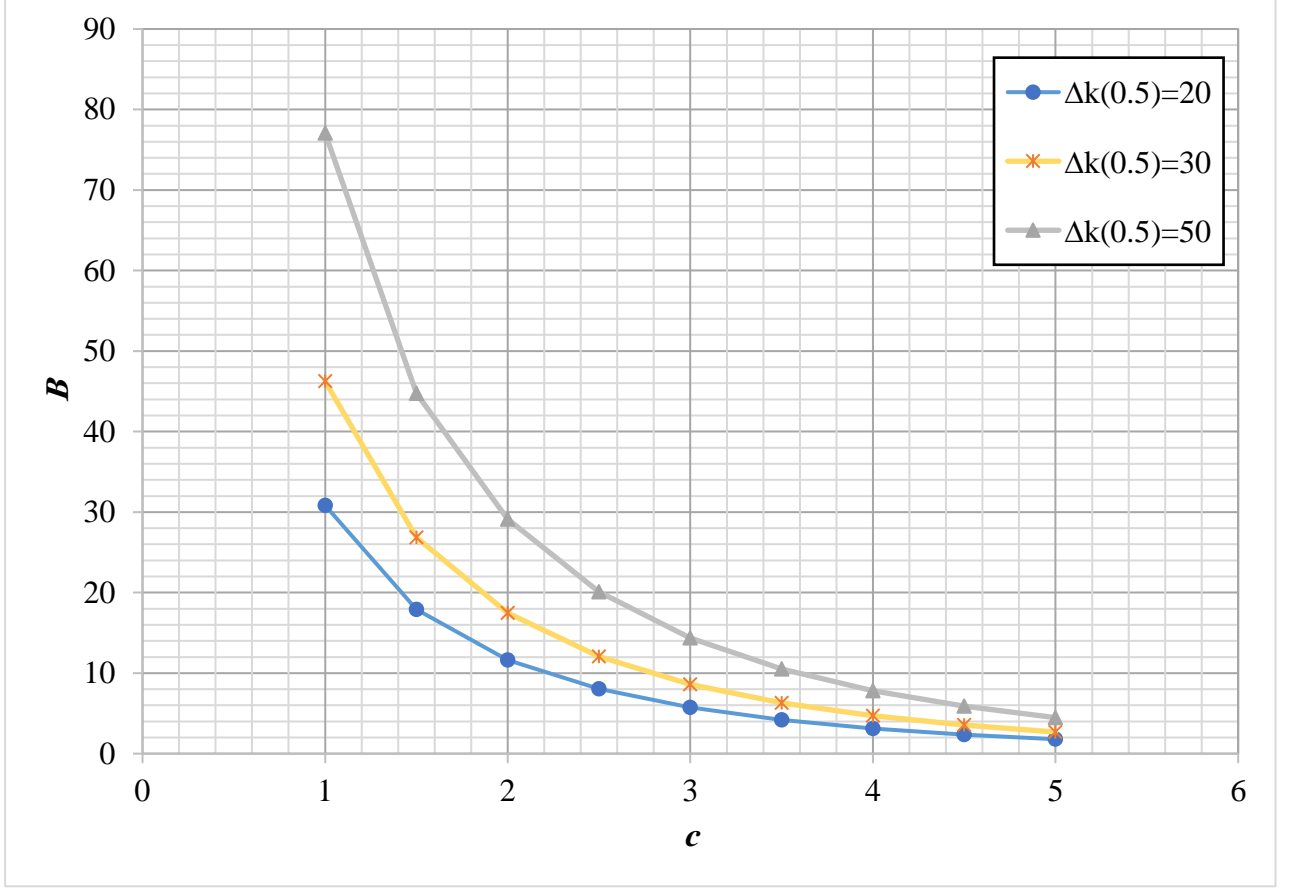


Fig. 4.13. Relation of constants B and c

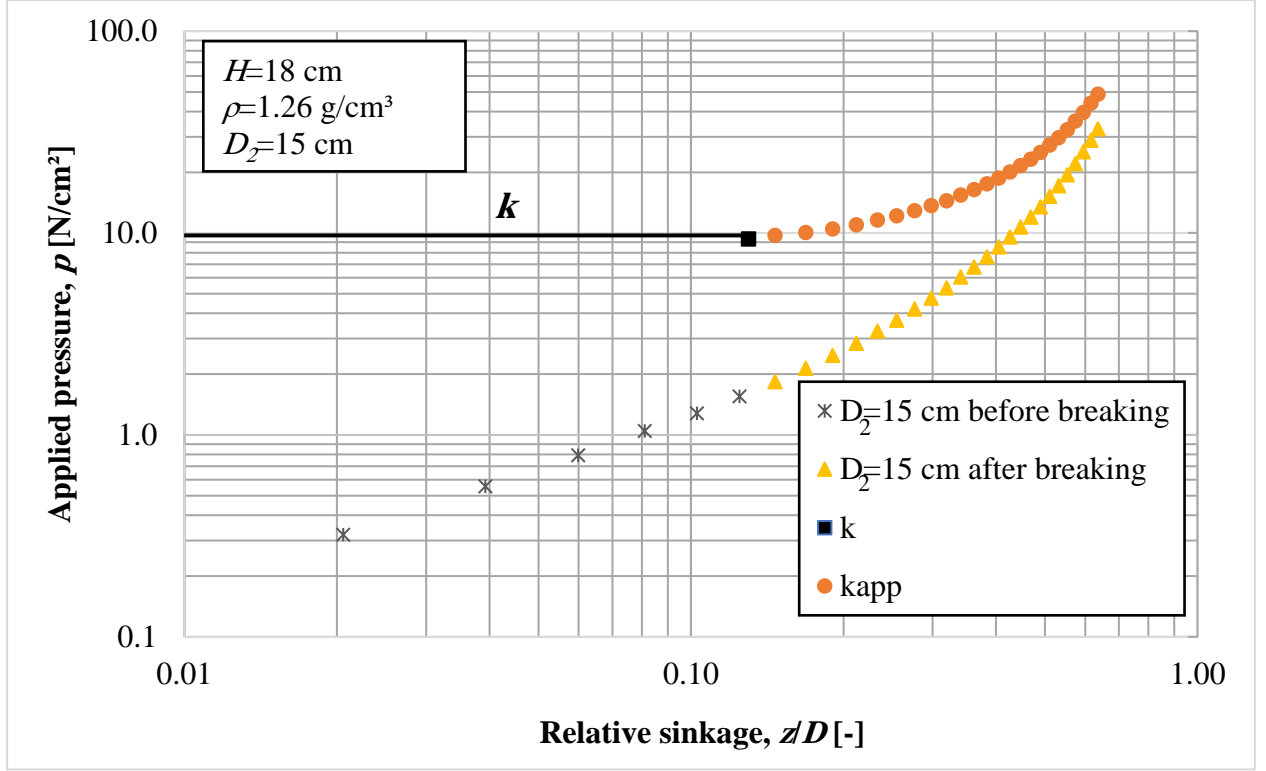


Fig. 4.14. Pressure-sinkage curves with k_{app} curves of soil thickness of 18 cm at bulk density of 1.26 g/cm³ and sinkage plate diameter of 15 cm

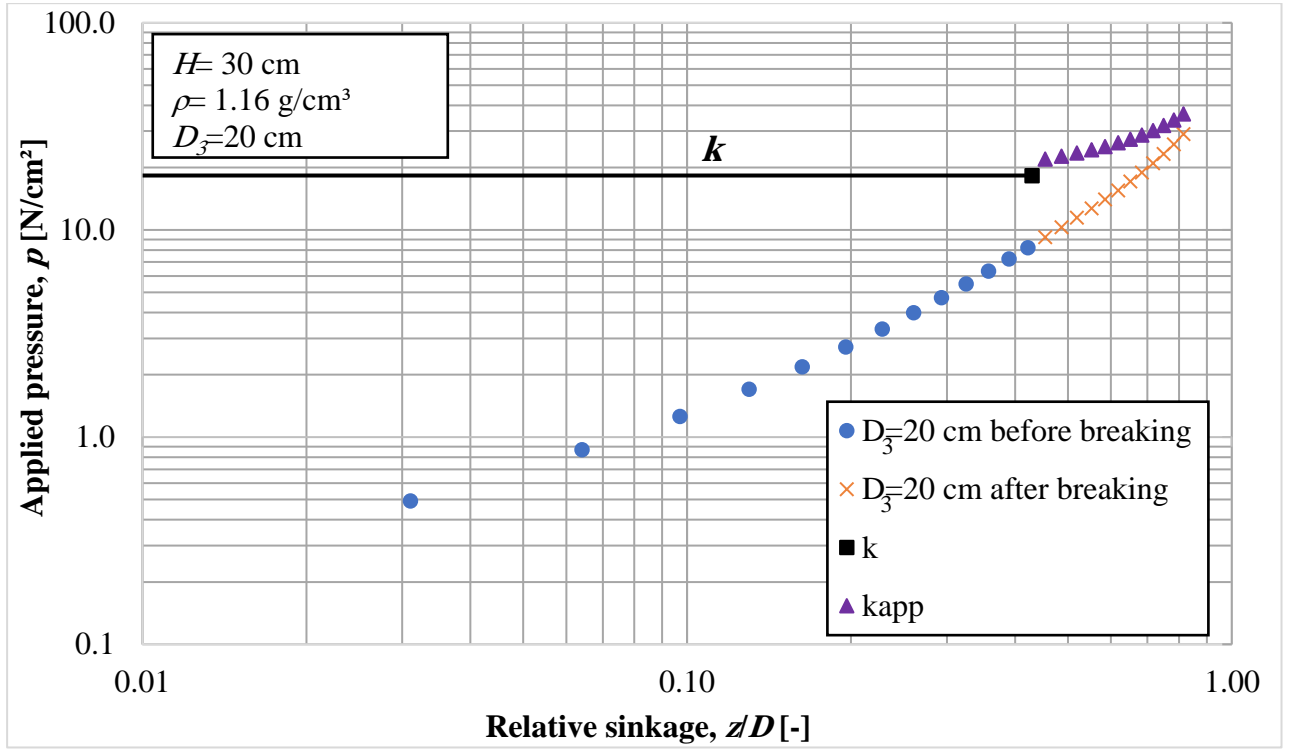


Fig. 4.15. Pressure-sinkage curves with k_{app} curves of soil thickness of 30 cm at bulk density of 1.16 g/cm³ and sinkage plate diameter of 20 cm

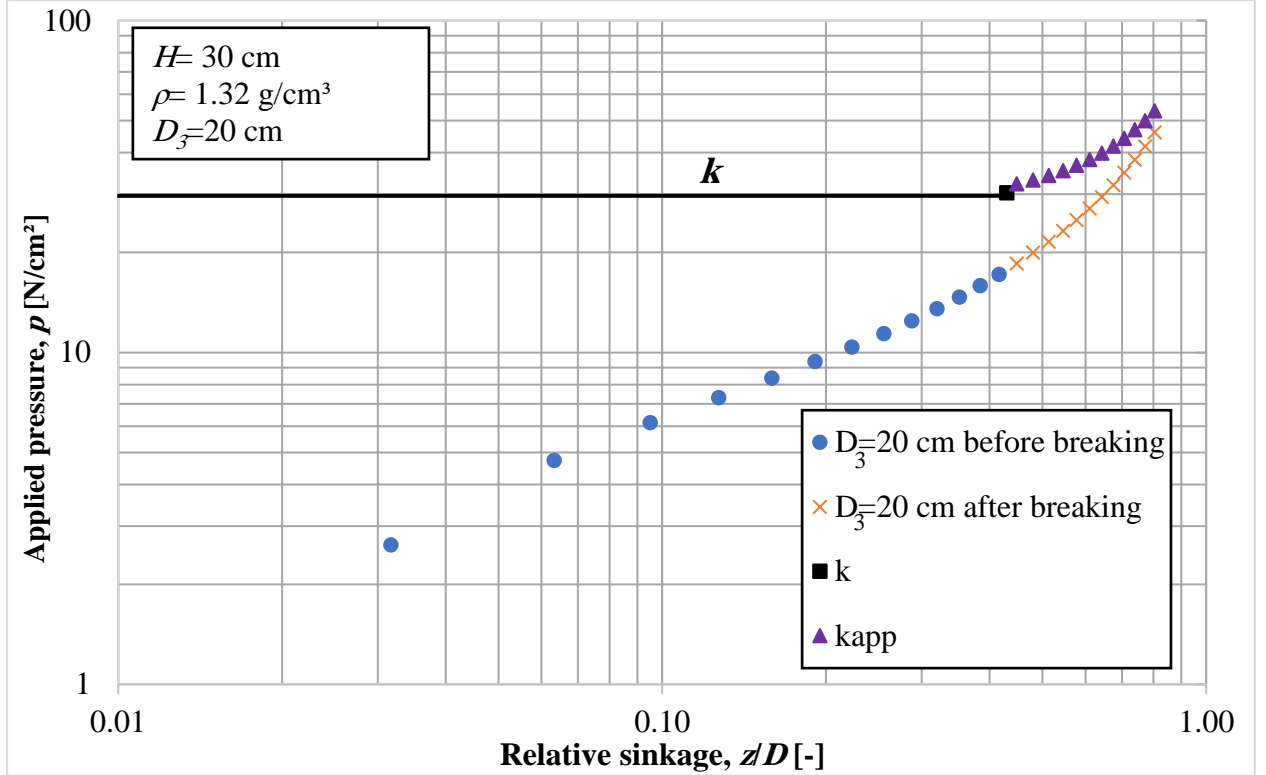


Fig. 4.16. Pressure-sinkage curves with k_{app} curves of soil thickness of 30 cm at bulk density of 1.32 g/cm³ and sinkage plate diameter of 20 cm

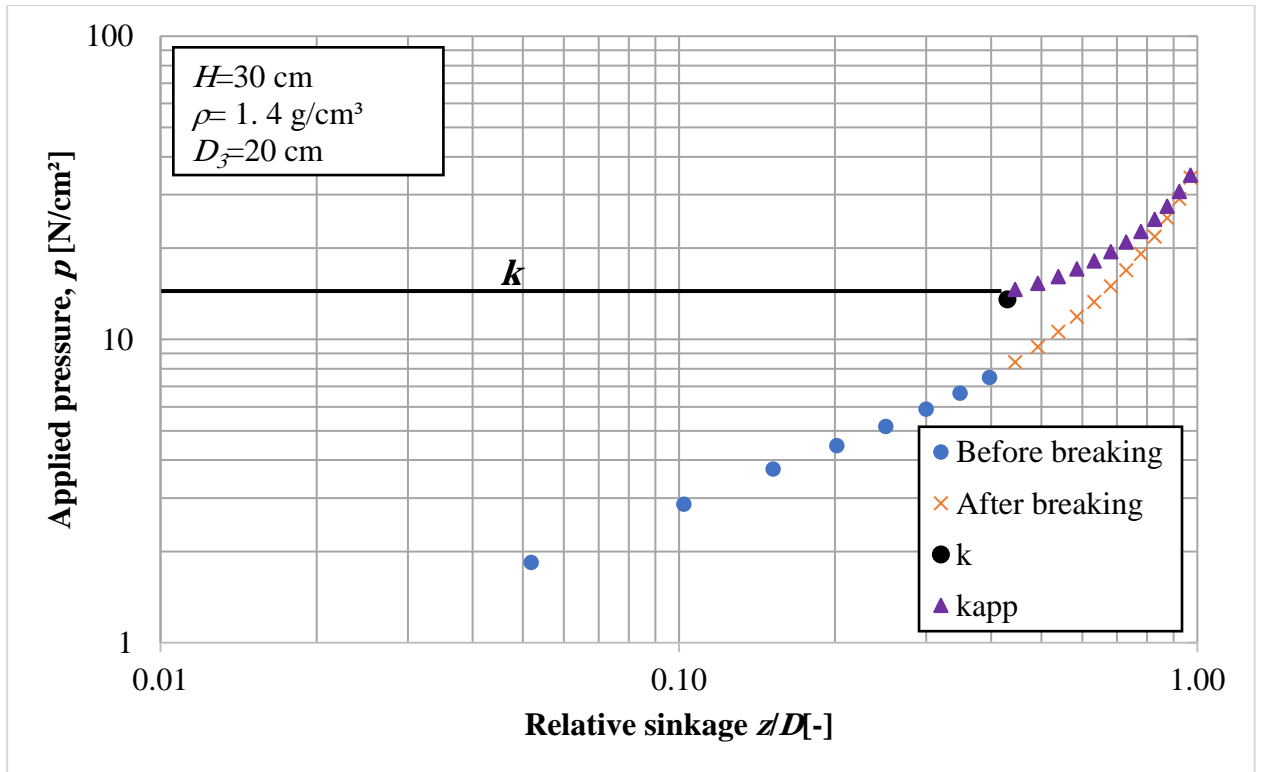


Fig. 4.17. Pressure-sinkage curves with k_{app} curves of soil thickness of 30 cm, plate diameter of 20 cm at bulk density of 1.4 g/cm³

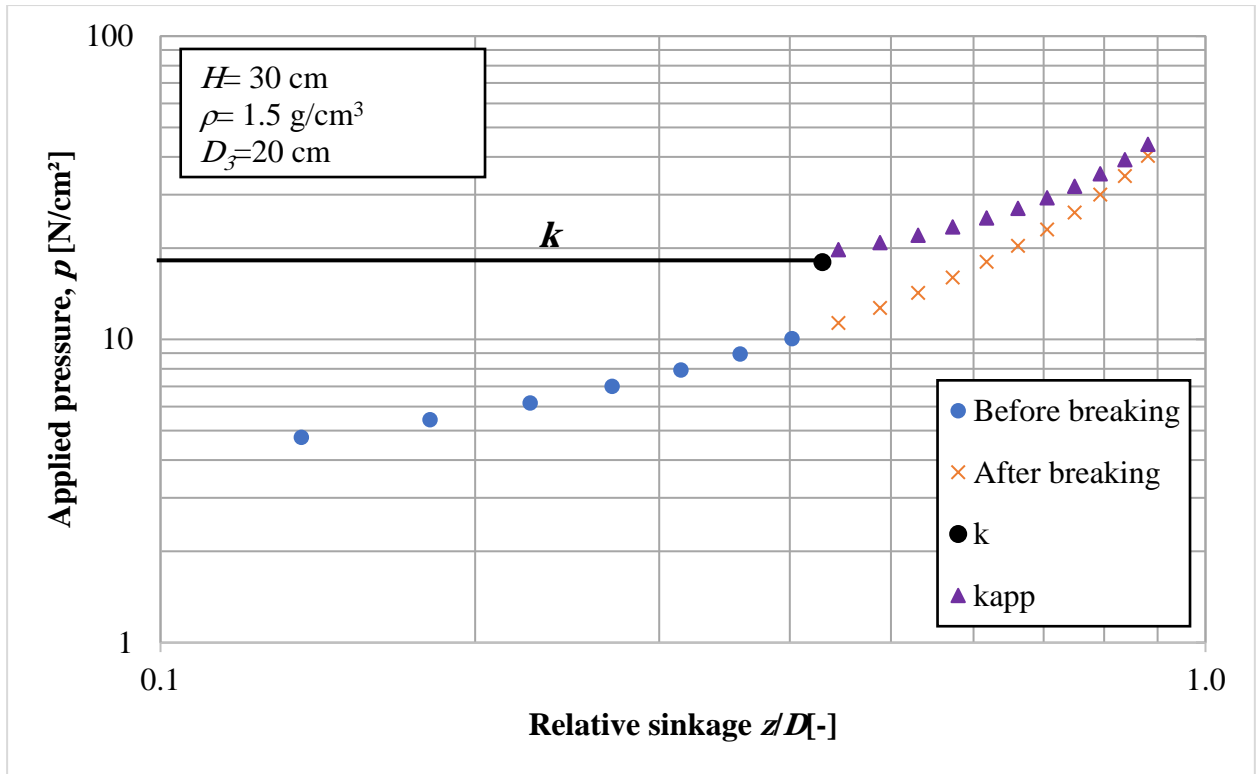


Fig. 4.18. Pressure-sinkage curves with k_{app} curves of soil thickness of 30 cm, plate diameter of 20 cm at bulk density of 1.5 g/cm³

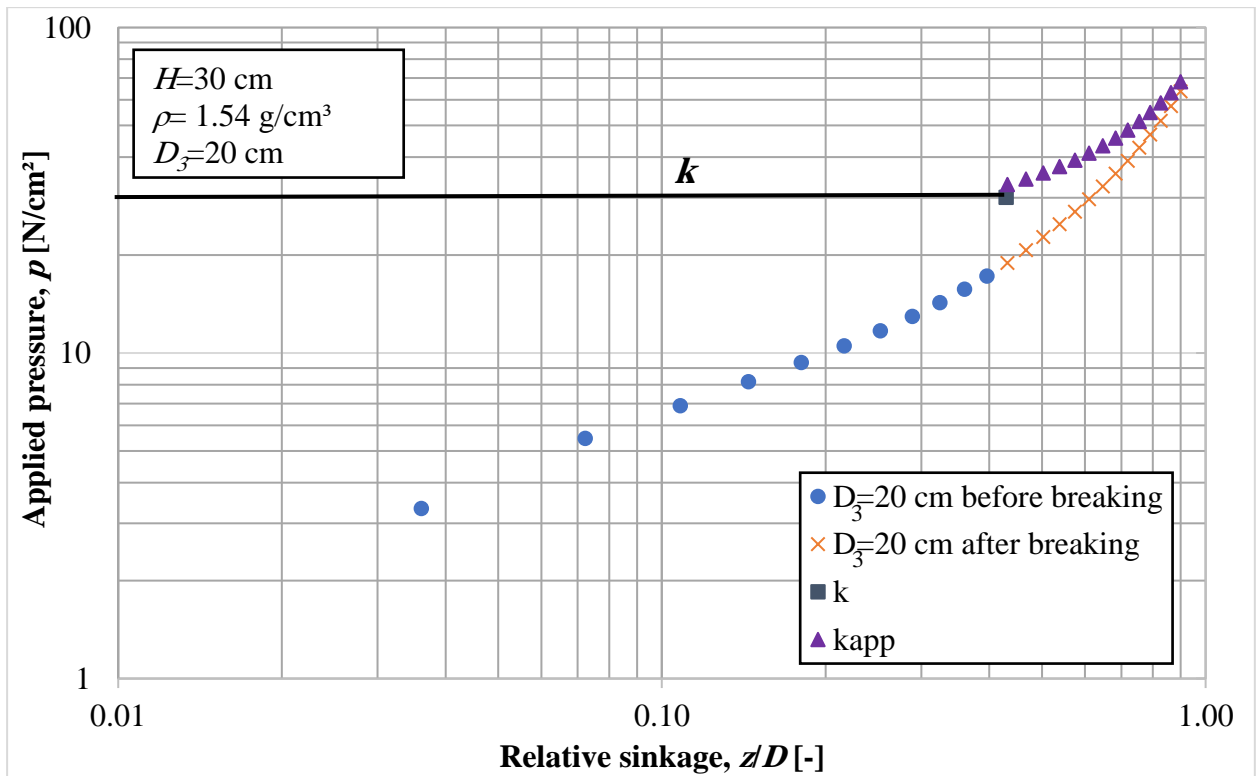


Fig. 4.19. Pressure-sinkage curves with k_{app} curves of soil thickness of 30 cm at bulk density of 1.54 g/cm³ and sinkage plate diameter of 20 cm

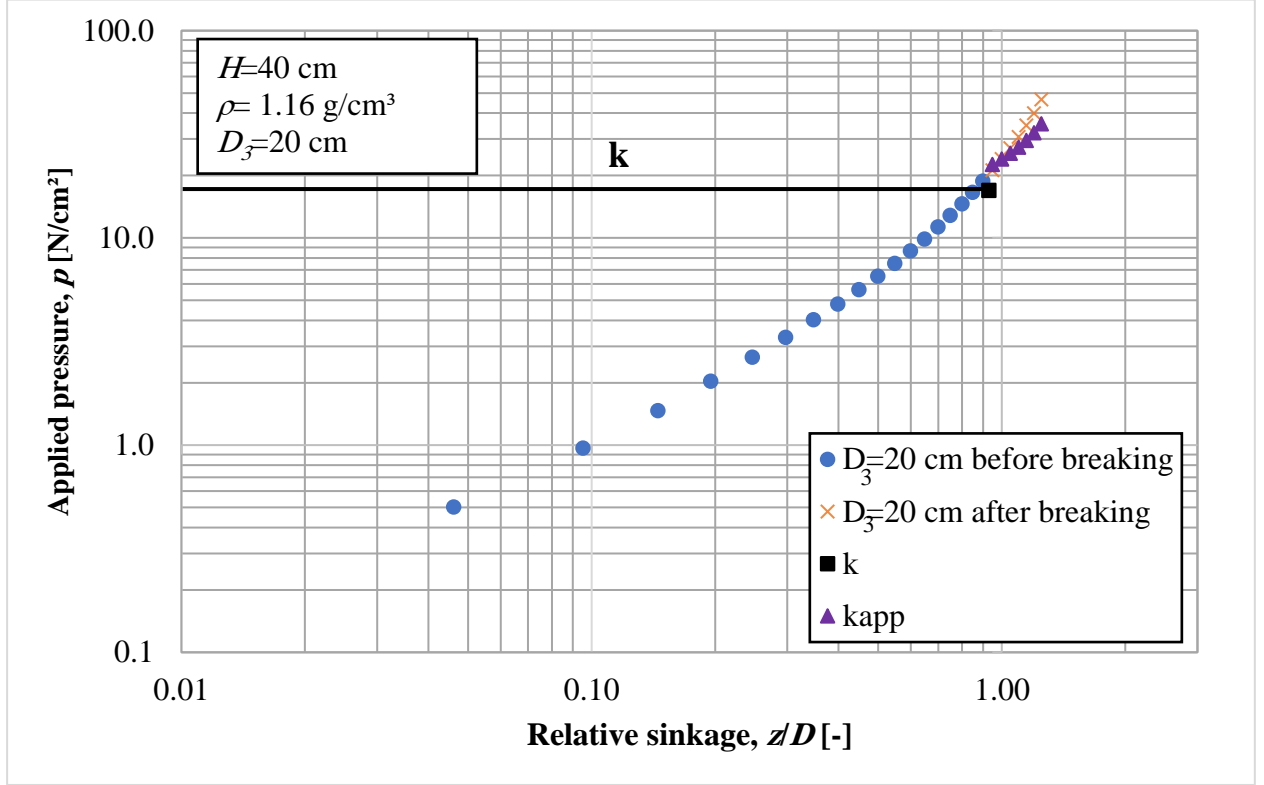


Fig. 4.20. Pressure-sinkage curves with k_{app} curves of soil thickness of 40 cm at bulk density of 1.16 g/cm³ and sinkage plate diameter of 20 cm

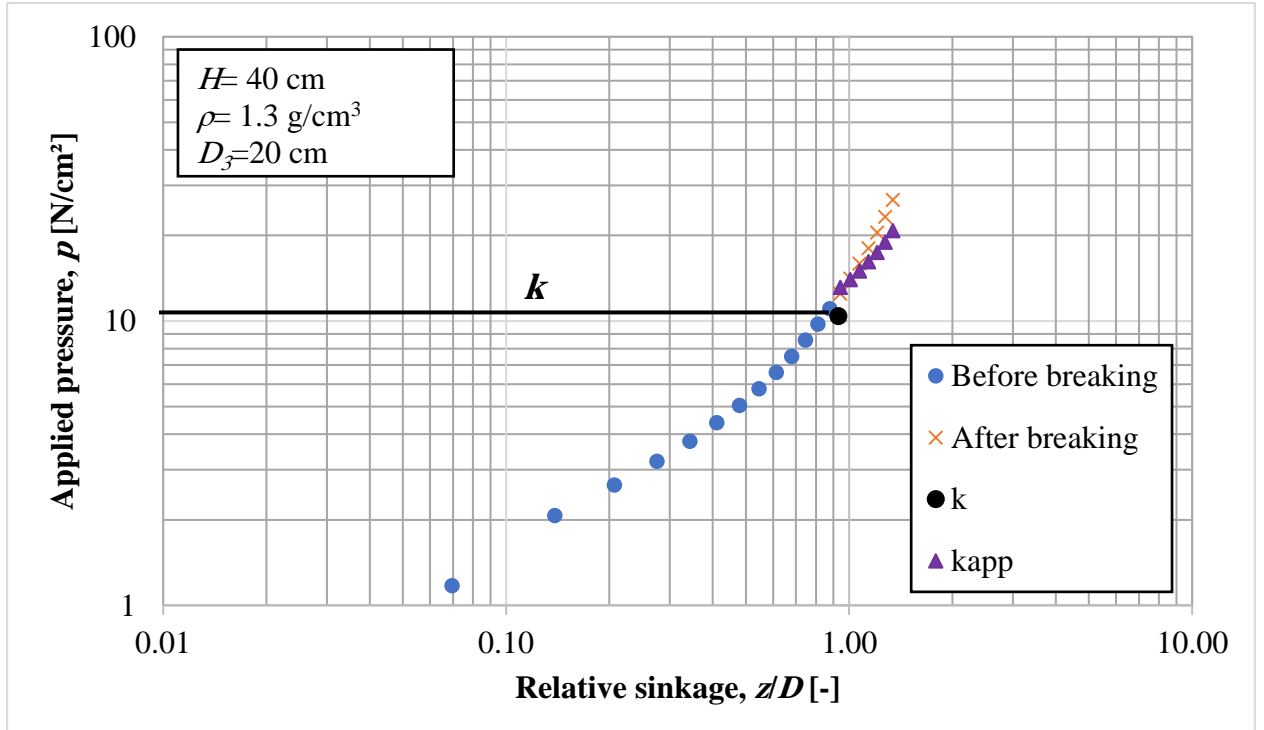


Fig. 4.21. Pressure-sinkage curves with k_{app} curves of soil thickness of 40 cm at bulk density of 1.3 g/cm³ and sinkage plate diameter of 20 cm

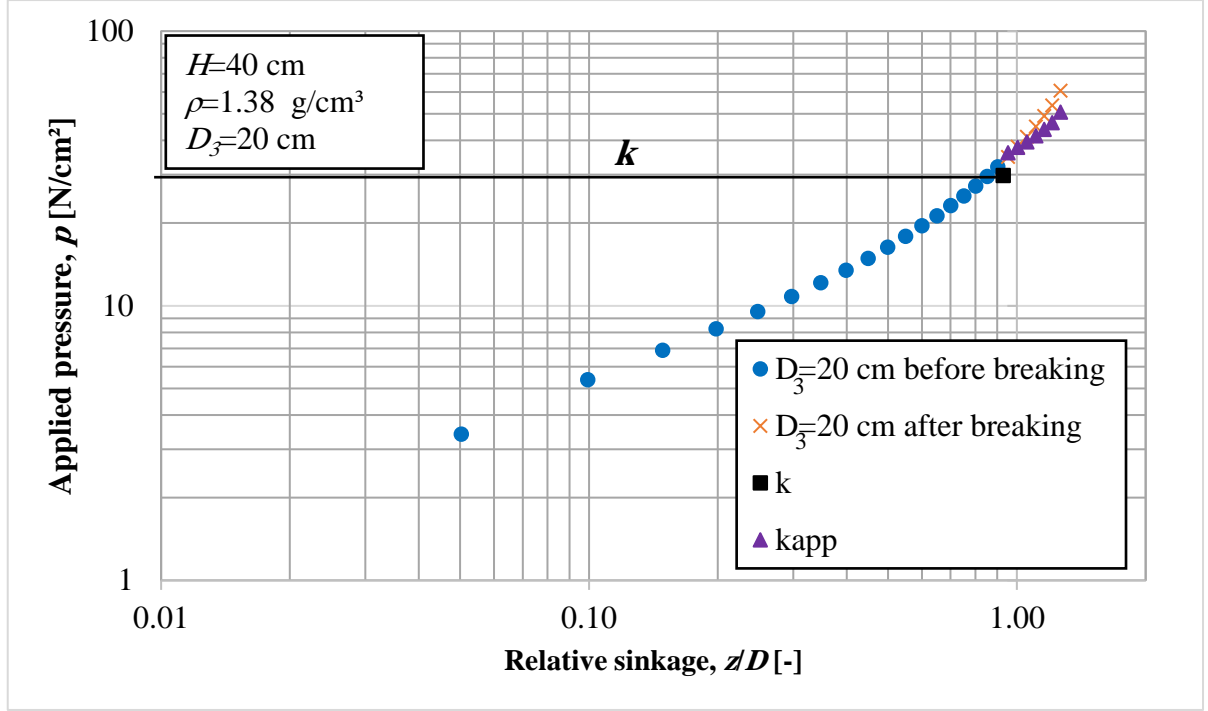


Fig. 4.22. Pressure-sinkage curves with k_{app} curves of soil thickness of 40 cm at bulk density of 1.38 g/cm³ and sinkage plate diameter of 20 cm

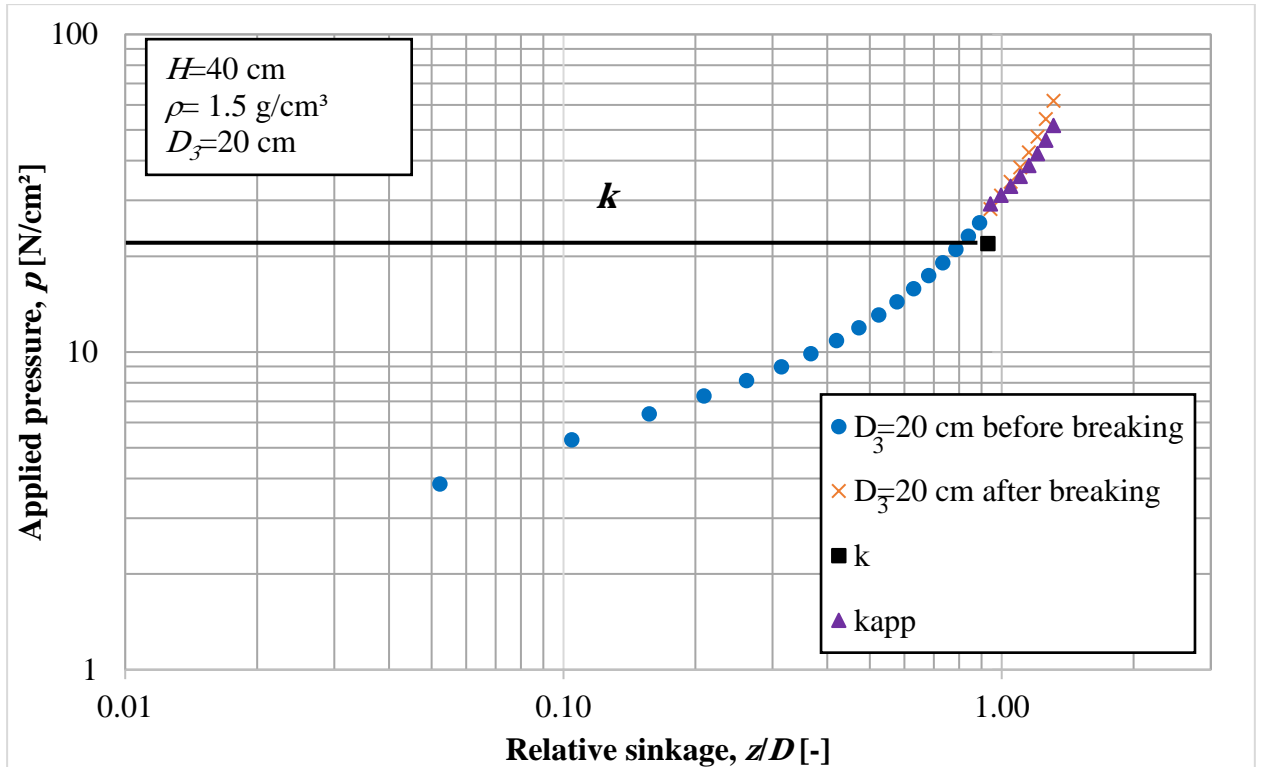


Fig. 5.23. Pressure-sinkage curves with k_{app} curves of soil thickness of 40 cm at bulk density of 1.5 g/cm³ and sinkage plate diameter of 20 cm

Table 4.4 presents the values of Δk at $\Delta(z/D) = 0.5$, k_{app} , B , and c , in terms of the soil thickness levels at diverse densities and different sinkage plate diameters. The table shows that there are

4. Results and discussions

anomalies in the outcomes of some of the tested conditions. This irregularity occurred because the soil filled up as layers in the soil bin. Therefore, it was difficult to ensure that all layers were in the same compressed level and soil distribution.

Eq. 4.14 applied to describe the relationship between Δk and $\Delta(z/D)$ by using the values of B and c which are shown in Table 4.4. Figs. 4.24-4.26 illustrate this relationship, along with the value of Δk at $\Delta(z/D) = 0.5$ for diver's sinkage plate diameters at soil thicknesses of 18, 30 and 40 cm and different densities. The rest of the figures are shown in appendices A6.

Table 4.4. The parameters of Eqs. 4.10 and 4.14

H [cm]	ρ [g/cm ³]	D [cm]	k [N/cm ²]	Δk (0.5) [N/cm ²]	k_{app} (0.5) [N/cm ²]	c	B
18	1.26	10	8.552	27.5	36.1	2.5	11.05
		15	9.334	39.3	48.7	2.5	15.78
	1.36	10	37.48	22.2	59.7	1.5	18.76
		15	42.14	23.3	65.4	1.5	19.80
30	1.16	15	12.89	22.4	35.3	2	13.03
		20	18.24	27.0	45.2	2	15.72
	1.32	15	24.81	35.0	59.8	2.5	14.04
		20	30.28	46.1	76.4	2.5	18.53
	1.54	15	28.46	49.6	78.0	2.5	19.90
		20	30.05	42.4	72.4	2.5	17.01
	1.4	20	13.56	17.20	30.76	2	10.33
	1.5	20	17.96	31.12	49.08	2.5	12.50
40	1.16	15	10.14	29.0	39.1	2.5	11.64
		20	16.91	38.0	54.9	2.5	15.24
	1.38	15	25.27	45.0	70.3	2.5	18.09
		20	29.8	40.6	70.4	2.5	16.30
	1.50	15	15.77	41.4	57.1	2.5	16.61
		20	22.94	46.7	69.6	2.5	18.74
	1.3	20	10.43	19.27	29.7	1.5	12.25

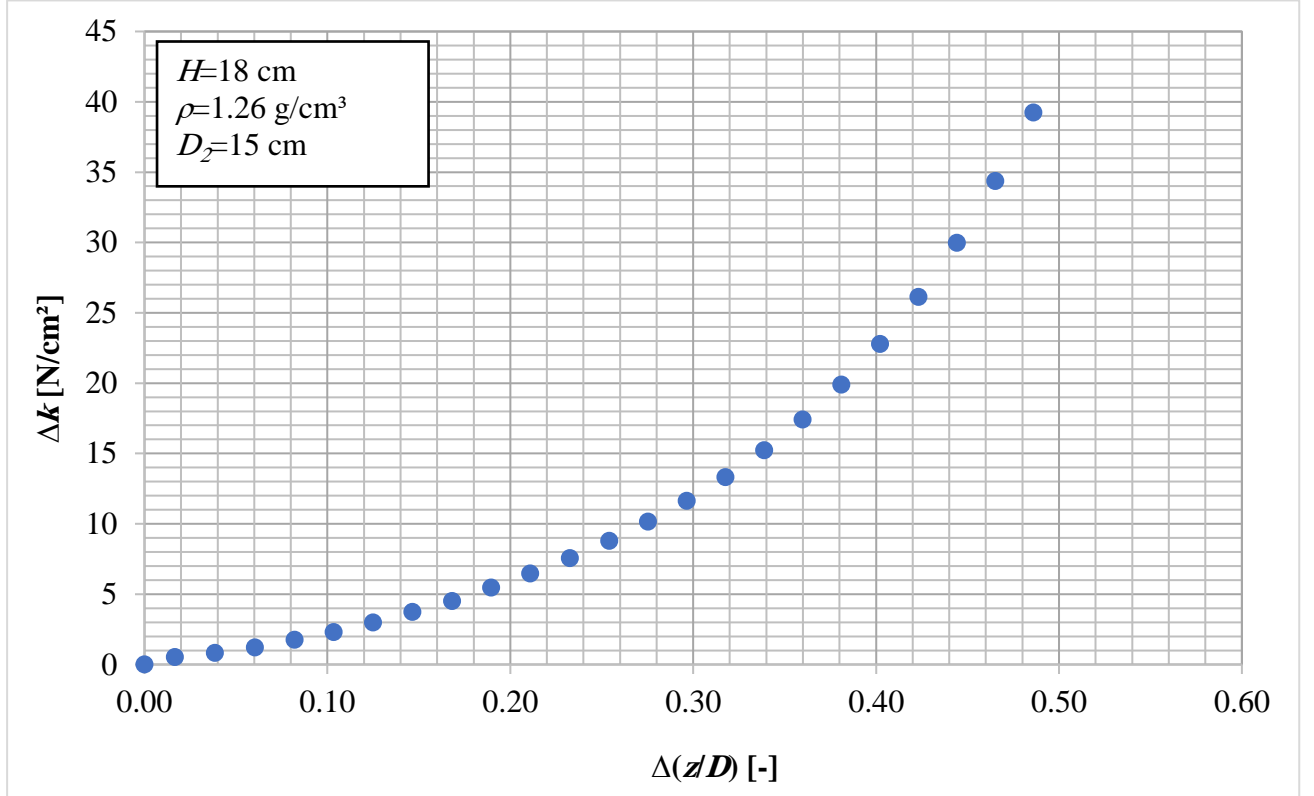


Fig. 4.24. Relation of Δk and $\Delta(z/D)$ of soil thickness of 18 cm at bulk density of 1.26 g/cm^3 and sinkage plate diameter of 15 cm

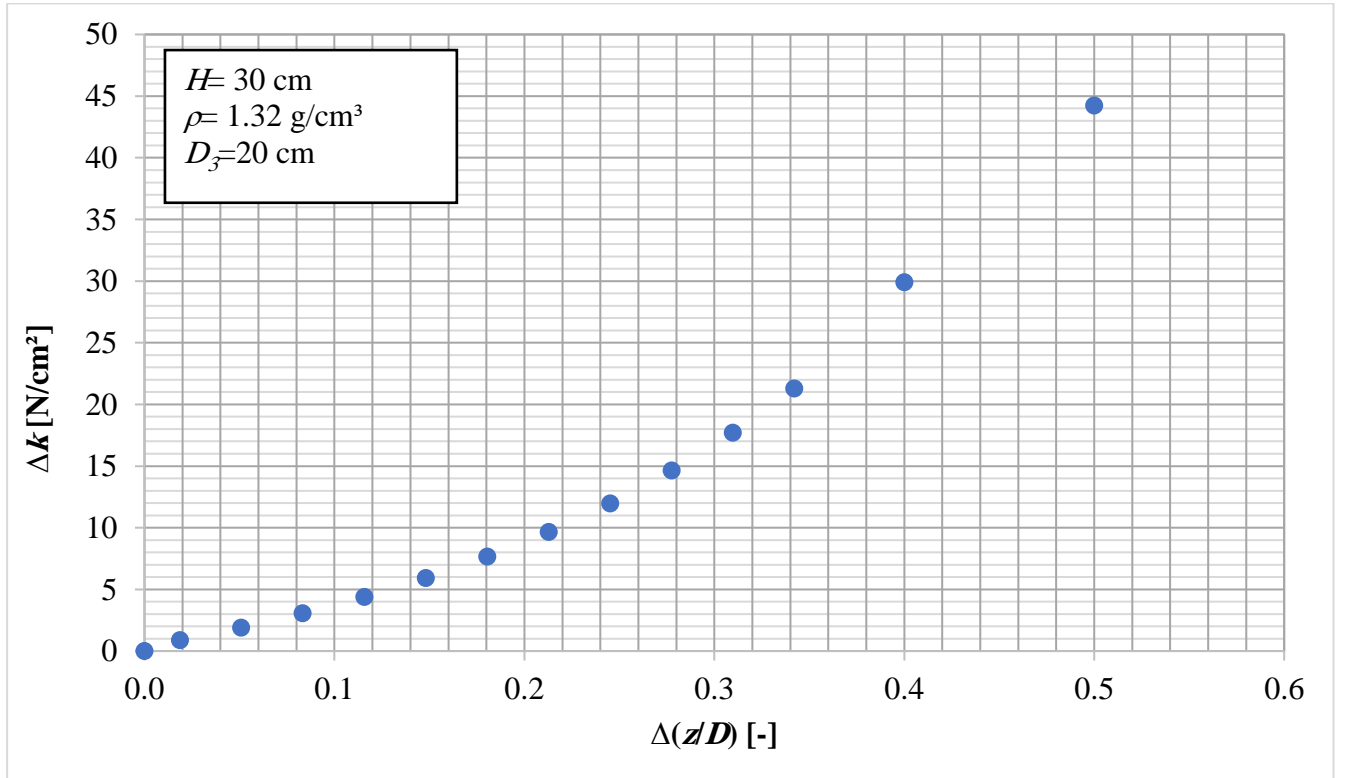


Fig. 4.25. Relation of Δk and $\Delta(z/D)$ of soil thickness of 30 cm at bulk density of 1.32 g/cm^3 and sinkage plate diameter of 20 cm

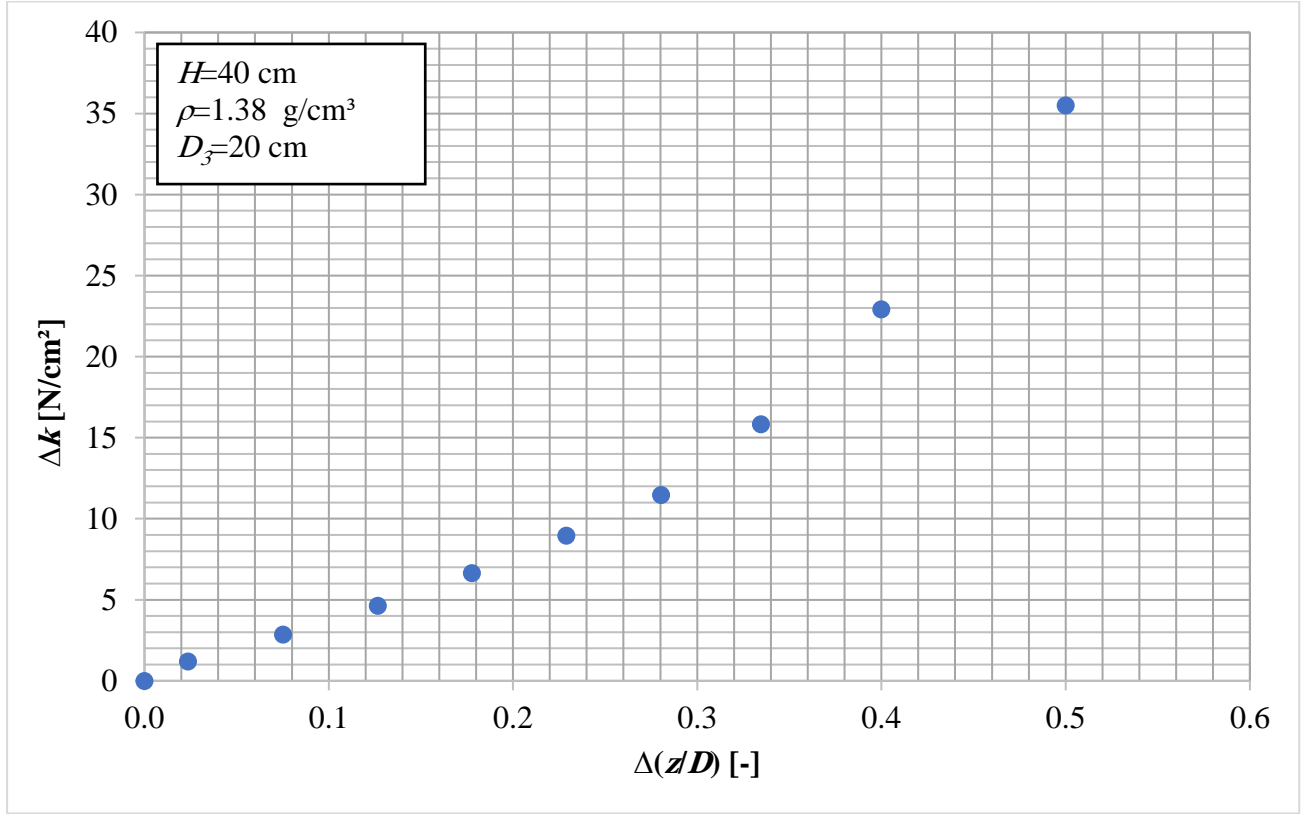


Fig. 4.26. Relation of Δk and $\Delta(z/D)$ of soil thickness of 40 cm at bulk density of 1.38 g/cm³ and sinkage plate diameter of 20 cm

4.7. Effect of finite depth on the load bearing capacity factor

Processing of experimental results for proving the validity of the suggested $k=f(\rho, H/D)$ relationship is given in Fig. 4.27. We mostly used the experimental results with plate diameter of 20 cm but not exclusively. For example, $H/D=3$ we used data with $H=30$ cm and $D=10$ cm.

From the figure it may be stated that the experimental results follow well the general regularity which is further supported with the limited number of data for $H/D=3$. As usually, soil measurement data have a given scattering due to varying soil properties (homogeneity) and imperfect soil preparation in soil bin for a given constant density.

Measurements with $H/D=0.9$ gave also some useful results. The compacted zone under the plate continuously develops and up to z/D ratios of 0.1 and 0.15 no interaction occurs with the bottom rigid layer.

The proof of the dimensionless load bearing number is demonstrated in Fig. 4.28. The $H/D=1$ line contains measurement data for $H/D=0.9$ and 1.2, while the second line for $H/D=1.8$ and 2. Again, despite of a given scattering, the dimensionless number seems to be constant for a wide range of soil densities which encompasses the whole range appearing in the practice.

It is concluded that the load bearing capacity of soil can be generalized including new influencing variables such as the soil density and the relative thickness of the homogenous soil layer.

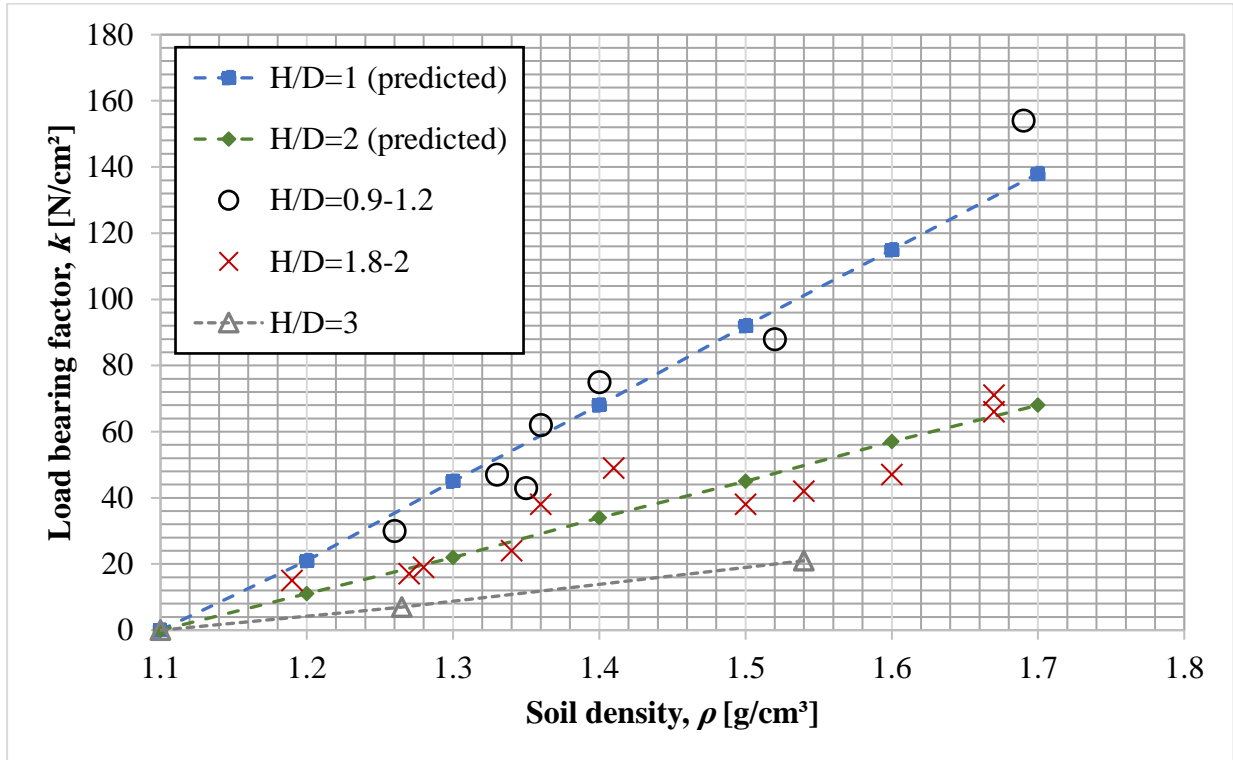


Fig. 4.27. Experimental and predicted load bearing capacity factor as a function of soil density for different H/D ratio

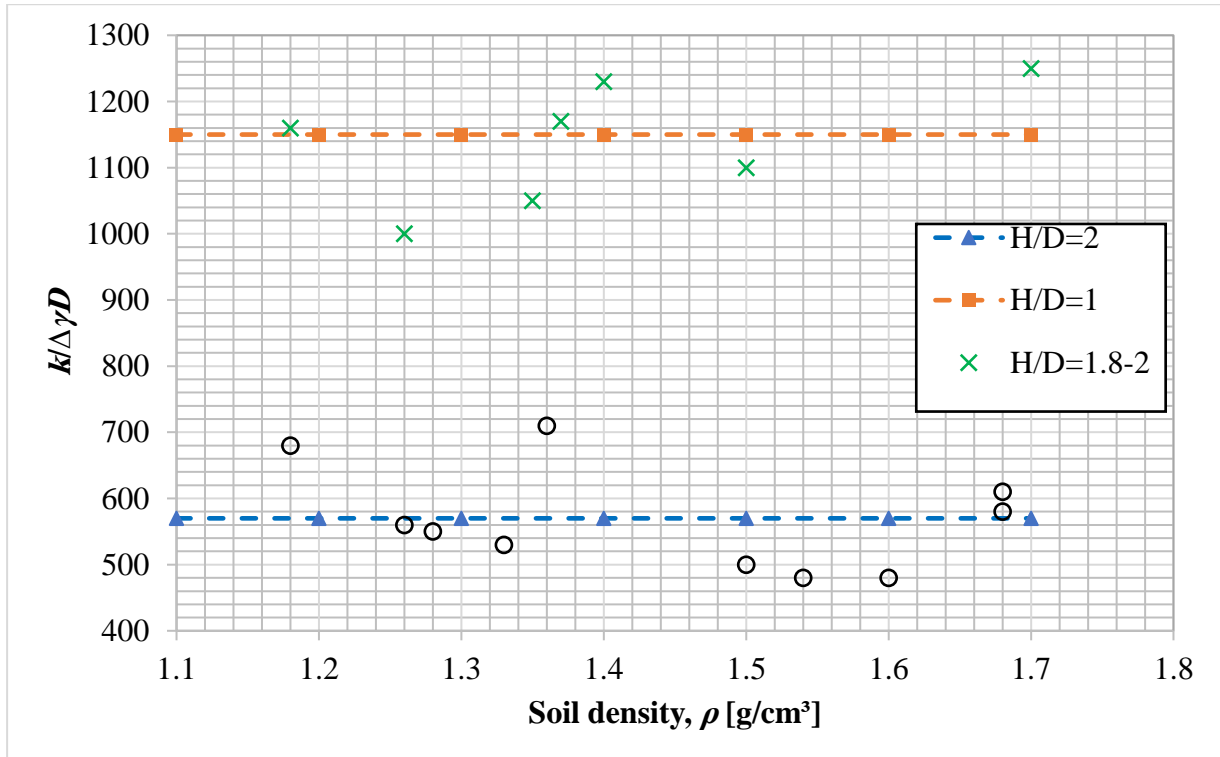


Fig. 4.28. Load bearing capacity number as a function of soil density for two H/D ratios

4.8. Generalized pressure-sinkage equation

Based on the dimensionless load bearing number, a new pressure number, also in dimensionless form, has been derived. The proof of this pressure number is given in Fig. 4.29 using experimental data for two H/D ranges as a function of relative sinkage. The experimentally determined points are well grouped along the previously suggested lines for different H/D ratios. This finding indicates the validity of expected general regularity for the homogenous finite half-space. Important, that the relative soil thickness is a new and distinct variable influencing soil deformation which should be taken into account.

The examined H/D range encompasses the practical cases since the actual soil layer is hardly more than 40 cm and the loading area is rarely less than 20 cm diameter. But even some measurement points for $H/D=3$ in Fig. 4.27 suggest that the influence of the H/D ratio on the pressure number may be valid also outside of the examined range. At the same time, as previously stated, the validity of H/D influence cannot be extended to infinity.

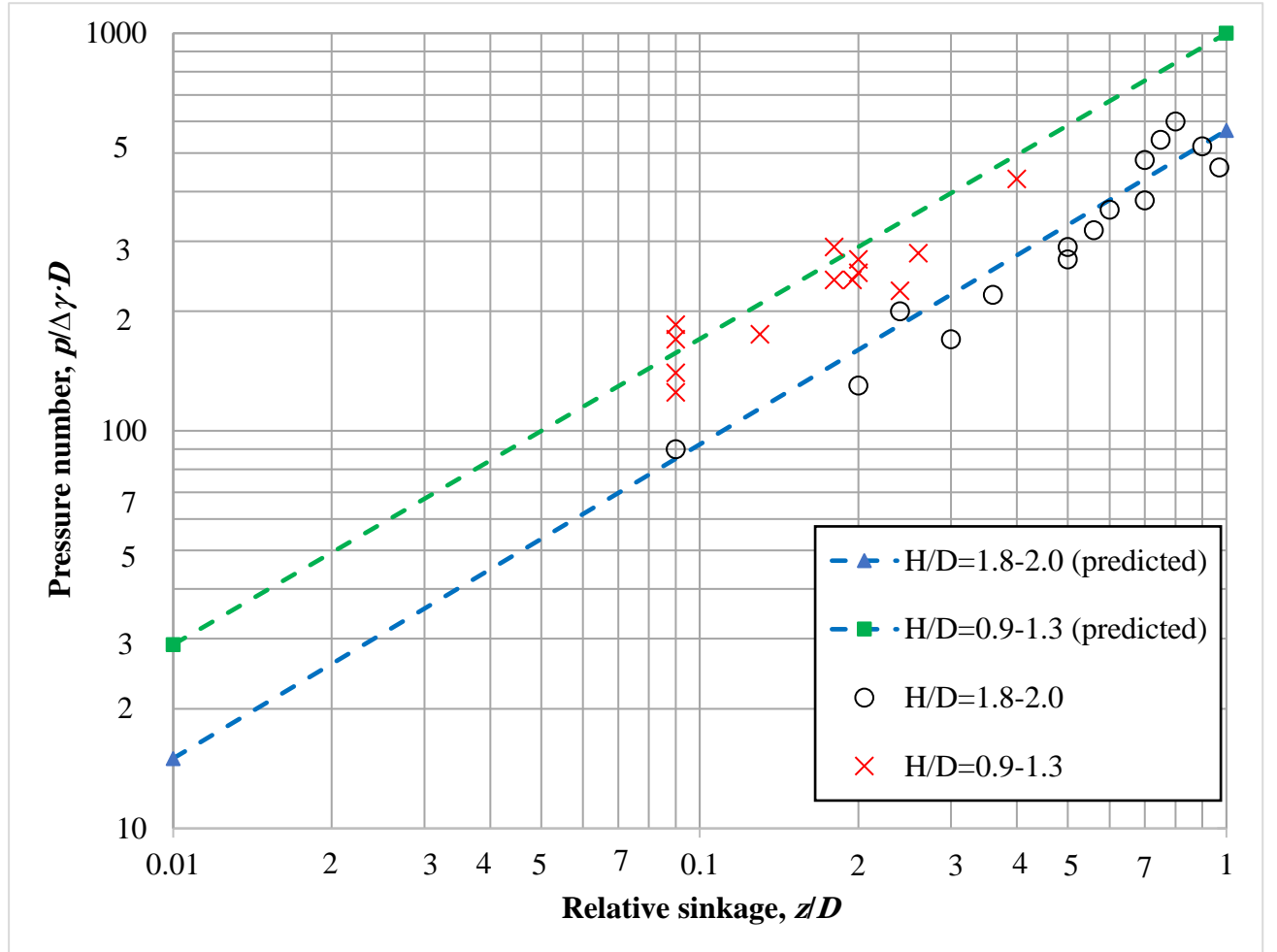


Fig. 4.29. Plot of pressure number as a function of relative sinkage for different soil thickness ratios H/D

4.9. Load bearing capacity increment due to rigid layer interaction

Theoretical considerations and preliminary indicated that, as a result of interaction between the compacted soil cone and hard pan, a definite increment of load bearing capacity may be expected. Using the developed evaluation method, Fig. 4.30 demonstrates the experimental results as a

4. Results and discussions

function of soil density for different H/D ratios. The increment is related to $\Delta(z/D) = 0.4$ values because, in the most cases of the measured $p = f(z/D)$ functions, it was available for processing. It is striking that the relative thickness of the soil (H/D) has even higher effect on the load bearing increment than the soil density. Therefore, we show the dominant influence of the H/D ratio in another coordinate system in Fig. 4.31. Note, however, that the influence rapidly decreases for higher H/D ratios.

Concerning practical questions, the following may be stated. The finite thickness of deformable soil may increase the load bearing capacity depending on the critical relative sinkage z_0/D ratio. The wheel sinkage is associated, however, with rolling resistance which depends on the relative wheel sinkage an exponent of 0.76. Therefore, it is only favorable smaller z_0/D ratio to utilize the increase in load bearing capacity.

For comparison, we take a tyre diameter $d=160$ cm and soil thickness $H=35$ cm, and varying contact D from 20 to 30 cm. The calculated results are summarized in the Table 4.5.

Table 4.5. the calculated result of tyre

D , cm	H/D	z_0/D	z_0 , cm	z_0/d	Rolling resistance coefficient
30	1.1667	0.1667	5	0.0313	0.1
25	1.4	0.4	10	0.0625	0.152
20	1.75	0.75	15	0.094	0.196

It can be seen that decreasing the contact diameter from 30 to 20 cm, a better load carrying capacity would only be attainable on the burden of double rolling resistance due to the higher wheel sinkage. Therefore, a bigger contact surface area not only decrease the contact pressure but may be favorable to increase the load bearing capacity of the same soil at moderate sinkage.

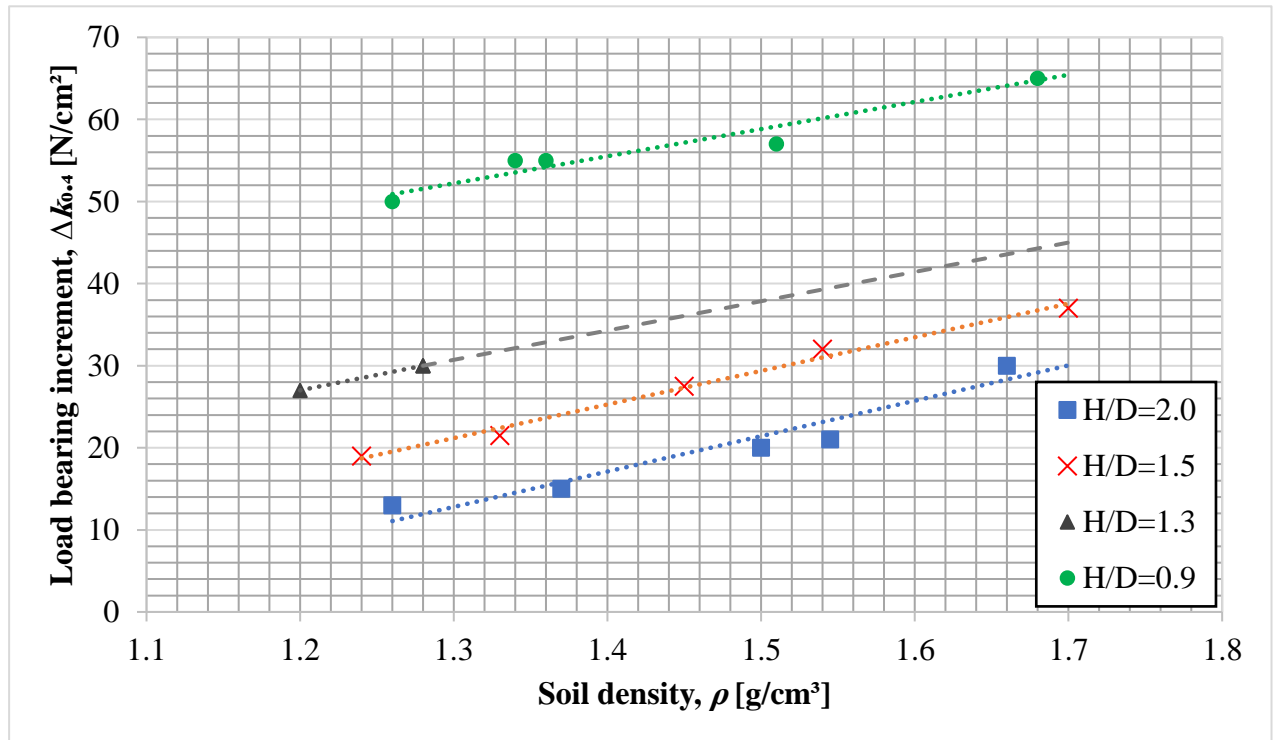


Fig. 4.30. Effect of soil density on the load bearing increment in the unconfined compaction range for different relative soil density

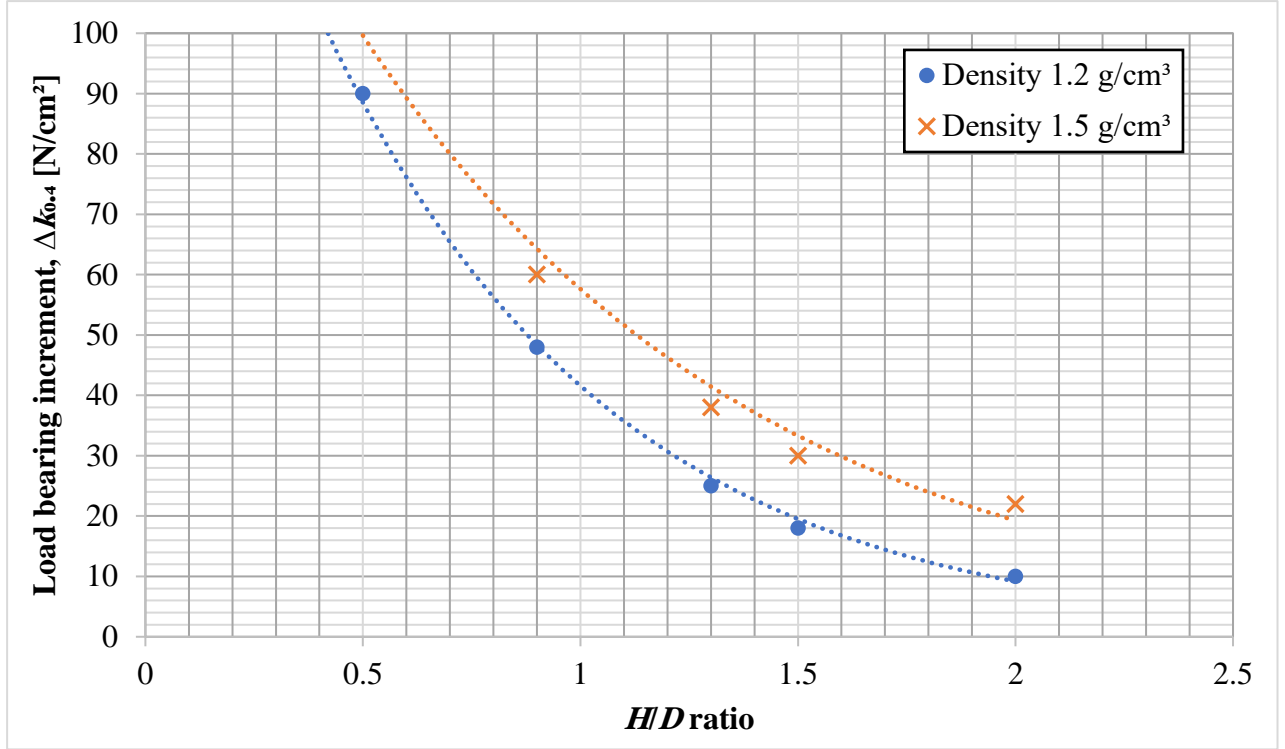


Fig. 4.31. Effect of relative soil thickness on the load bearing increment in the unconfined compaction range

4.10. Behaviour of soil in shallow layer

In shallow homogenous upper layer, $H/D \leq 0.5$ the soil under loading surface behaves like closed space compaction. The side motion of soil is prevented and in the most space under the plate the vertical motion take over. As Yegorov's theory suggests in shallow layer the pressure (stress) is almost equalized and the whole layer will be compacted.

Experimental results of closed space (confined test) are shown in Fig. 4.32 where different soil density used with plate diameter (20 cm) and soil thickness of 10 cm. As can be seen in Fig. 4.32 the pressure-sinkage curve exhibited the same behaviour, moreover after small pre-compaction depending on the initial density the curves ascended very steeply. As a result, the cone shaped compact zone cannot be developed in its classical form and there is no constant load bearing capacity factor k only the varying part exists.

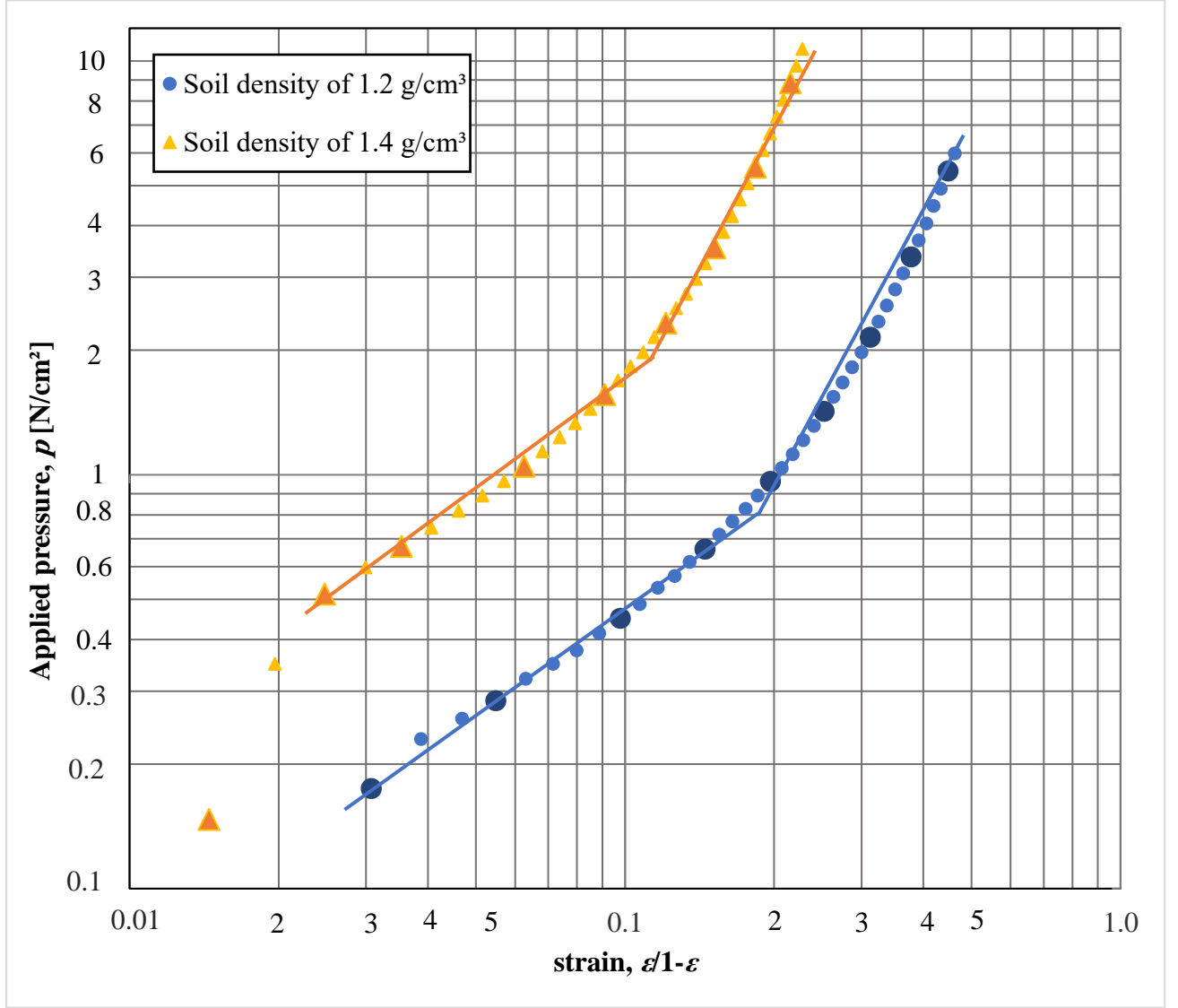


Fig. 4.32. Compaction of sandy loam soil with two different soil densities of 1.2 and 1.4 g/cm³

For compression, the compaction of closed space (confined test) and plate sinkage test in soil bin is shown in Fig. 4.33. Despite the stress-strain curves of the bevameter and confined tests are slightly diverged, but the soil behaviour seems similar. Moreover, there is no cone shape compact zone under the plate with the bevameter test, as the pressure and the load bearing capacity modulus are increasing steeply.

The calculated compaction equations are:

under the plate unconfined compaction

$$p = 36.5 \left(\frac{\epsilon}{1-\epsilon} \right)^{2.1}, \quad (4.18)$$

for closed space compaction

$$p = 34.5 \left(\frac{\epsilon}{1-\epsilon} \right)^{2.2}. \quad (4.19)$$

For higher compaction the exponents slightly increase.

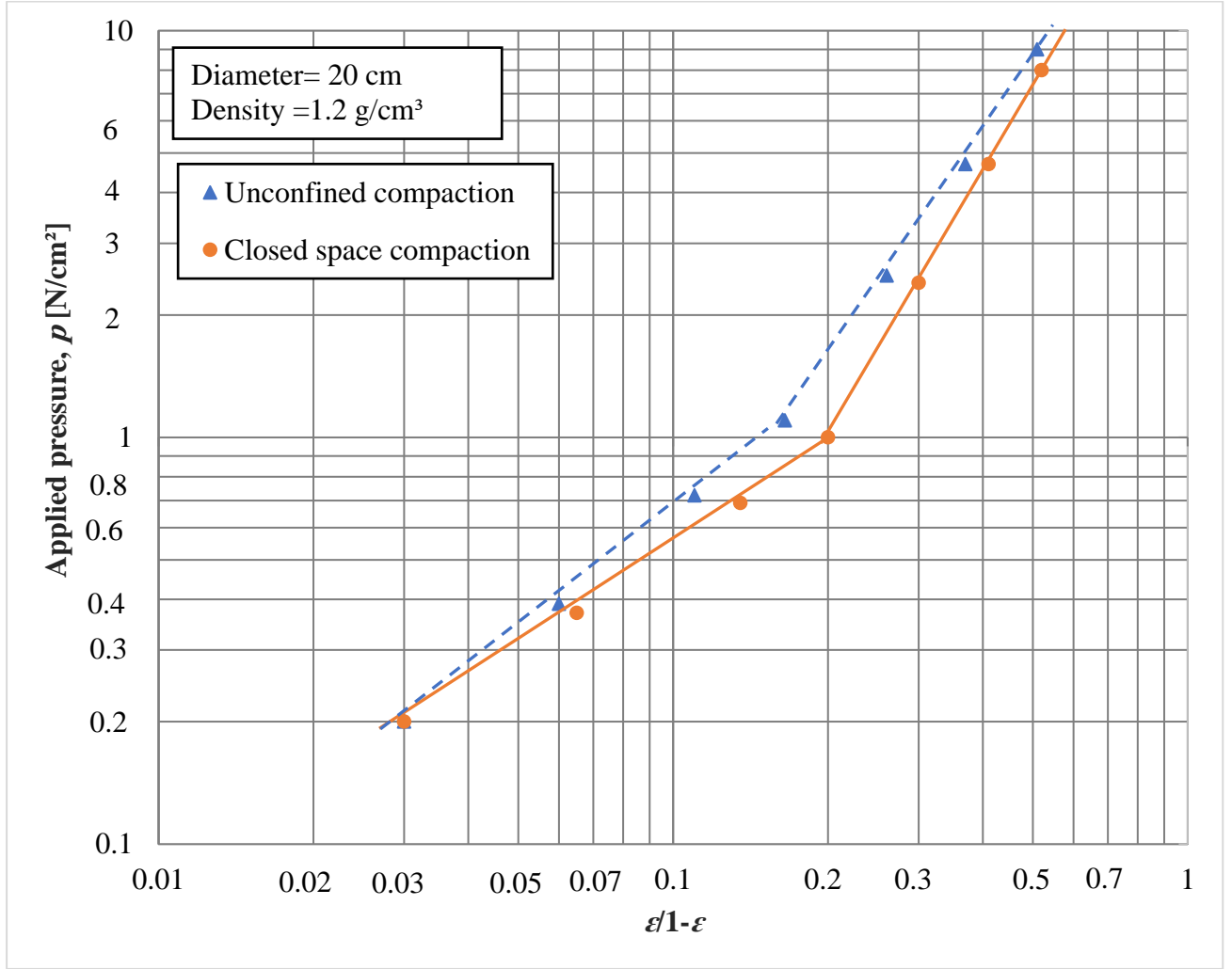


Fig. 4.33. Comparison of unconfined compaction in shallow layer and in closed space

An interesting soil behaviour is shown at $H/D=0.9$. In principle, at $H/D=1$ or below there is no constant load bearing capacity factor (k) exists, but a continuous soil compaction take place. Several measurements with soil thickness of 18 cm and plate diameter of 20 cm show that there is short soil consolidation under the plate with some side flow resulting in common parabolic pressure rise with constant k value up to $z/D=0.18$. After that (inflection point) the pressure curve steeply increasing and the conical compact zone is developed under the plate with hindered side motion of the soil.

It is noted that similar consolidation is not seen at $H/D=0.5$, probably due to the very small soil side flow and the governing vertical deformation.

4.11. New scientific results

This section presents the new scientific findings from the research as follows:

1. Transition zone of infinite to finite thickness

There are typically two deformation zones under loading, the build-up zone (infinite thickness) that has an increasing resistance and the compact zone (finite thickness). In addition, there is transition zone between them which reflect the effect of the rigid layer on the compaction. I

introduced a relation to specify the transition zone by considering the relative sinkage (z/D) and relative depth (H/D). This transition mentioned as breaking points (z_o/D)

$$\frac{z_o}{D} - \frac{H}{D} = 1,$$

where the constant slightly depends on the internal friction angle of soil.

2. Interaction zone with rigid layer

A resting compact zone of cone shape develops under the loading surface (plate or tyre) which, nearing the rigid layer, counter acts with the rigid layer increasing the vertical pressure and load bearing factor (k) in an exponential mode. Due to this interaction, I introduced an apparent load bearing factor (k_{app}) consisting of two parts: one (k) is the common and constant load bearing capacity factor valid under the critical depth z_o/D , and the second one is $B \left(e^{c \left(\frac{z}{D} - \frac{z_o}{D} \right)} - 1 \right)$ which increases with the deformation due to the interaction of compact zone with the rigid layer.

$$p = k_{app} \left(\frac{z}{D} \right)^n,$$

$$k_{app} = k + B \left(e^{c \left(\frac{z}{D} - \frac{z_o}{D} \right)} - 1 \right).$$

3. Generalizing the pressure-sinkage equation

A change in soil depth (H) modifies the strain ($\varepsilon=z/H$) as well as the compaction for the same deformation (z). I derived two dimensionless numbers by employing an approximate similarity. These dimensionless numbers are $\left(\frac{k}{\Delta\gamma \cdot D} \right)$ which represents the infinite thickness and (H/D) which represents the finite thickness. Also, I derived and determined a dimensionless load bearing number by multiplying the dimensionless numbers aforementioned to combine the effect of the infinite and finite half-space which is invariant for a given soil.

$$\frac{k \cdot H}{\Delta\gamma \cdot D^2} = 1150.$$

Using this dimensionless number, I introduced the generalized pressure-sinkage equation taking into account the effect of soil density, loading surface diameter, and the soil depth H .

$$\frac{p}{\Delta\gamma \cdot D} = 1150 \frac{D}{H} \left(\frac{z}{D} \right)^n.$$

4. Shallow homogenous layer

Through the experimental results, I have proven in the case of shallow homogenous upper layer where $H/D \leq 0.5$, after a short pre-compaction, the pressure and load bearing are steeply increasing almost similarly to a closed space compaction process. In the whole space the pressure is almost the same without definite cone shaped zone.

5. CONCLUSIONS AND RECOMMENDATIONS

In conclusion, theoretical and experimental analysis has been conducted to study the load bearing capacity of sandy loam soil as a homogenous finite half-space. The load bearing capacity represented by the pressure-sinkage relationship. The bevameter apparatus has been designed and constructed to examine the load bearing capacity and soil properties via applied normal load on soil surface. The experiments were conducted using three different diameters of circular sinkage plates with different soil thicknesses and different soil densities. The applied force, time and plate displacement inside the soil which are recorded by the strain gauge have been examined indoor. These experimental data employed to determine the applied pressure (p) and the relative sinkage (z/D). The pressure–sinkage curves of in situ soil measurement plotted by using logarithmic scale. All the curves showed there are two deformation zones, the first one is the build-up zone where the load bearing capacity factor (k) is constant, the conventional pressure-sinkage relationship can be applied for determining the soil properties k and n , the soil under the plate behaves similarly to when it is in the infinite thickness. The other zone is the interaction zone with the rigid layer where the soil behaves more exponentially and the load bearing capacity is varied. A relationship proposed to define the transition zone between the deformation zones which represented by breaking point as critical relative sinkage (z_o/D). Here, the compaction, as well as the deformation, increases rapidly. The conventional pressure-sinkage relationship modified by suggesting new load bearing capacity factor (k_{app}) to convey this part. The pressure-sinkage curve plotted with the k_{app} for different soil thickness, divers of plate sinkage plate and various densities. The values of k_{app} and the applied pressure are converging. Therefore, as the pressure increased, the sinkage modulus k_{app} also increased, which means the load bearing capacity of soil increasing as well. The effect of finite depth (H) on the load bearing capacity factor (k) have been studied, the results showed that the load bearing capacity factor dependent on soil density where it increased with increasing the soil density. The behaviour of the finite half-space and the changing hardness of soil within the finite thickness present the greatest difficulties for generalizing the experimental results. By using similarity number, a dimensionless number (Π) proposed to cover the relation of soils and finite half-space. The new generalized pressure-sinkage relationship suggested by employing the dimensionless number in the conventional pressure-sinkage relationship. The new relation represents the generalized pressure-sinkage equation in dimensionless form considering the effect of soil density and the finite depth. The behaviour of shallow homogenous upper layer, $H/D \leq 0.5$, discussed and the result showed the soil under loading surface behaves like closed space compaction. The side motion of soil is prevented and in the most space under the plate the vertical motion take over. Therefore, the cone shaped compact zone cannot be developed in its classical form and there is no constant load bearing capacity factor k only the varying part exists.

As a recommendation, further experimental work should be conducted with inhomogeneous soil in the laboratory then in the field to validate the proposed new relations of load bearing capacity factor and the generalized pressure-sinkage relationship. Moreover, further work on other soil type should be carried out.

6. SUMMARY

LOAD BEARING CAPACITY OF SOIL AS A HOMOGENEOUS FINITE HALF-SPACE

The first section of this study dealt with the comprehensive analysis of load bearing capacity determination and lighted the gap in knowledge in the effect of the loading surface diameter on the load bearing capacity as a function of thickness of the finite half-space. the next chapter describe the materials and processes used in the research for the experimental measurements, like designing and constructing a bevameter (plate sinkage test) for testing the soil behaviour under loading using wide ranging of soil properties and soil thickness. Thereafter, a theoretical part which includes prediction of soil sinkage and soil behaviours in the finite half-space by employing some results from literature and some theories like Yegorov theory. Consequently, theoretical equations have been suggested for homogeneous finite half-space to cover the soil behaviour of finite half-space. The mechanical properties of the soil which are shown in the results section have been determined by employing the direct shear test. The results of the plate sinkage test can be classified into:

1. The deformation zones and the interaction of the compact zone with the action of a rigid layer have been explained by employing different sinkage plate diameter, various soil thickness and divers soil densities.
2. A new sinkage modulus(k_{app}) concerning the affection of the soil's hard layer have been proposed according to the experimental results,
3. The experimental results of load bearing capacity factor (k) with the soil density (ρ) showed that there is acceptable accuracy between the theoretical and experimental estimate.
4. Generalizing the pressure-sinkage equation have been discussed by comparing the experimental results of pressure number ($p/\Delta\gamma \cdot D$) and the relative sinkage (z/D) with the proposed model. The results show that there is reasonable converging between the theoretical and experimental estimate.
5. Regarding the shallow homogenous upper layer where $H/D \leq 0.5$, the results showed that the soil under loading surface behaves like closed space compaction. The side motion of soil is prevented and in the most space under the plate the vertical motion take over.

As a recommendation, more experimental work should be conducted with inhomogeneous soil in the laboratory then in the field to validate the proposed new relations of load bearing capacity factor and the generalized pressure-sinkage relationship. Moreover, further work on other soil type should be carried out.

A further interesting and examined question is the actual deformation zone developing under a loading surface during its downward motion causing a continuously increasing loading force.

7. ÖSSZEFOGLALÁS (SUMMARY IN HUNGARIAN)

A TALAJ TEHERBÍRÓKÉPESSÉGÉNEK ALAKULÁSA VÉGESFÉLTÉR ESETÉN

A disszertáció első része a teherbíróképesség meghatározásának átfogó elemzésével foglalkozik és rávilágít arra az ismerethiányra, hogy a terhelőfelület átmérőjének a teherbíróképességre gyakorolt hatását a véges féltér vastagságának (H) függvényében nem vizsgálták. A következő fejezetben a kutatás során a kísérleti mérésekhez felhasznált anyagok és eljárások kerültek ismertetésre, mint pl. egy bevameter (nyomólap süllyedéssel vizsgáló készülék) tervezése és kivitelezése. A talaj teherbíróképességének vizsgálata során a talajparaméterek és az alkalmazott talajvastagságok széles skáláját alkalmaztam. Ezt követi egy elméleti következtetések fejezet, amely magában foglalja a talaj besüllyedésének és a talaj viselkedésének leírását végesféltér esetén. A talaj viselkedésének ilyen körülmények közötti leírása szakirodalmi adatokra támaszkodik, mint például Egorov-elmélete.

Végül elméleti összefüggéseket javasoltam a talaj homogén végesféltérben történő nyomólap süllyedéssel vizsgálata esetén mutatott talajviselkedés leírására. A talaj mechanikai tulajdonságait az eredmények részben mutatom be, melyeket talajnyírási vizsgálattal határoztam meg. A nyomólap süllyedéssel vizsgálat főbb eredményei a következők:

1. A deformációs és a tömör zóna kölcsönhatását a keménysréteg, eltérő nyomólap átmérők, talajvastagságok és a talajsűrűség befolyásolják.
2. A kísérleti eredmények alapján új teherbírási tényezőt (k_{app}) javasoltam a talajban lévő keménysréteg meghatározására vonatkozóan.
3. A teherbírási tényezővel (k) és a talajsűrűséggel (ρ) végzett kísérleti eredmények azt mutatták, hogy az elméleti megfontolások és a kísérleti eredmények között elfogadható korreláció van.
4. Az általános nyomás-besüllyedés egyenletet a nyomásszám ($p/(\Delta\gamma \cdot D)$) és a relatív besüllyedés (z/D) felhasználásával hoztam létre. Az eredmények azt mutatják, hogy az elmélet és a kísérlet között szoros összefüggés van.
5. A vékony homogén felső rétegre vonatkozóan, amikor $H/D \leq 0.5$, az eredmények azt mutatták, hogy a terhelőfelület alatti talaj a zárt térben történő tömörítésnek megfelelően viselkedik. A talaj oldalirányú mozgása gátolt, így a lemez alatt a legtöbb helyen a talajszemcsék csak függőleges mozgást végeznek.

Az általam javasolt általánosított nyomás-besüllyedés összefüggés validálására több laboratóriumi kísérletet, mint terepi vizsgálatot javaslok. Ezenkívül ki kell terjeszteni a vizsgálatokat más talajtípusokra is. A következő érdekes vizsgálódási irány a terhelőfelület alatt kialakuló tényleges deformációs zóna mozgásának vizsgálata, amely egy folyamatosan növekvő terhelőerőt hoz létre a nyomófejen.

8. APPENDICES

A1: Bibliography

1. Afzalnia, S., and Zabihi, J. (2014): Soil compaction variation during corn growing season under conservation tillage, *Soil and Tillage Research*, 137, 1–6.
<https://doi.org/10.1016/j.still.2013.11.003>
2. Ageikin, J. S. (1987a): *Off-The-Road Mobility of Automobiles*. Amerind Pub. Co., New Delhi
3. Ageikin, J. S. (1987b): *Off-the-road Wheeled and Combined Traction Devices: Theory and Calculation*. Amerind Pub. Co., New Delhi
4. Alakukku, L., Weisskopf, P., Chamen, W. C. ., Tijink, F. G. ., van der Linden, J. ., Pires, S., Sommer, C., and Spoor, G. (2003): Prevention strategies for field traffic-induced subsoil compaction: a review, *Soil and Tillage Research*, 73(1–2), 145–160.
[https://doi.org/10.1016/S0167-1987\(03\)00107-7](https://doi.org/10.1016/S0167-1987(03)00107-7)
5. Alaoui, A., and Diserens, E. (2018): Mapping soil compaction – A review, *Current Opinion in Environmental Science & Health*, 5, 60–66. <https://doi.org/10.1016/j.coesh.2018.05.003>
6. Alexandrous, A., and Earl, R. (1995): In situ determination of the precompaction stress of a soil, *Journal of Agricultural and Engineering Research*, (61), 67–72.
<https://doi.org/10.1006/jaer.1995.1032>
7. Amuri, N., and Brye, K. R. (2008): Residue management practice effects on soil penetration resistance in a wheat-soybean double-crop production system, *Soil Science*, 173(11), 779–791. <https://doi.org/10.1097/SS.0b013e31818a54b4>
8. Apfelbeck, M., Wedler, A., Gibbesch, A., and Rebele, B. (2009): A novel terramechanics testbed setup for planetary rover wheel- soil interaction Testbed setup Pose tracking, in *International Society for Terrain-Vehicle Systems*. Bermen: ISTVS, 1–8
9. Arriaga, F. J., Lowery, B., and Raper, R. (2011): *Encyclopedia of Agrophysics*. Edited by J. Gliński, J. Horabik, and J. Lipiec. Dordrecht: Springer Netherlands (Encyclopedia of Earth Sciences Series). <https://doi.org/10.1007/978-90-481-3585-1>
10. Beckett, C. T. S., Bewsher, S., Guzzomi, A. L., Lehane, B. M., Fourie, A. B., and Riethmuller, G. (2018): Evaluation of the dynamic cone penetrometer to detect compaction in ripped soils, *Soil and Tillage Research*, 175, 150–157.
<https://doi.org/10.1016/j.still.2017.09.009>
11. Bekker, M. G. (1956): *Theory of Land Locomotion*. Ann Arbor, MI: University of Michigan Press. <https://doi.org/10.3998/mpub.9690401>
12. Bekker, M. G. (1960): *Off-the-road locomotion*. University of Michigan Press
13. Bekker, M. G. (1961): Evaluation and selection of optimum vehicle types under random terrain conditions, in *Proceedings of the 1st ISTVS International Conference*,. Turin: ISTVS
14. Bekker, M. G. (1969): *Introduction to terrain-vehicle systems*. University of Michigan Press; First Edition edition (March 1, 1969)
15. Bernstein, R. (1913): Probleme zur experimentellen Motorpflugmechanik, *Der Motorwagen*, 16(9), 199–206
16. Blanco-Canqui, H., and Ruis, S. J. (2018): No-tillage and soil physical environment, *Geoderma*, 326, 164–200. <https://doi.org/10.1016/j.geoderma.2018.03.011>
17. Brus, D. J., and van den Akker, J. J. H. (2018): How serious a problem is subsoil compaction in the Netherlands? A survey based on probability sampling, *SOIL*, 4(1), 37–45. <https://doi.org/10.5194/soil-4-37-2018>

18. Campbell, D. M. H., White, B., and Arp, P. A. (2013): Modeling and mapping soil resistance to penetration and rutting using LiDAR-derived digital elevation data, *Journal of Soil and Water Conservation*, 68(6), 460–473. <https://doi.org/10.2489/jswc.68.6.460>
19. Castioni, G. A. F., de Lima, R. P., Cherubin, M. R., Bordonal, R. O., Rolim, M. M., and Carvalho, J. L. N. (2021): Machinery traffic in sugarcane straw removal operation: Stress transmitted and soil compaction, *Soil and Tillage Research*, 213, 105122. <https://doi.org/10.1016/j.still.2021.105122>
20. Cerato, A. B., and Lutenecker, A. J. (2006): Bearing Capacity of Square and Circular Footings on a Finite Layer of Granular Soil Underlain by a Rigid Base, *Journal of Geotechnical and Geoenvironmental Engineering*, 132(11), 1496–1501. [https://doi.org/10.1061/\(ASCE\)1090-0241\(2006\)132:11\(1496\)](https://doi.org/10.1061/(ASCE)1090-0241(2006)132:11(1496))
21. Chen, D., Hou, L., Bu, X., and Chen, Y. (2020): A piecewise bearing capacity method of unstructured terrain considering characteristics of soil mechanic and wheel geometry, *Journal of Terramechanics*, 89, 13–20. <https://doi.org/10.1016/j.jterra.2020.01.002>
22. Chung, S. O., Sudduth, K. A., Motavalli, P. P., and Kitchen, N. R. (2013): Relating mobile sensor soil strength to penetrometer cone index, *Soil and Tillage Research*, 129, 9–18. <https://doi.org/10.1016/j.still.2012.12.004>
23. Das, B. M. (2017): *Shallow Foundations*. Third edition. | Boca Raton : CRC Press, 2017.: CRC Press. <https://doi.org/10.1201/9781315163871>
24. Dewhurst, D. L. (1964): A load-sinkage equation for lunar soils, *AIAA Journal*, 2(4), 761–762. <https://doi.org/10.2514/3.2421>
25. Ding, L., Gao, H., Deng, Z., Li, Y., and Liu, G. (2014): New perspective on characterizing pressure–sinkage relationship of terrains for estimating interaction mechanics, *Journal of Terramechanics*, 52, 57–76. <https://doi.org/10.1016/j.jterra.2014.03.001>
26. Duttman, R., Schwanebeck, M., Nolde, M., and Horn, R. (2014): Predicting Soil Compaction Risks Related to Field Traffic during Silage Maize Harvest, *Soil Science Society of America Journal*, 78(2), 408–421. <https://doi.org/10.2136/sssaj2013.05.0198>
27. Earl, R. (1996): Prediction of Trafficability and Workability using Tensiometers, *Journal of Agricultural Engineering Research*, 63(1), 27–33. <https://doi.org/10.1006/jaer.1996.0004>
28. Earl, R. (1997): Assessment of the Behaviour of Field Soils during Compression, *Journal of Agricultural Engineering Research*, 68(2), 147–157. <https://doi.org/10.1006/jaer.1997.0192>
29. Edwards, M. B., Dewoolkar, M. M., Huston, D. R., and Creager, C. (2017): Bevameter testing on simulant Fillite for planetary rover mobility applications, *Journal of Terramechanics*, 70, 13–26. <https://doi.org/10.1016/j.jterra.2016.10.004>
30. Emori, R., and Schuring, D. (1966): Static and dynamic penetration tests of soil, *Journal of Terramechanics*, 3(1), 23–30
31. Eslami, A., Moshfeghi, S., MolaAbasi, H., and Eslami, M. M. (2020): Background to foundation engineering, in *Piezocone and Cone Penetration Test (CPTu and CPT) Applications in Foundation Engineering*. Elsevier, 25–53. <https://doi.org/10.1016/B978-0-08-102766-0.00002-X>
32. Evans, I. (1953): The sinkage of tracked vehicles on soft ground, *British Journal of Applied Physics*, 4(11), 330–334. <https://doi.org/10.1088/0508-3443/4/11/303>
33. Gao, W., Ren, T., Bengough, A. G., Auneau, L., Watts, C. W., and Whalley, W. R. (2012): Predicting Penetrometer Resistance from the Compression Characteristic of Soil, *Soil Science Society of America Journal*, 76(2), 361–369. <https://doi.org/10.2136/sssaj2011.0217>

34. Gao, Y. (2016): *Contemporary Planetary Robotics*. Germany: Wiley- VCH
35. Goodin, C., and Priddy, J. D. (2016): Comparison of SPH simulations and cone index tests for cohesive soils, *Journal of Terramechanics*, 66, 49–57.
<https://doi.org/10.1016/j.jterra.2015.09.002>
36. Gotteland, P., and Benoit, O. (2002): Experimental device to study trafficability: penetration tests and useful parameters, in *Proceedings of the 14th international conference of the ISTVS*. Vicksburg, USA.
37. Gotteland, P., and Benoit, O. (2006): Sinkage tests for mobility study , modelling and experimental validation, *Journal of Terramechanics*, 43, 451–467.
<https://doi.org/10.1016/j.jterra.2005.05.003>
38. Grahn, M. (1991): Prediction of sinkage and rolling resistance for off-the-road vehicles considering penetration velocity, *Journal of Terramechanics*, 28(4), 339–347.
[https://doi.org/10.1016/0022-4898\(91\)90015-X](https://doi.org/10.1016/0022-4898(91)90015-X)
39. Gürsoy, S. (2021): Soil Compaction Due to Increased Machinery Intensity in Agricultural Production: Its Main Causes, Effects and Management, in *Technology in Agriculture*. IntechOpen. <https://doi.org/10.5772/intechopen.98564>
40. Gysi, M. (1999): Influence of single passes with high wheel load on a structured, unploughed sandy loam soil, *Soil and Tillage Research*, 52(3–4), 141–151.
[https://doi.org/10.1016/S0167-1987\(99\)00066-5](https://doi.org/10.1016/S0167-1987(99)00066-5)
41. Hamada, K., Inoue, H., Mochizuki, H., Miyamoto, T., Asakura, M., and Shimizu, Y. (2021): Effect of hardpan on the vertical distribution of water stress in a converted paddy field, *Soil and Tillage Research*, 214, 105161. <https://doi.org/10.1016/j.still.2021.105161>
42. Hamza, M. A., and Anderson, W. K. (2005): Soil compaction in cropping systems, *Soil and Tillage Research*, 82(2), 121–145. <https://doi.org/10.1016/j.still.2004.08.009>
43. He, R., Sandu, C., Khan, A. K., Guthrie, A. G., Schalk Els, P., and Hamersma, H. A. (2019): Review of terramechanics models and their applicability to real-time applications, *Journal of Terramechanics*, 81, 3–22. <https://doi.org/10.1016/j.jterra.2018.04.003>
44. Head, K. H., and Epps, R. J. (2011): *Manual of Soil Laboratory Testing: Volume 2: Permeability, Shear Strength and Compressibility tests*, Environmental & Engineering Geoscience. Published by Whittles Publishing, Dunbeath Mill, Dunbeath, Caithnes.
<https://doi.org/10.2113/gsegeosci.21.3.247>
45. Hegedus, E. (1965): Plate sinkage study by means of dimensional analysis, *Journal of Terramechanics*, 2(2), 25–32. [https://doi.org/10.1016/0022-4898\(65\)90070-4](https://doi.org/10.1016/0022-4898(65)90070-4)
46. Hernanz, J. ., Peixoto, H., Cerisola, C., and Sánchez-Girón, V. (2000): An empirical model to predict soil bulk density profiles in field conditions using penetration resistance, moisture content and soil depth, *Journal of Terramechanics*, 37(4), 167–184.
[https://doi.org/10.1016/S0022-4898\(99\)00020-8](https://doi.org/10.1016/S0022-4898(99)00020-8)
47. Herrick, J. E., and Jones, T. L. (2002): A dynamic cone penetrometer for measuring soil penetration resistance, *Soil Science Society of America Journal*, 66(4), 1320–1324.
<https://doi.org/10.2136/sssaj2002.1320>
48. Hong, W.-T., Yu, J.-D., Kim, S. Y., and Lee, J.-S. (2019): Dynamic Cone Penetrometer Incorporated with Time Domain Reflectometry (TDR) Sensors for the Evaluation of Water Contents in Sandy Soils, *Sensors*, 19(18), 3841. <https://doi.org/10.3390/s19183841>
49. Horiko, S., and Ishigami, G. (2020): Experimental study on wheel-soil interaction mechanics using in-wheel sensor and particle image velocimetry part II. Analysis and modeling of shear stress of lightweight wheeled vehicle, *Journal of Terramechanics*, 91, 243–256. <https://doi.org/10.1016/j.jterra.2020.07.002>

50. Horn, R., and Fleige, H. (2003): A method for assessing the impact of load on mechanical stability and on physical properties of soils, *Soil and Tillage Research*, 73(1–2), 89–99. [https://doi.org/10.1016/S0167-1987\(03\)00102-8](https://doi.org/10.1016/S0167-1987(03)00102-8)
51. Horn, R., and Peth, S. (2011): *Mechanics of Unsaturated Soils for Agricultural Applications*, in Pan Ming, H., Yuncong, L., and Malcolm E., S. (eds) *Handbook of Soil Sciences Properties and Processes*. Routledge Handbooks Online. <https://doi.org/10.1201/b11267-4>
52. Inns, F. M., and Kilgour, J. (1978): *Agricultural tyres*. London : Dunlop. Available at: http://books.google.co.uk/books/about/Agricultural_tyres.html?id=JB8NAQAAMAAJ&pgis=1
53. Jabro, J. D., Iversen, W. M., Evans, R. G., Allen, B. L., and Stevens, W. B. (2014): Repeated Freeze-Thaw Cycle Effects on Soil Compaction in a Clay Loam in Northeastern Montana, *Soil Science Society of America Journal*, 78(3), 737–744. <https://doi.org/10.2136/sssaj2013.07.0280>
54. Jabro, J. D., Iversen, W. M., Stevens, W. B., Evans, R. G., Mikha, M. M., and Allen, B. L. (2015): Effect of Three Tillage Depths on Sugarbeet Response and Soil Penetrability Resistance, *Agronomy Journal*, 107(4), 1481–1488. <https://doi.org/10.2134/agronj14.0561>
55. Jabro, J. D., Iversen, W. M., Stevens, W. B., Evans, R. G., Mikha, M. M., and Allen, B. L. (2016): Physical and hydraulic properties of a sandy loam soil under zero, shallow and deep tillage practices, *Soil and Tillage Research*, 159, 67–72. <https://doi.org/10.1016/j.still.2016.02.002>
56. Jang, G., Lee, S., and Lee, K. (2016): Discrete element method for the characterization of soil properties in, *Journal of Mechanical Science and Technology*, 30(6), 2743–2751. <https://doi.org/10.1007/s12206-016-0536-4>
57. Janosi, Z. (1961): An analysis of pneumatic tyre performance on deformable soil. *Proceedings of the 1st International Conference on the Mechanics of Soil-Vehicle Systems.*, in *Proceedings of the 1st International Conference on the Mechanics of Soil-Vehicle Systems*. Troino, Italy.
58. Kacigin, V. V., and Guskovt, V. V (1968): The basis of tractor performance theory, *Journal of Terramechanics*, 5(3), 43–66
59. Kaliakin, V. N. (2017): Example Problems Related to Shear Strength of Soils, in *Soil Mechanics*. Elsevier, 419–439. <https://doi.org/10.1016/B978-0-12-804491-9.00010-0>
60. Keller, T., and Arvidsson, J. (2016): A model for prediction of vertical stress distribution near the soil surface below rubber-tracked undercarriage systems fitted on agricultural vehicles, *Soil and Tillage Research*, 155, 116–123. <https://doi.org/10.1016/j.still.2015.07.014>
61. Keller, T., Berli, M., Ruiz, S., Lamandé, M., Arvidsson, J., Schjønnig, P., and Selvadurai, A. P. S. (2014): Transmission of vertical soil stress under agricultural tyres: Comparing measurements with simulations, *Soil and Tillage Research*, 140, 106–117. <https://doi.org/10.1016/j.still.2014.03.001>
62. Keller, T., Lamand, M., Peth, S., Berli, M., Delenne, J.-Y., Baumgarten, W., Rabbel, W., Radja, F., Rajchenbach, J., Selvadurai, A. P. S., and Or, D. (2013): An interdisciplinary approach towards improved understanding of soil deformation during compaction, *Soil and Tillage Research*, 128, 61–80. <https://doi.org/10.1016/j.still.2012.10.004>
63. Keller, T., Lamandé, M., Naderi-Boldaji, M., and de Lima, R. P. (2022): Soil Compaction Due to Agricultural Field Traffic: An Overview of Current Knowledge and Techniques for Compaction Quantification and Mapping, in. Springer, Cham, 287–312. https://doi.org/10.1007/978-3-030-85682-3_13

64. Keller, T., Lamandé, M., Schjønning, P., and Dexter, A. R. (2011): Analysis of soil compression curves from uniaxial confined compression tests, *Geoderma*, 163(1–2), 13–23. <https://doi.org/10.1016/j.geoderma.2011.02.006>
65. Kim, J.-T., Im, D., Park, J.-H., Choi, H.-J., Oh, J.-W., Cho, S.-J., and Park, Y.-J. (2022): Experimental analysis of mechanical properties of coastal terrain via bevameter tests, *Journal of Terramechanics*, 100, 39–50. <https://doi.org/10.1016/j.jterra.2021.12.001>
66. Kim, Y.-S., Kim, T.-J., Kim, Y.-J., Lee, S.-D., Park, S.-U., and Kim, W.-S. (2020): Development of a Real-Time Tillage Depth Measurement System for Agricultural Tractors: Application to the Effect Analysis of Tillage Depth on Draft Force during Plow Tillage, *Sensors*, 20(3), 912. <https://doi.org/10.3390/s20030912>
67. Kiss, P. (2003): Rolling Radii of a Pneumatic Tyre on Deformable Soil, *Biosystems Engineering*, 85(2), 153–161. [https://doi.org/10.1016/S1537-5110\(03\)00043-6](https://doi.org/10.1016/S1537-5110(03)00043-6)
68. Kogelbauer, I., Heine, E., D’Amboise, C., Müllebnner, C., Sokol, W., and Loiskandl, W. (2013): Adaptation of Soil Physical Measurement Techniques for the Delineation of Mud and Lakebed Sediments at Neusiedler See, *Sensors*, 13(12), 17067–17083. <https://doi.org/10.3390/s131217067>
69. Kogure, K., Ohira, Y., and Yamaguchi, H. (1983): Prediction of sinkage and motion resistance of a tracked vehicle using plate penetration test, *Journal of Terramechanics*, 20(3–4), 121–128. [https://doi.org/10.1016/0022-4898\(83\)90043-5](https://doi.org/10.1016/0022-4898(83)90043-5)
70. Kulhawy, F. H., and Hirany, A. (2003): Foundations, in *Encyclopedia of Physical Science and Technology*. Elsevier, 145–166. <https://doi.org/10.1016/B0-12-227410-5/00874-7>
71. Laib, L. (2002): *Terepen mozgó járművek (Off-Road Vehicles)*. Budapest: Szaktudás Kiadó
72. Lamandé, M., and Schjønning, P. (2011): Transmission of vertical stress in a real soil profile. Part II: Effect of tyre size, inflation pressure and wheel load, *Soil and Tillage Research*, 114(2), 71–77. <https://doi.org/10.1016/j.still.2010.08.011>
73. Langhaar, H. L. (1951): *Dimensional Analysis and Theory of Models*. 1st Editio. John Wiley & Son Ltd
74. Li, B., and Yuan, H. (2019): Research on dynamic characteristics and reliability of a new heavy duty tractor, *Journal of Advanced Mechanical Design, Systems, and Manufacturing*, 13(1), JAMDSM0010–JAMDSM0010. <https://doi.org/10.1299/jamdsm.2019jamdsm0010>
75. Lim, Y., Le, V. D., and Bahati, P. A. (2021): Development of a New Pressure-Sinkage Model for Rover Wheel- Lunar Soil Interaction based on Dimensional Analysis and Bevameter Tests, *Journal of Astronomy and Space Sciences*, 38(4), 237–250. <https://doi.org/10.5140/JASS.2021.38.4.237>
76. de Lima, R. P., da Silva, A. P., Giarola, N. F. B., da Silva, A. R., and Rolim, M. M. (2017): Changes in soil compaction indicators in response to agricultural field traffic, *Biosystems Engineering*, 162, 1–10. <https://doi.org/10.1016/j.biosystemseng.2017.07.002>
77. Lin, J., Sun, Y., and Schulze Lammers, P. (2014): Evaluating model-based relationship of cone index, soil water content and bulk density using dual-sensor penetrometer data, *Soil and Tillage Research*, 138, 9–16. <https://doi.org/10.1016/j.still.2013.12.004>
78. Lyasko, M. (2010): LSA model for sinkage predictions, *Journal of Terramechanics*, 47(1), 1–19. <https://doi.org/10.1016/j.jterra.2009.06.004>
79. Mähönen, J., Lintzén, N., and Casselgren, J. (2021): Portable bevameter for measuring snow properties in field, *Cold Regions Science and Technology*, 182, 103195. <https://doi.org/10.1016/j.coldregions.2020.103195>
80. Mason, G. L., Salmon, J. E., McLeod, S., Jayakumar, P., Cole, M. P., and Smith, W. (2020): An overview of methods to convert cone index to bevameter parameters, *Journal of Terramechanics*, 87, 1–9. <https://doi.org/10.1016/j.jterra.2019.10.001>

81. Massah, J., and Noorolahi, S. (2010): Design, development and performance evaluation of a tractor-mounted bevameter, *Soil and Tillage Research*, 110(1), 161–166.
<https://doi.org/10.1016/j.still.2010.07.002>
82. Máthé, L. (2014): *Analysis of the motion of vehicles running onto terrain*. PhD dissertation, Szent Istvan University, Gödöllő, Hungary.
83. Máthé, L., and Kiss, P. (2015): Determination of rolling losses of a towed vehicle, in *Proceedings of the 13th ISTVS European Conference*. Rome
84. Máthé, L., Kiss, P., Laib, L., and Pillinger, G. (2013): Computation of run-off-road vehicle speed from terrain tracks in forensic investigations, *Journal of Terramechanics*, 50(1), 17–27. <https://doi.org/10.1016/j.jterra.2012.08.002>
85. Medvedev, V. V., and Cybulko, W. G. (1995): Soil criteria for assessing the maximum permissible ground pressure of agricultural vehicles on Chernozem soils, *Soil and Tillage Research*, 36(3–4), 153–164. [https://doi.org/10.1016/0167-1987\(95\)00501-3](https://doi.org/10.1016/0167-1987(95)00501-3)
86. Meirion-Griffith, G., and Spenko, M. (2011): A modified pressure-sinkage model for small, rigid wheels on deformable terrains, *Journal of Terramechanics*, 48(2), 149–155.
<https://doi.org/10.1016/j.jterra.2011.01.001>
87. Meirion-Griffith, G., and Spenko, M. (2013): A pressure-sinkage model for small-diameter wheels on compactive, deformable terrain, *Journal of Terramechanics*, 50(1), 37–44.
<https://doi.org/10.1016/j.jterra.2012.05.003>
88. Moinfar, A., Shahgholi, G., Abbaspour-Gilandeh, Y., Herrera-Miranda, I., Hernández-Hernández, J. L., and Herrera-Miranda, M. A. (2021): Investigating the Effect of the Tractor Drive System Type on Soil Behavior under Tractor Tires, *Agronomy*, 11(4), 696.
<https://doi.org/10.3390/agronomy11040696>
89. Mouazen, A. M. (2002): Mechanical behaviour of the upper layers of a sandy loam soil under shear loading, *Journal of Terramechanics*, 39(3), 115–126.
[https://doi.org/10.1016/S0022-4898\(02\)00008-3](https://doi.org/10.1016/S0022-4898(02)00008-3)
90. Nawaz, M. F., Bourrié, G., and Trolard, F. (2013): Soil compaction impact and modelling. A review, *Agronomy for Sustainable Development*, 33(2), 291–309.
<https://doi.org/10.1007/s13593-011-0071-8>
91. Onafeko, O., and Reece, A. R. (1967): Soil stress and deformation beneath rigid wheels, *Journal of Terramechanics*, 59(1), 59–80
92. Oravec, H. A. (2009): *Understanding mechanical behavior of lunar soils for the study of vehicle mobility*. PhD dissertation, Case Western Reserve University, Cleveland, USA
93. Oyama, S. T. (2011): Chapter 1 - Correlations, in *Membrane Science and Technology*: Elsevier, 1–24. <https://doi.org/10.1016/B978-0-444-53728-7.00001-X>
94. Paradelo, R., and Barral, M. T. (2013): Influence of organic matter and texture on the compactability of Technosols, *CATENA*, 110, 95–99.
<https://doi.org/10.1016/j.catena.2013.05.012>
95. Peralta, G., Alvarez, C. R., and Taboada, M. Á. (2021): Soil compaction alleviation by deep non-inversion tillage and crop yield responses in no tilled soils of the Pampas region of Argentina. A meta-analysis, *Soil and Tillage Research*, 211, 105022.
<https://doi.org/10.1016/j.still.2021.105022>
96. Pillinger, G. (2016): *Deformation and damping of soil under tire*. PhD dissertation, Szent Istvan University, Gödöllő, Hungary.
97. Pillinger, G., Géczy, A., Hudoba, Z., and Kiss, P. (2018): Determination of soil density by cone index data, *Journal of Terramechanics*, 77, 69–74.
<https://doi.org/10.1016/j.jterra.2018.03.003>

98. Pope, R. G. (1969): The effect of sinkage rate on pressure sinkage relationships and rolling resistance in real and artificial clays, *Journal of Terramechanics*, 6(4), 31–38. [https://doi.org/10.1016/0022-4898\(69\)90015-9](https://doi.org/10.1016/0022-4898(69)90015-9)
99. Powrie, W. (2018): *Soil Mechanics*. 3rd Editio. London: CRC Press. <https://doi.org/10.1201/9781315275284>
100. Reece, A. R. (1965): Principles of soil-vehicle mechanics, *Proceedings of the Institution of Mechanical Engineers*, 180(1), 45–66. Available at: https://doi.org/10.1243/PIME_AUTO_1965_180_009_02
101. Ruzicka, M. C. (2008): On dimensionless numbers, *Chemical Engineering Research and Design*, 86(8), 835–868. <https://doi.org/10.1016/j.cherd.2008.03.007>
102. S. Gorucu, A. Khalilian, Y. J. Han, R. B. Dodd, and B. R. Smith (2006): An algorithm to determine the optimum tillage depth from soil penetrometer data in coastal plain soils, *Applied Engineering in Agriculture*, 22(5), 625–631. <https://doi.org/10.13031/2013.21993>
103. Sastre Jurado, C., Breul, P., Bacconnet, C., and Benz-Navarrete, M. (2020): Probabilistic 3D modelling of shallow soil spatial variability using dynamic cone penetrometer results and a geostatistical method, *Georisk: Assessment and Management of Risk for Engineered Systems and Geohazards*, 1–13. <https://doi.org/10.1080/17499518.2020.1728558>
104. Scott, C. R. (1994): *An Introduction to Soil Mechanics and Foundations*. Boston, MA: Springer US. <https://doi.org/10.1007/978-1-4899-7250-7>
105. Shah, A. N., Tanveer, M., Shahzad, B., Yang, G., Fahad, S., Ali, S., Bukhari, M. A., Tung, S. A., Hafeez, A., and Souliyanonh, B. (2017): Soil compaction effects on soil health and cropproductivity: an overview, *Environmental Science and Pollution Research*, 24(11), 10056–10067. <https://doi.org/10.1007/s11356-017-8421-y>
106. Sitkei, G. (1972): *A mezőgazdasági járószerkezetek méretezési módszerei*. Akadémiai Kiadó
107. Sitkei, G. (1986): *Mechanics of Agricultural Materials*. Elsevier Science
108. Sitkei, G. (1997): A Non-Linear Viscoelastic-Plastic Model for Describing Compaction Processes, *IFAC Proceedings Volumes*, 30(5), 105–112. [https://doi.org/10.1016/S1474-6670\(17\)44417-X](https://doi.org/10.1016/S1474-6670(17)44417-X)
109. Sitkei, G. (2015): Sinkage and rolling resistance of wheels, *Progress in Agricultural Engineering Sciences*, 11(1), 85–94. <https://doi.org/10.1556/446.11.2015.3>
110. Sitkei, G., Pillinger, G., Máthé, L., Gurmai, L., and Kiss, P. (2019): Methods for generalization of experimental results in terramechanics, *Journal of Terramechanics*, 81, 23–34. <https://doi.org/10.1016/j.jterra.2018.05.004>
111. Söhne, W. (1953): Fundamentals of pressure distribution and soil compaction under tractor tires, *Agricultural engineering*, 39
112. Taghavifar, H., and Mardani, A. (2017): *Off-road Vehicle Dynamics*. Switzerland: Springer International Publishing (Studies in Systems, Decision and Control). <https://doi.org/10.1007/978-3-319-42520-7>
113. Terzaghi, K. (1943): *Theoretical Soil Mechanics*. Hoboken, NJ, USA: John Wiley & Sons, Inc. <https://doi.org/10.1002/9780470172766>
114. Upadhyaya, S. K., Wulfsohn, D., and Mehlschau, J. (1993): An instrumented device to obtain traction related parameters, *Journal of Terramechanics*, 30(1), 1–20. [https://doi.org/10.1016/0022-4898\(93\)90027-U](https://doi.org/10.1016/0022-4898(93)90027-U)
115. Vaz, C. M. P., Manieri, J. M., de Maria, I. C., and Tuller, M. (2011): Modeling and correction of soil penetration resistance for varying soil water content, *Geoderma*, 166(1), 92–101. <https://doi.org/10.1016/j.geoderma.2011.07.016>

116. Wang, X., Fu, Z., Zhang, Q., and Huang, Y. (2021): Short-term subsoiling effects with different wing mounting heights before winter wheat on soil properties and wheat growth in Northwest China, *Soil and Tillage Research*, 213, 105151.
<https://doi.org/10.1016/j.still.2021.105151>
117. Whitlow, R. (1995): *Basic Soil Mechanics*. 3rd editio. England: Longman Group Limited
118. Wills, B. M. D. (1964): The design and development of a hydraulic bevameter, *Journal of Terramechanics*, 1(1), 91–97. [https://doi.org/10.1016/0022-4898\(64\)90125-9](https://doi.org/10.1016/0022-4898(64)90125-9)
119. Wong, J. Y. (2001): *Theory of Ground Vehicles*. Third. Canada: JOHN WILY and SONS
120. Wong, J. Y. (2010): *Terramechanics and Off-Road Vehicle Engineering*. Second. Oxford, UK: Elsevier Ltd. <https://doi.org/10.1016/C2009-0-00403-6>
121. Wong, J. Y., and Asnani, V. M. (2008): Study of the correlation between the performances of lunar vehicle wheels predicted by the Nepean wheeled vehicle performance model and test data, *Proceedings of the Institution of Mechanical Engineers, Part D: Journal of Automobile Engineering*, 222(11), 1755–1770.
<https://doi.org/10.1243/09544070JAUTO811>
122. Yang, C., Yang, G., Liu, Z., Chen, H., and Zhao, Y. (2018): A method for deducing pressure–sinkage of tracked vehicle in rough terrain considering moisture and sinkage speed, *Journal of Terramechanics*, 79, 99–113. <https://doi.org/10.1016/j.jterra.2018.09.001>
123. Yegorov, K. E. (1961): Deformation of a foundation bed of finite thickness, *Soil Mechanics [in Russian] Research Institute of Foundations, Moscow*, 43
124. Youssef, A.-F. A., and Ali, G. A. (1982): Determination of Soil Parameters using Plate Test, *Journal of Terramechanics*, 19(2), 129–147.
[https://doi.org/10.1016/0022-4898\(82\)90016-7](https://doi.org/10.1016/0022-4898(82)90016-7)
125. Yu, T. (2006): The Tractive Performance of a Friction-Based Prototype Track, *National Institute Economic Review*, 86(1), 1–43. <https://doi.org/10.1177/002795017808600103>
126. Zeleke, G., Owende, P. M. O., Kanali, C. L., and Ward, S. M. (2007): Predicting the pressure–sinkage characteristics of two forest sites in Ireland using in situ soil mechanical properties, *Biosystems Engineering*, 97(2), 267–281.
<https://doi.org/10.1016/j.biosystemseng.2007.03.007>

A2: Publications related to the dissertation

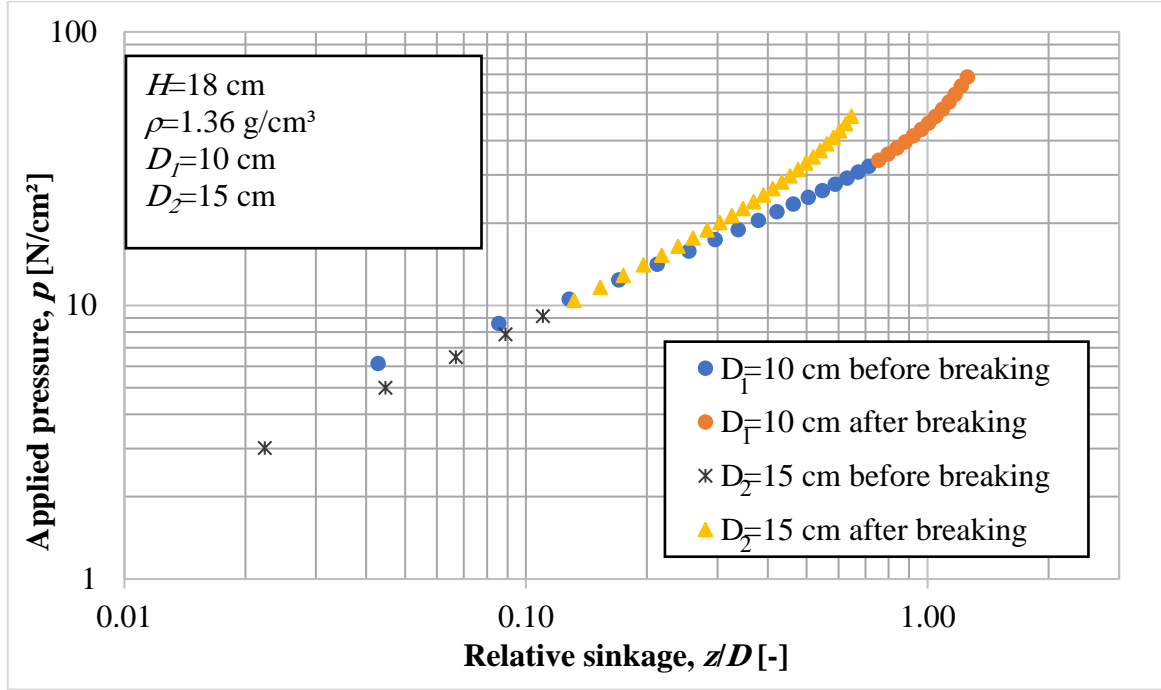
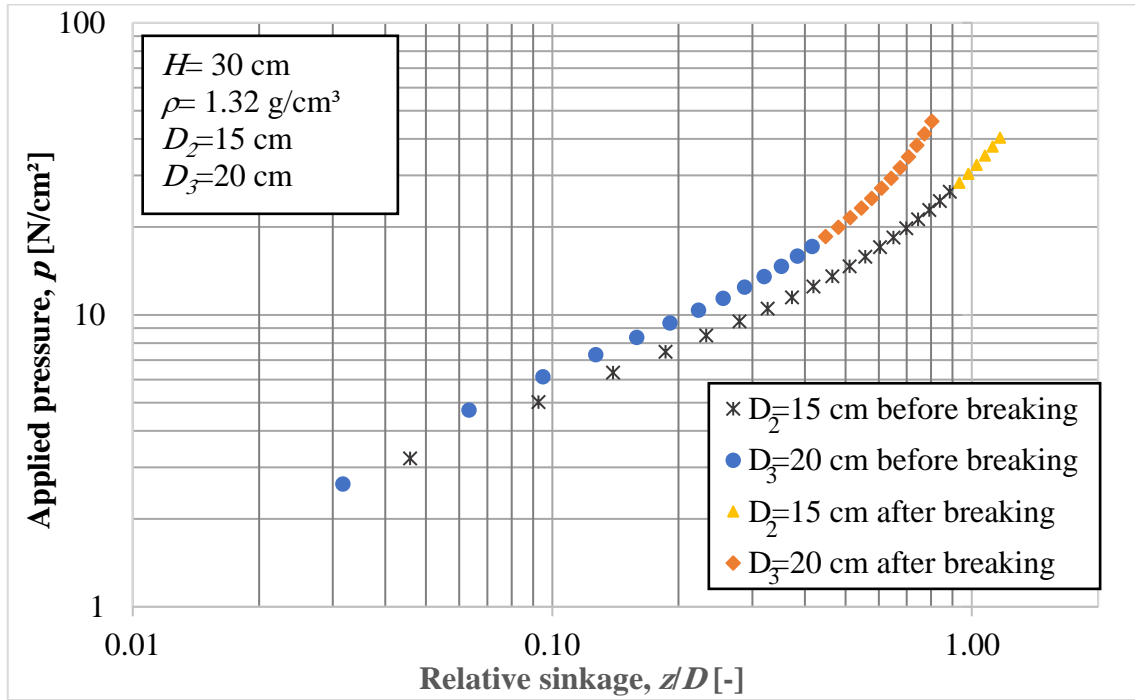
Refereed papers in foreign languages:

1. **Salman N. D.**, Kiss P. (2018): Survey: Effect of bulk density and moisture content of soil on the penetration resistance and penetration depth, *Mechanical Engineering Letters*, Vol. 17, pp. 109-118, HU ISSN 2060-3789.
2. **Salman N. D.**, Kiss P. (2019): A study of pressure sinkage relationship used in a tyre terrain interaction, *International Journal of Engineering and Management Sciences*, Vol. 4, No. 1, pp. 186-199, ISSN 2498-700X.
3. **Salman N. D.**, Pillinger G., Hanon M., Kiss P. (2020): Design and performance evaluation of bevameter equipment, *Journal of Advanced Mechanical Design, Systems, and Manufacturing*, Vol. 14, No. 6, pp. JAMDSM0084-JAMDSM0084, doi: 10.1299/jamdsm.2020jamdsm0084, ISSN 1881-3054 (IF: 0.609*).
4. **Salman N. D.**, Pillinger G., Kiss P. (2021): Soil behaviour under load in case of finite thickness, *International Review of Applied Sciences and Engineering*, Vol. 12, No. 1, pp. 29-33, doi: 10.1556/1848.2020.00091, ISSN 2062-0810.
5. **Salman N. D.**, Kiss P. (2021): Application of two techniques used for measuring the soil strength: A review, *Hungarian Agricultural Engineering*, No. 39, pp. 29-41, doi: 10.17676/HAE.2021.39.29, ISSN 2415-9751.
6. **Salman N. D.**, Pillinger G., Kiss P. (2021): Soil behavior of shallow homogenous upper layer soil, *Journal of Applied Science and Engineering (JASE)*, Vol. 25, No. 1, pp. 159 -164, doi: 10.6180/jase.202202_25(1).0016, ISSN 2708-9975.
7. **Salman N. D.**, Pillinger G., Hanon M., Kiss P. (2021): A modified pressure-sinkage model for studying the effect of a hard layer in sandy loam soil, *Applied Sciences*, MDPI, Vol. 11, No. 12, pp. 5499, doi:10.3390/app11125499, ISSN 2076-3417 (IF: 2.679*).
8. Keppler I., Bablena A., **Salman N. D.**, Kiss P. (2021): Discrete element model calibration based on in situ measurements, *Engineering Computations*, Emerald, Vol. ahead-of-print No. ahead-of-print. doi.org/10.1108/EC-05-2021-0288 (IF: 1.593*).

International conference abstracts:

9. **Salman N.**, Kiss P. (2018): A study of pressure sinkage relationship used in a tyre terrain interaction, *Book of extended abstracts*, 6th International Scientific Conference on Advances in Mechanical Engineering, University of Debrecen, Hungary, October 11-13, 2018, pp. 139-140, ISBN 978-963-490-051-1.
10. **Salman N.**, Pillinger G., Kiss P. (2019): Effect of the hard layer of the soil on the sinkage, *International Society for Terrain-Vehicle Systems (ISTVS) 15th European-African Regional Conference*, Prague, Czech Republic, September 9-11, 2019, (<https://www.istvs.org/15th-european-african-regional-conference-prague>), ISSN 1022-0313.

A3: Pressure-sinkage curves

Fig. A3.1. Pressure-sinkage curves of soil thickness of 18 cm at density of 1.36 g/cm³Fig. A3.2. Pressure-sinkage curves of soil thickness of 30 cm at density of 1.32 g/cm³

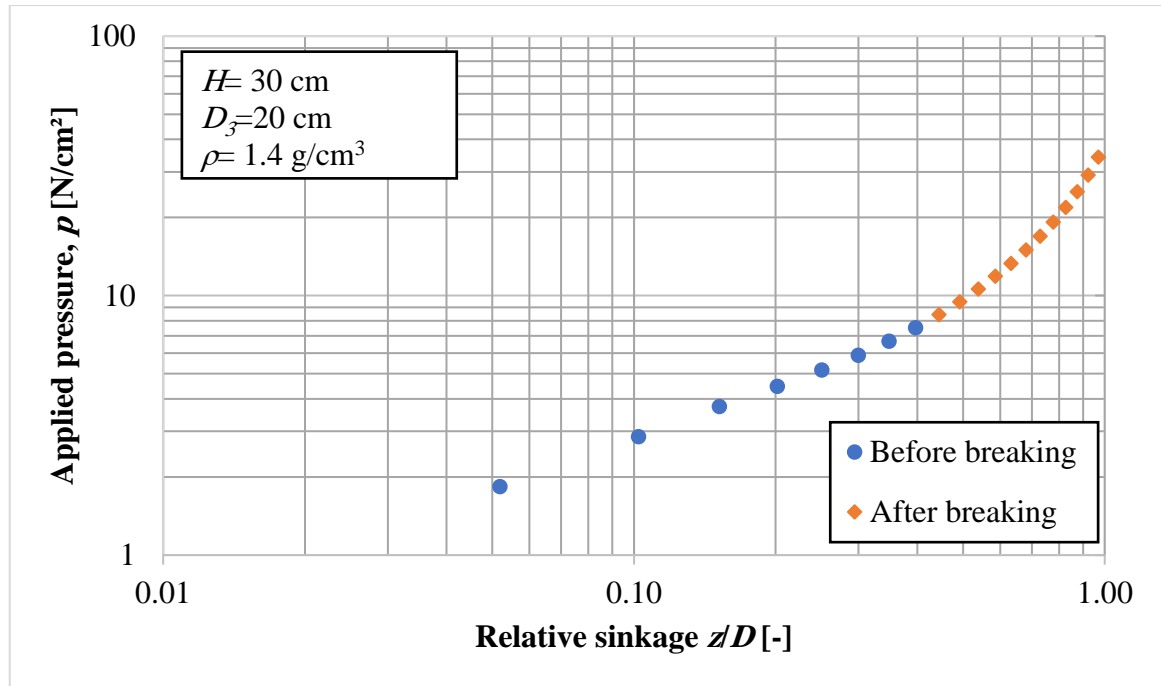


Fig. A3.3. Pressure-sinkage curves of soil thickness of 30 cm at density of 1.4 g/cm³

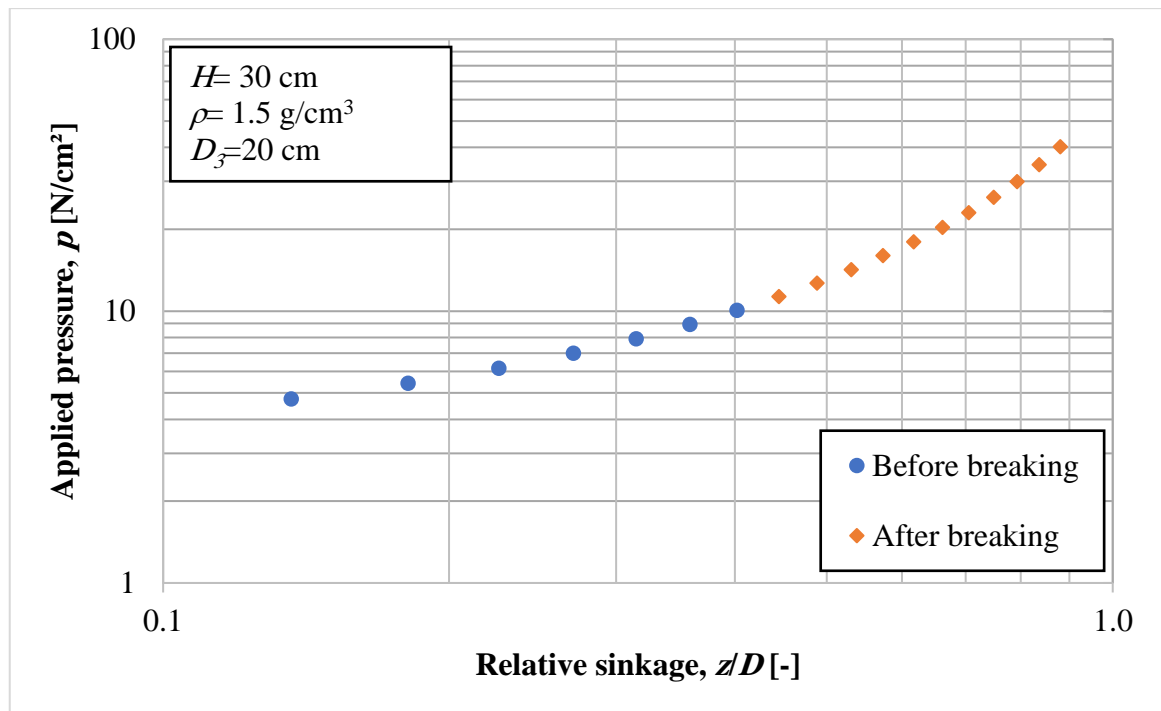


Fig. A3.4. Pressure-sinkage curves of soil thickness of 30 cm at density of 1.5 g/cm³

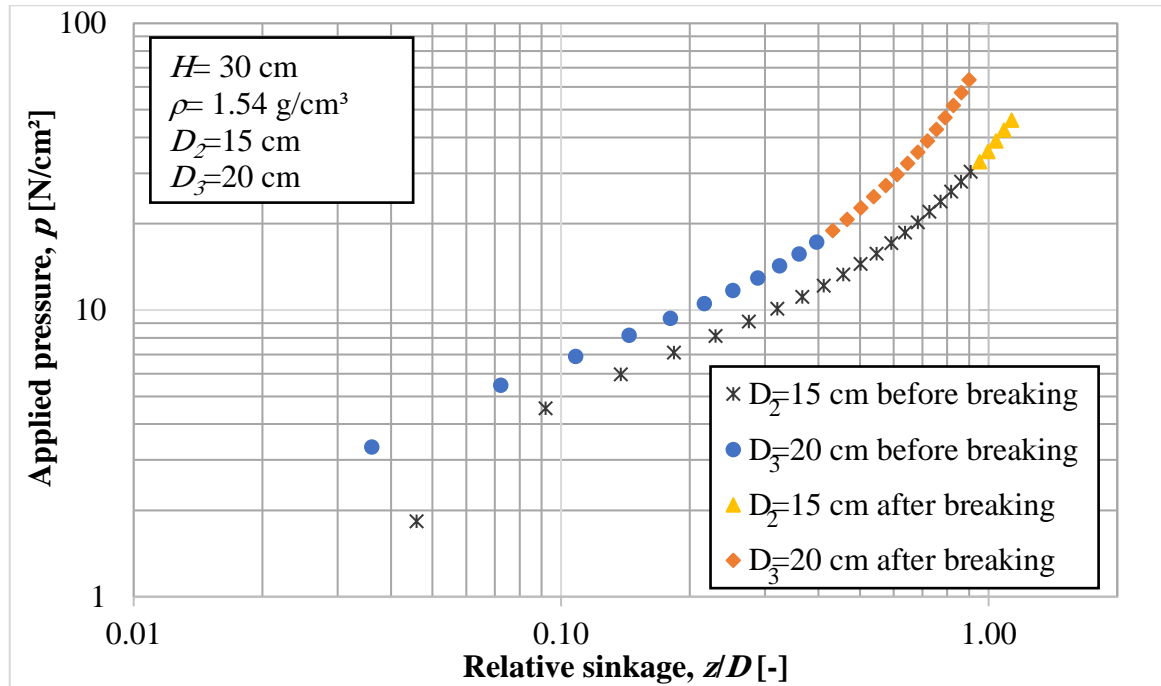


Fig. A3.5. Pressure-sinkage curves of soil thickness of 30 cm at density of 1.54 g/cm³

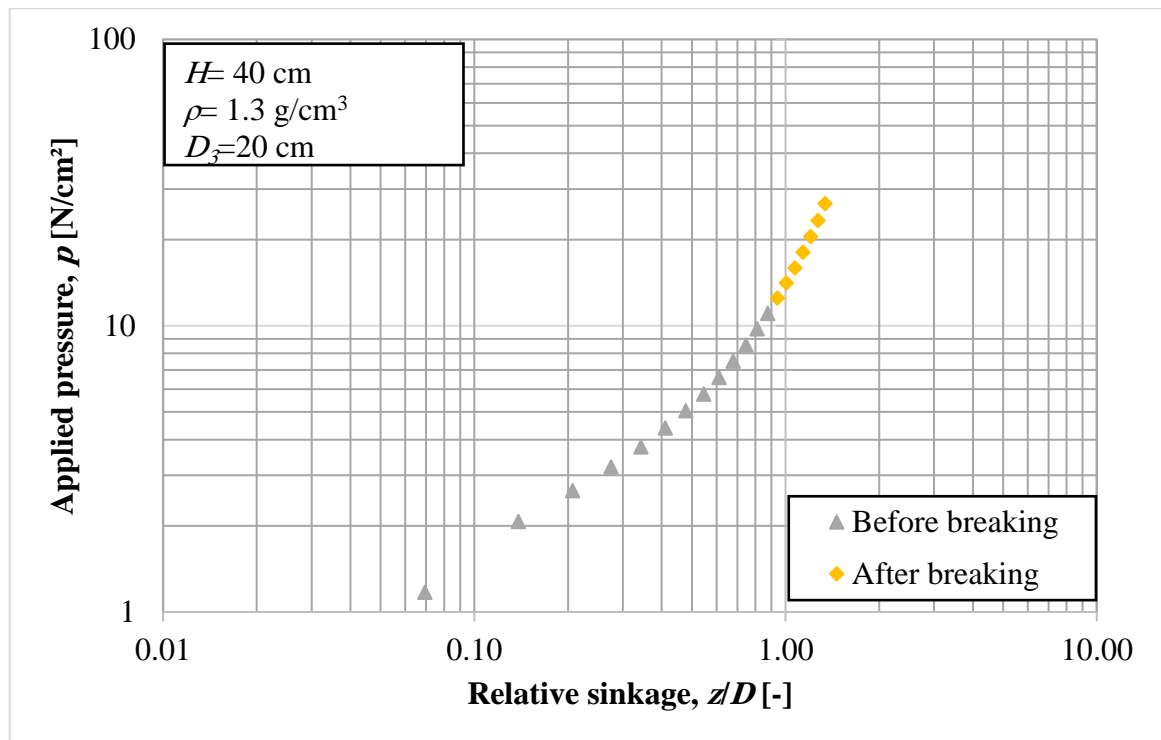
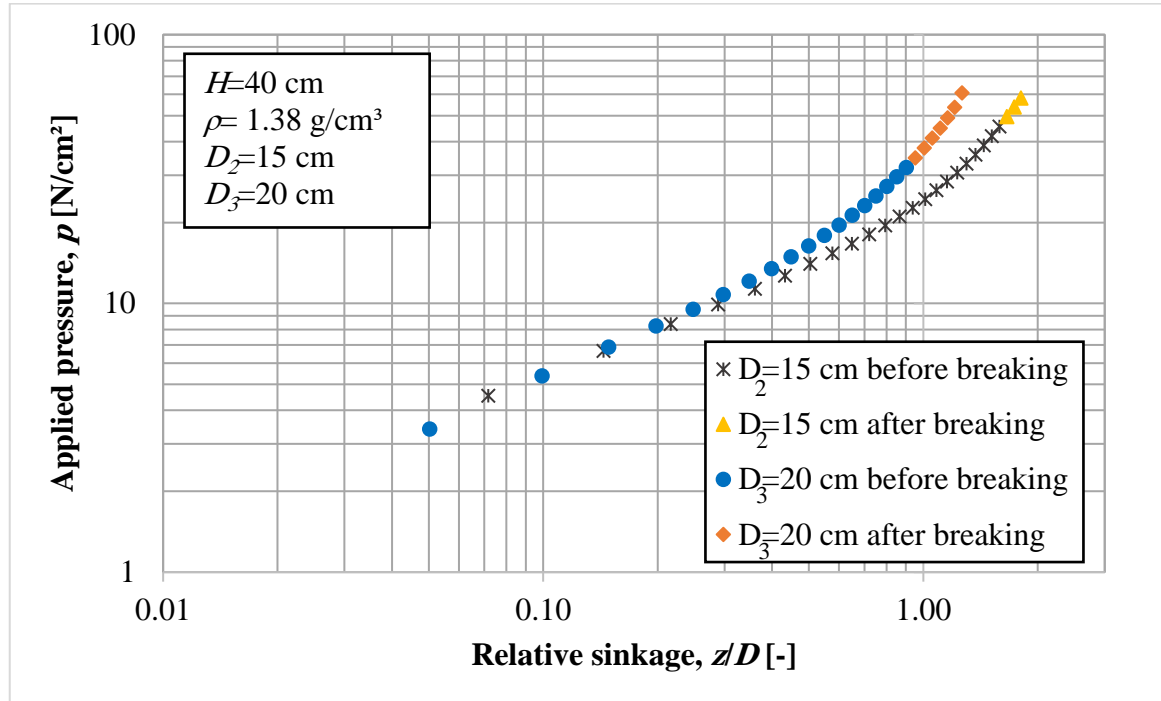
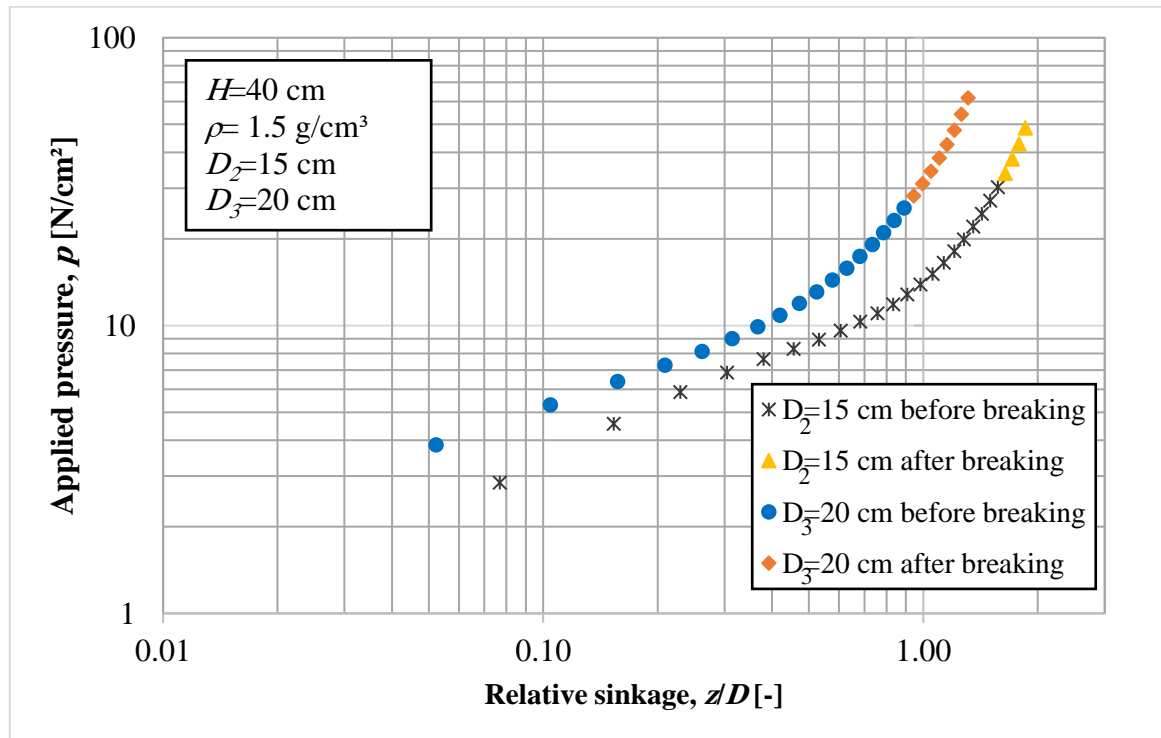


Fig. A3.6. Pressure-sinkage curves of soil thickness of 40 cm at density of 1.3 g/cm³

Fig. A3.7. Pressure-sinkage curves of soil thickness of 40 cm at density of 1.38 g/cm³Fig. A3.8. Pressure-sinkage curves of soil thickness of 40 cm at density of 1.5 g/cm³

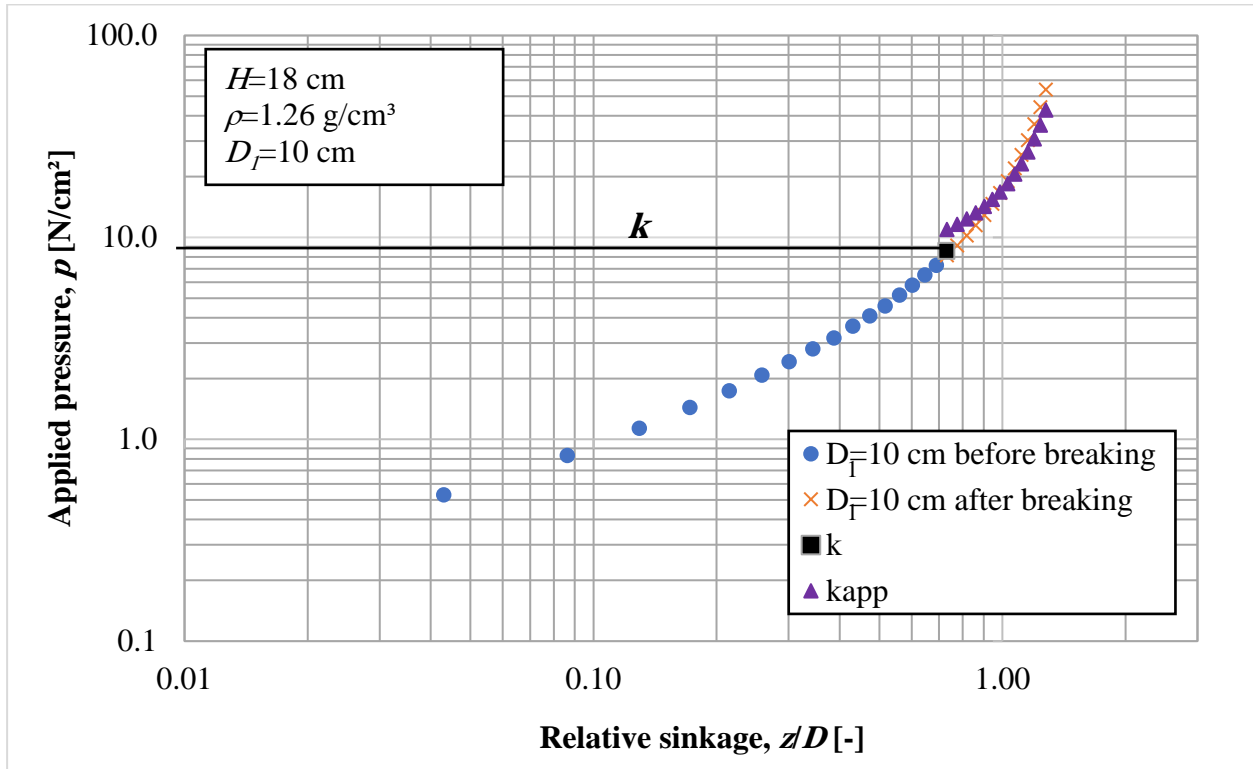
A4: Pressure-sinkage curves with k_{app} curves

Fig. A4.1. Pressure-sinkage curves with k_{app} curves of soil thickness of 18 cm at bulk density of 1.26 g/cm³ and sinkage plate diameter of 10 cm

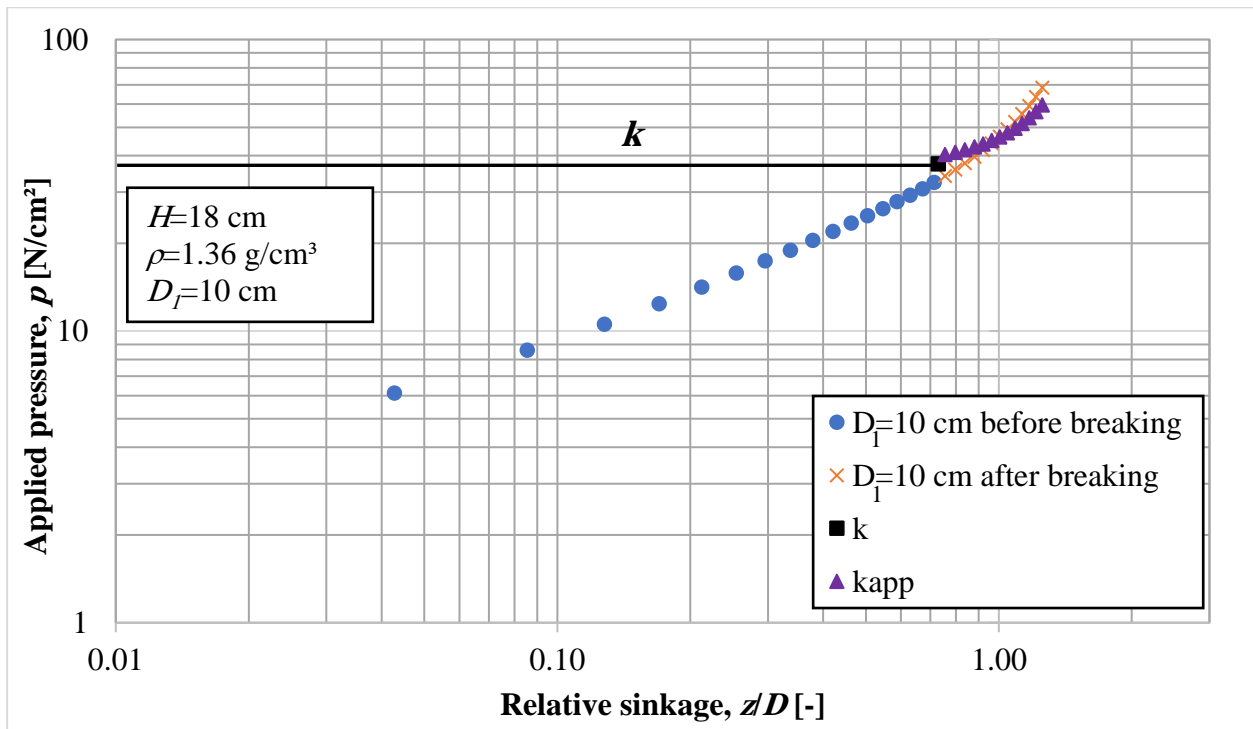


Fig. A4.2. Pressure-sinkage curves with k_{app} curves of soil thickness of 18 cm at bulk density of 1.36 g/cm³ and sinkage plate diameter of 10 cm

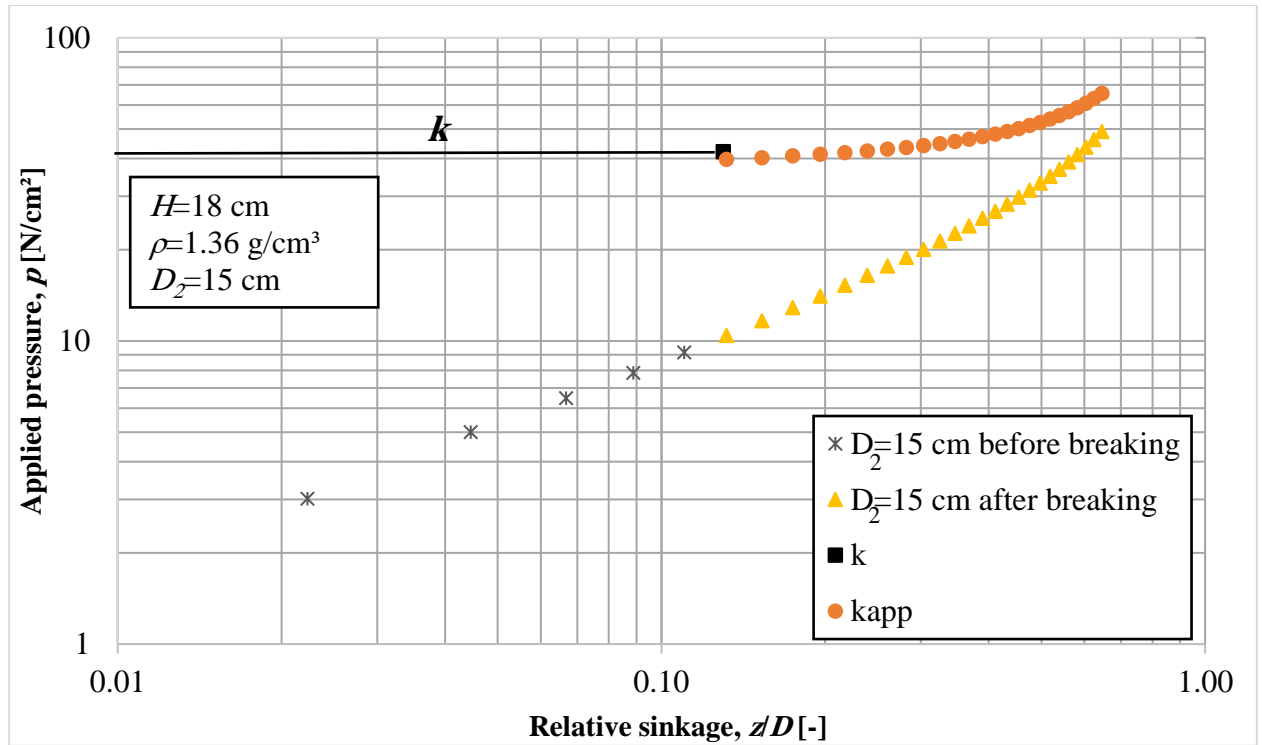


Fig. A4.3. Pressure-sinkage curves with k_{app} curves of soil thickness of 18 cm at bulk density of 1.36 g/cm³ and sinkage plate diameter of 15 cm

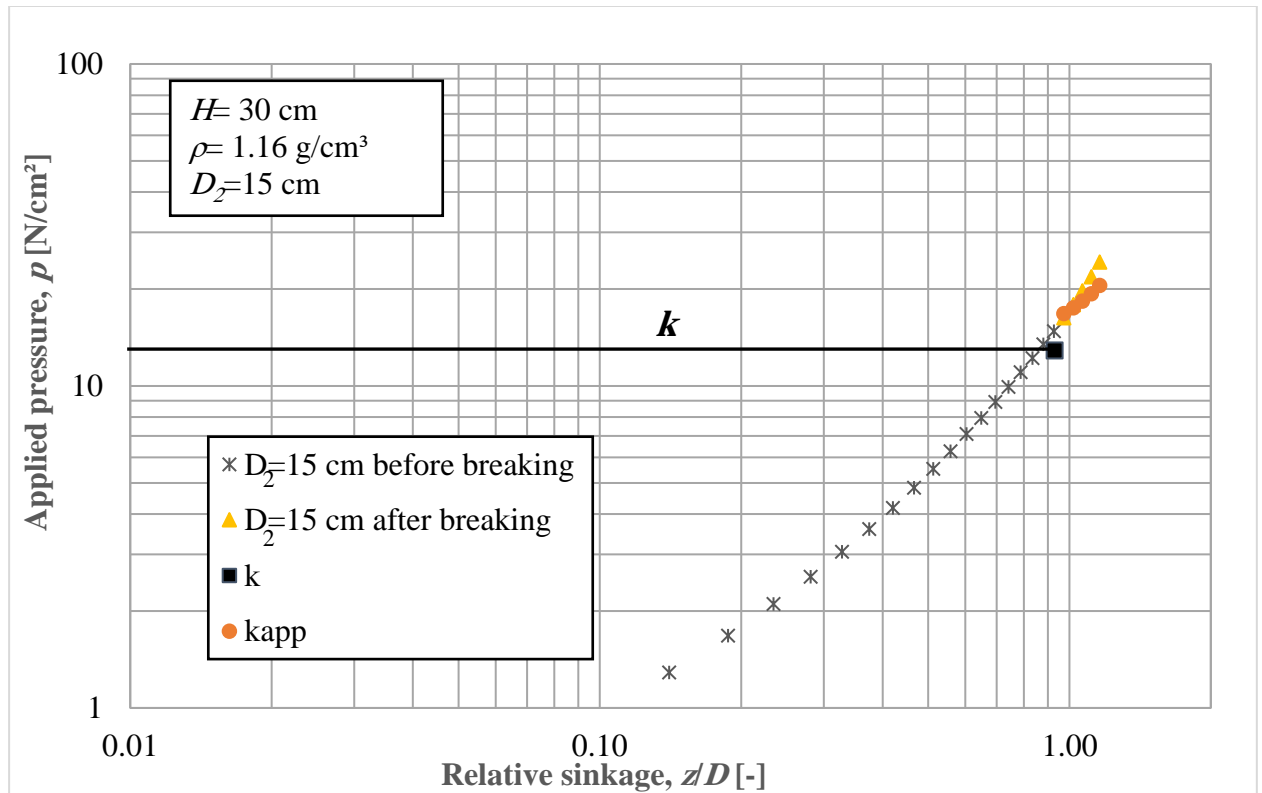


Fig. A4.4. Pressure-sinkage curves with k_{app} curves of soil thickness of 30 cm at bulk density of 1.16 g/cm³ and sinkage plate diameter of 15 cm

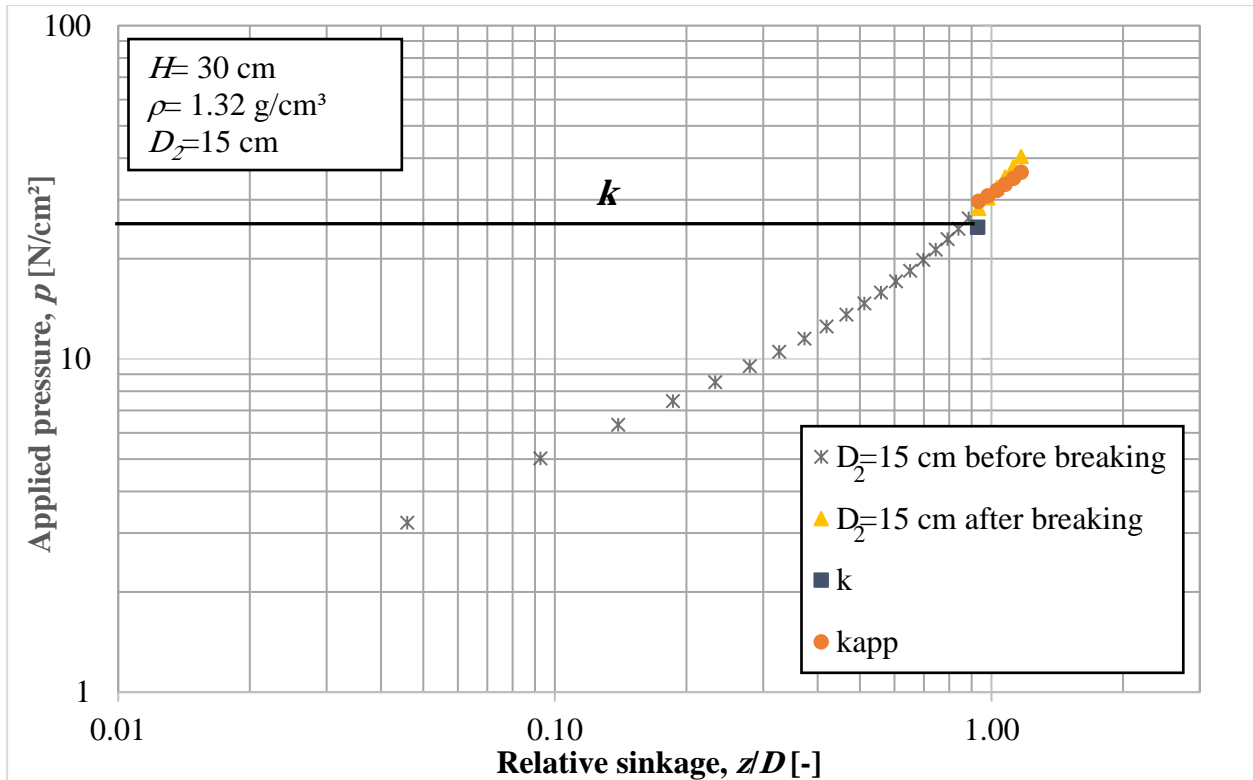


Fig. A4.5. Pressure-sinkage curves with k_{app} curves of soil thickness of 30 cm at bulk density of 1.32 g/cm³ and sinkage plate diameter of 15 cm

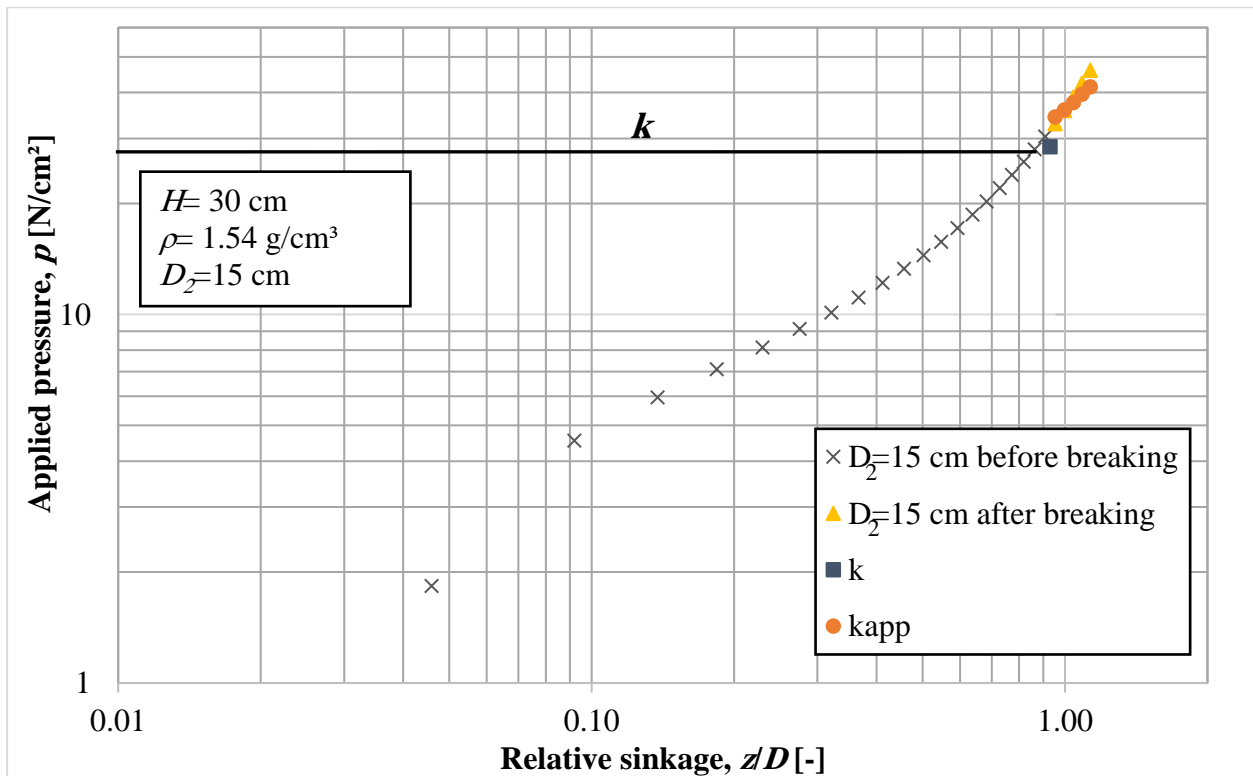


Fig. A4.5. Pressure-sinkage curves with k_{app} curves of soil thickness of 30 cm at bulk density of 1.54 g/cm³ and sinkage plate diameter of 15 cm

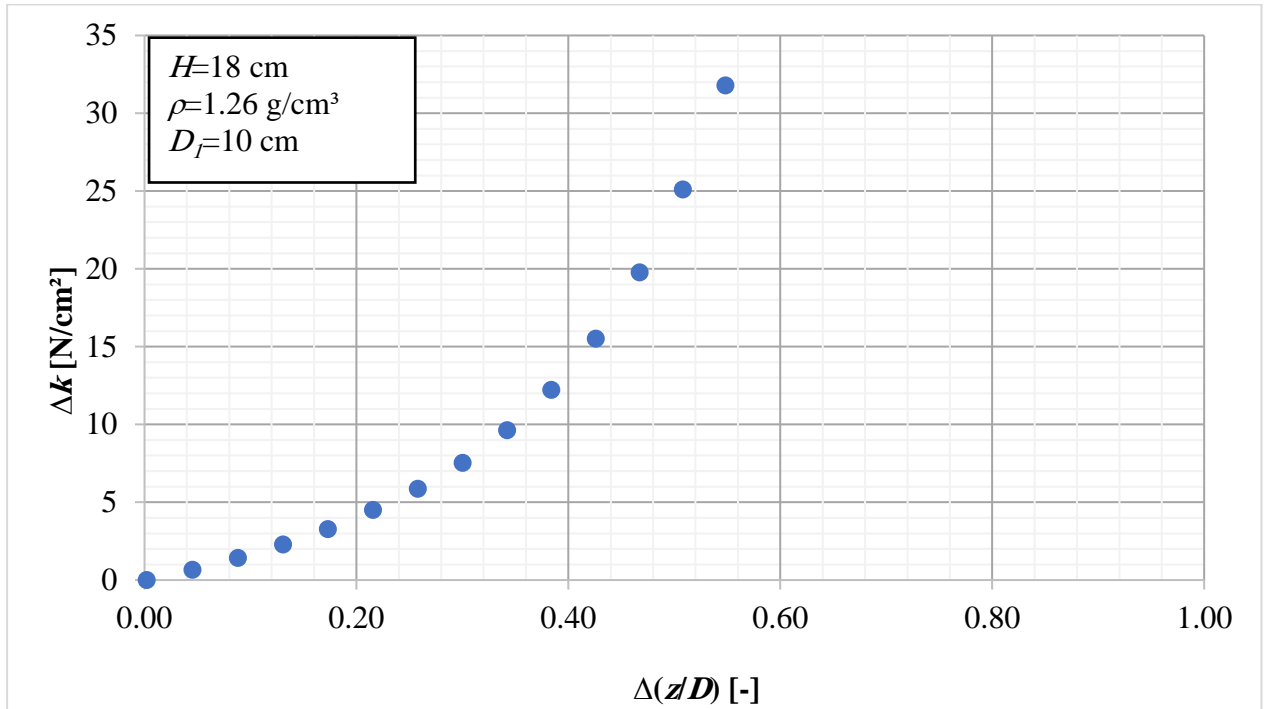
A5: Relation of Δk and $\Delta(z/D)$ 

Fig. A5.1. Pressure-sinkage curves with k_{app} curves of soil thickness of 18 cm at bulk density of 1.26 g/cm³ and sinkage plate diameter of 10 cm

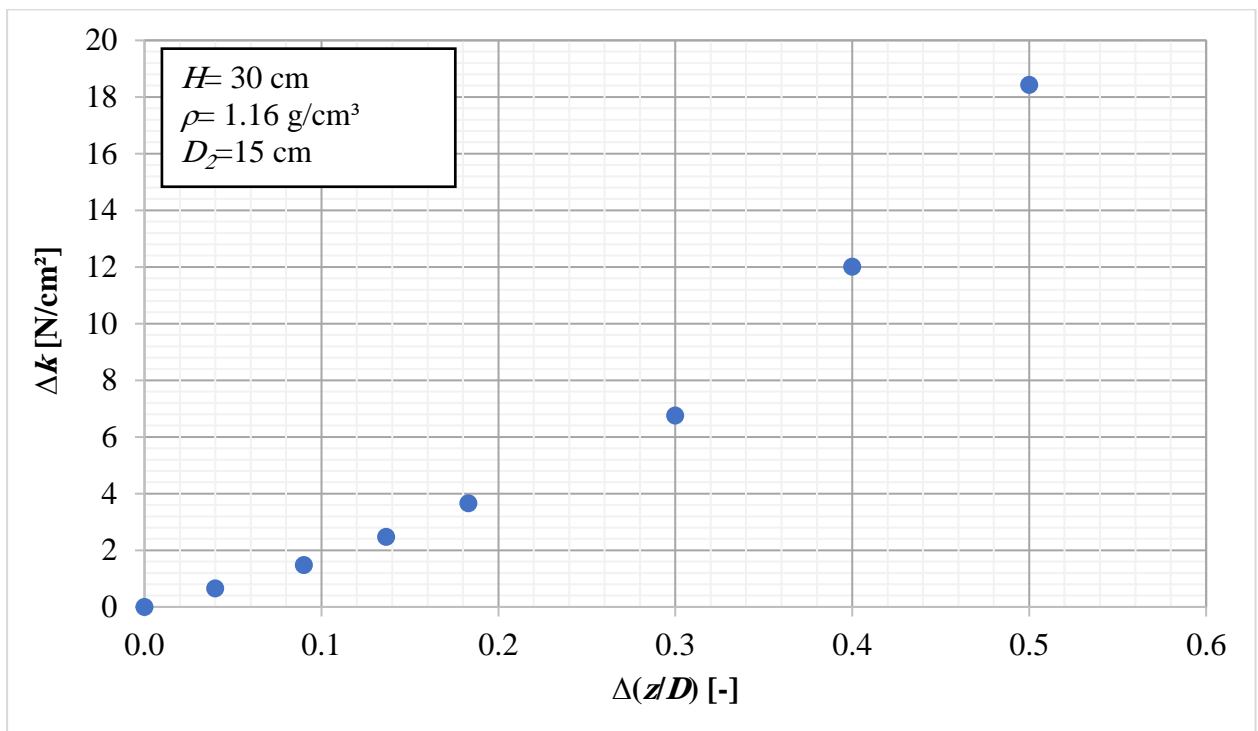


Fig. A5.2. Pressure-sinkage curves with k_{app} curves of soil thickness of 30 cm at bulk density of 1.16 g/cm³ and sinkage plate diameter of 15 cm

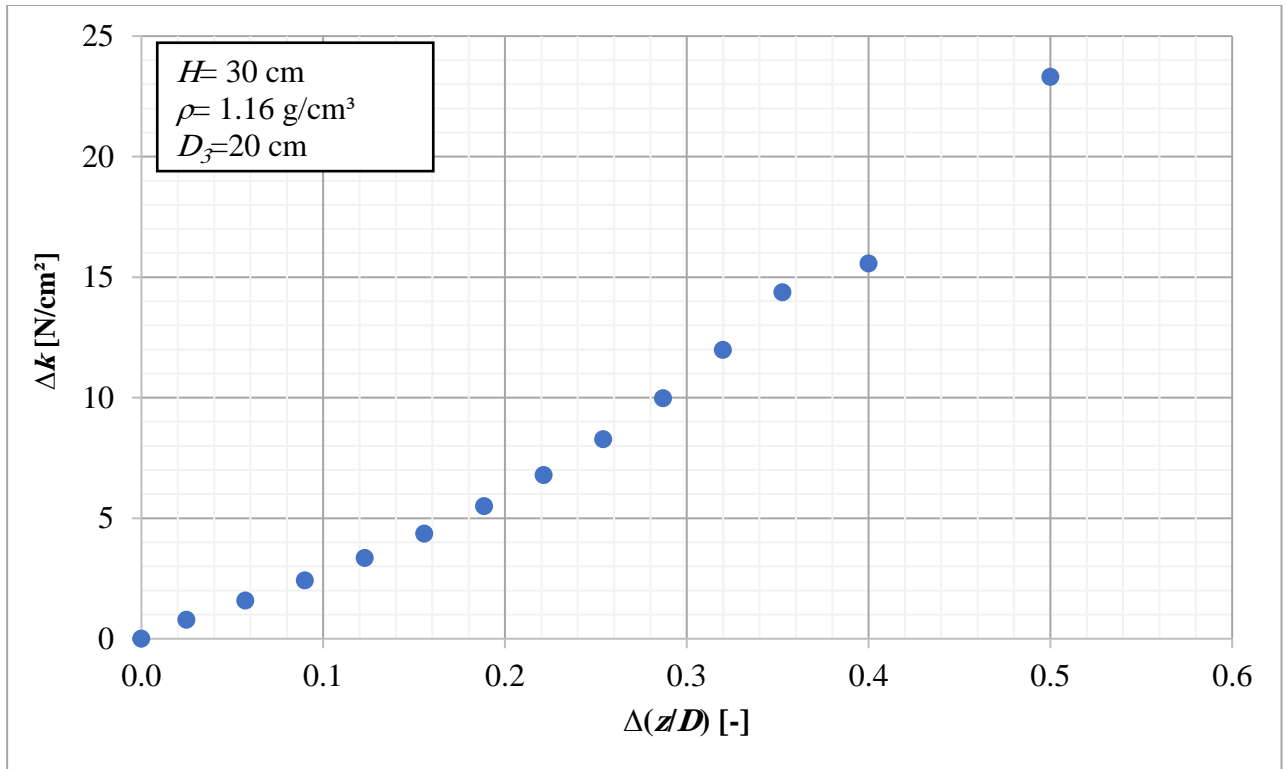


Fig. A5.3. Pressure-sinkage curves with k_{app} curves of soil thickness of 30 cm at bulk density of 1.16 g/cm³ and sinkage plate diameter of 20 cm

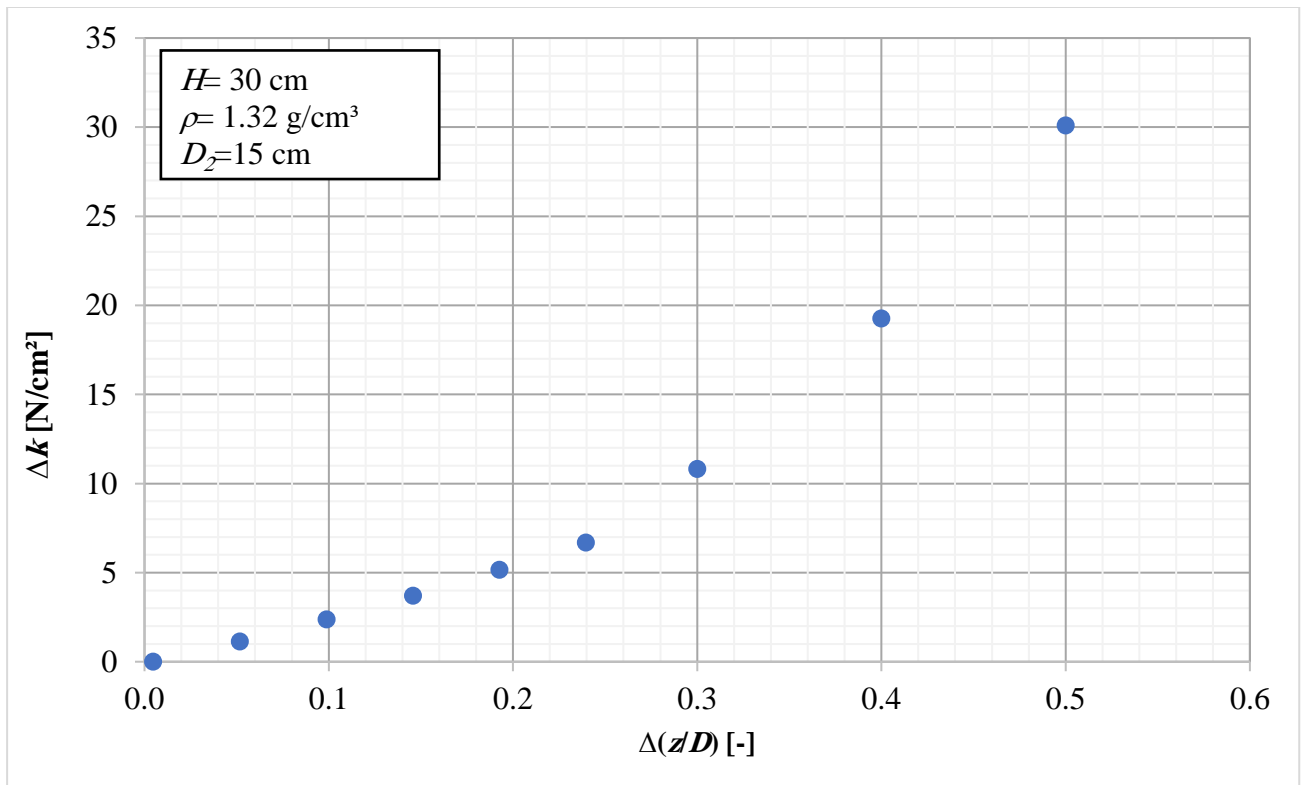


Fig. A5.4. Pressure-sinkage curves with k_{app} curves of soil thickness of 30 cm at bulk density of 1.32 g/cm³ and sinkage plate diameter of 15 cm

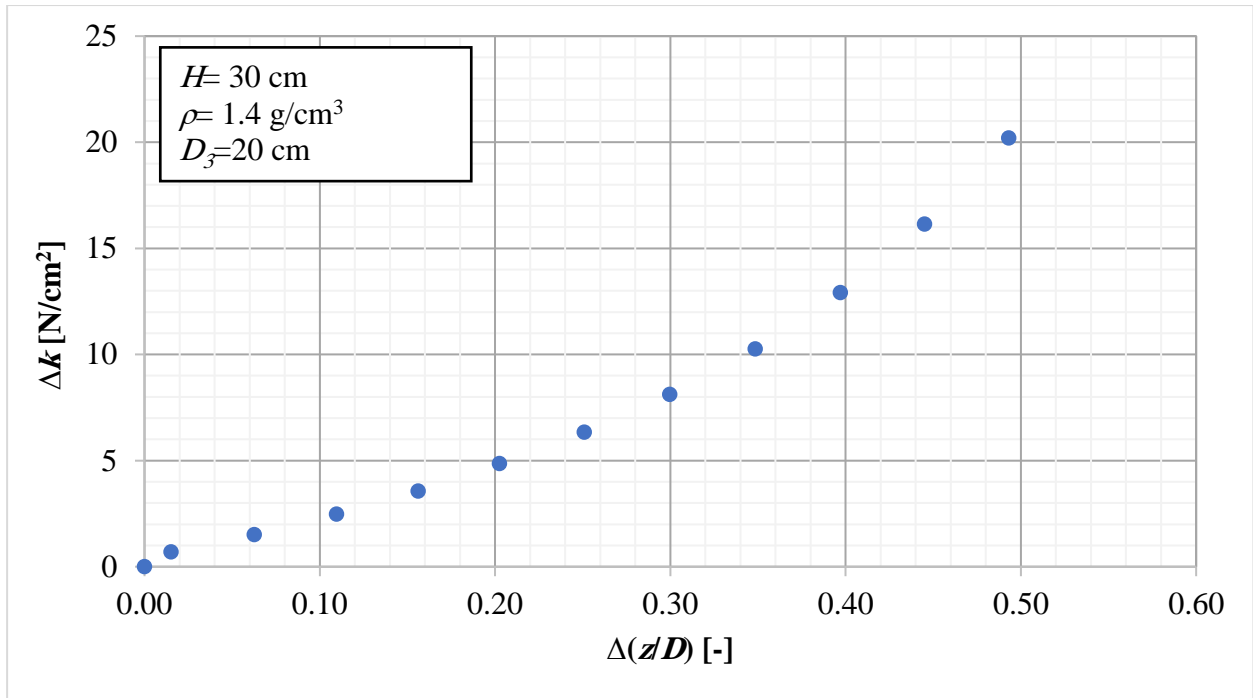


Fig. A5.5. Pressure-sinkage curves with k_{app} curves of soil thickness of 30 cm at bulk density of 1.4 g/cm³ and sinkage plate diameter of 20 cm

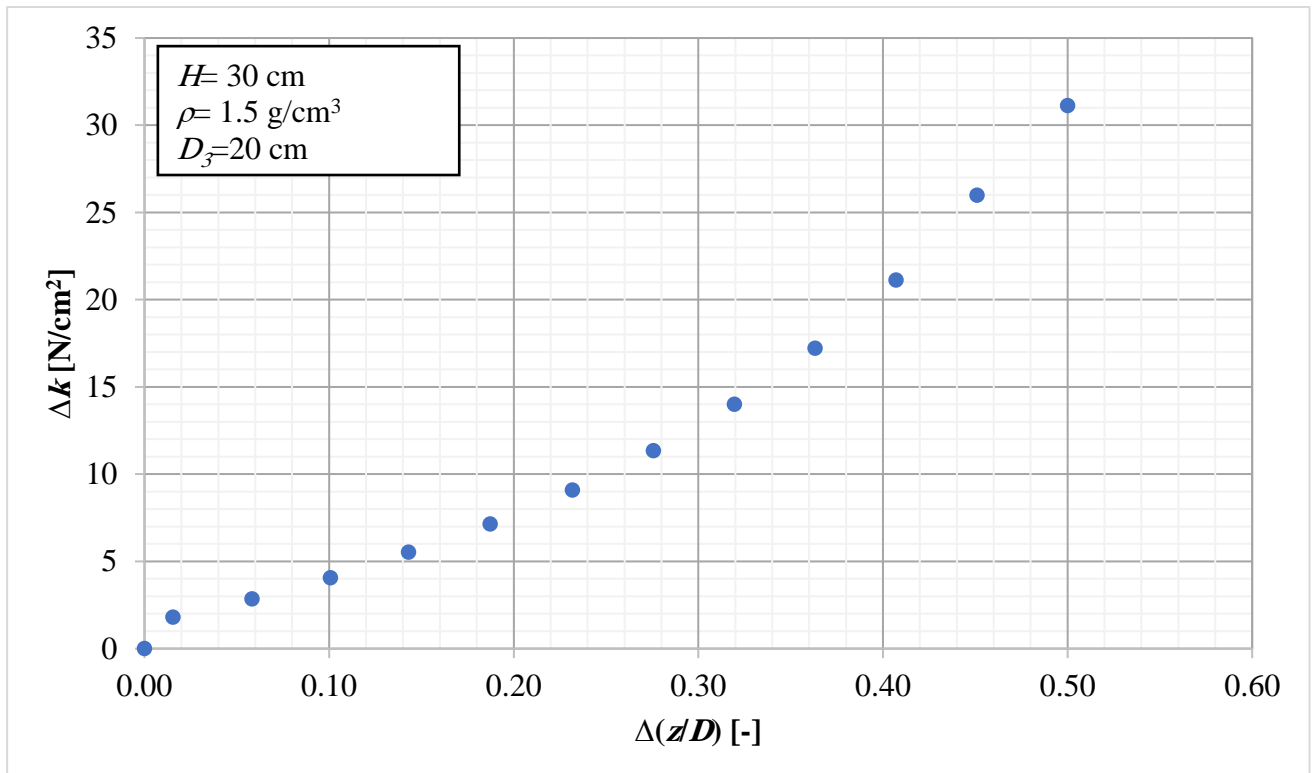


Fig. A5.6. Pressure-sinkage curves with k_{app} curves of soil thickness of 30 cm at bulk density of 1.5 g/cm³ and sinkage plate diameter of 20 cm

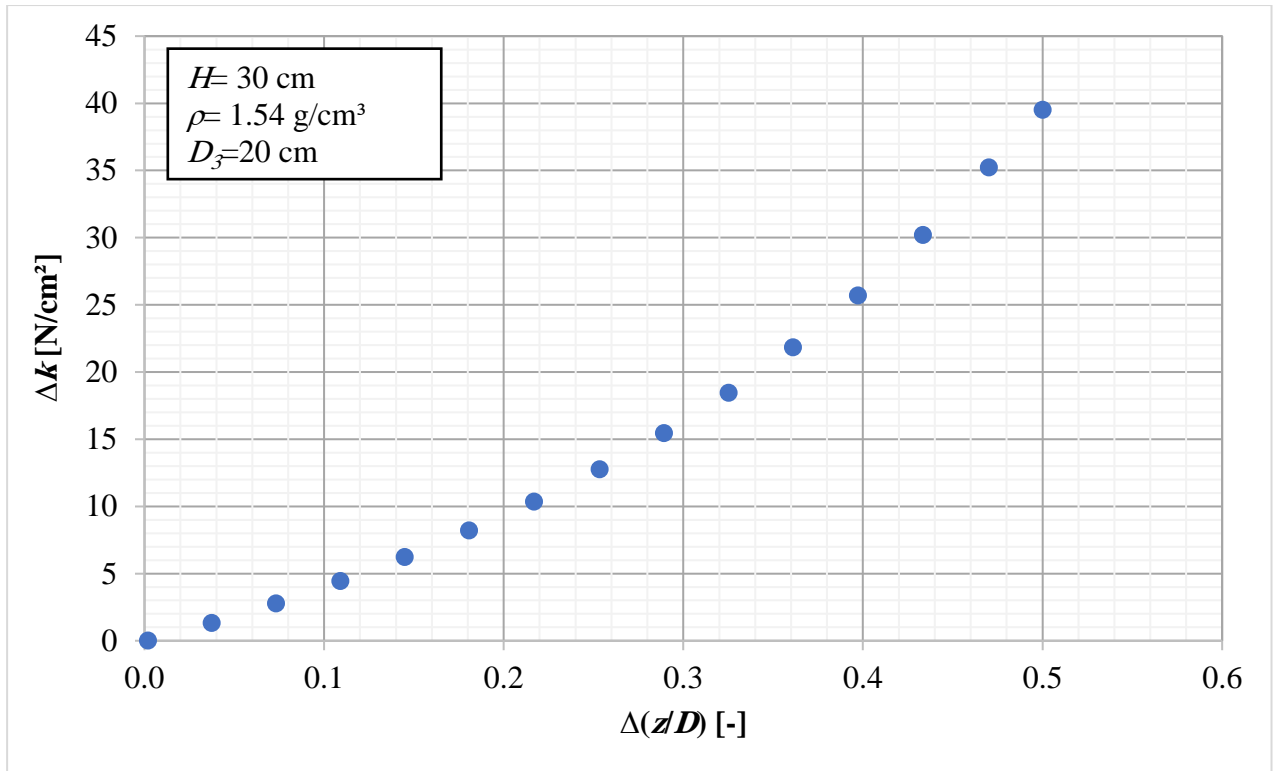


Fig. A5.7. Pressure-sinkage curves with k_{app} curves of soil thickness of 30 cm at bulk density of 1.54 g/cm³ and sinkage plate diameter of 20 cm

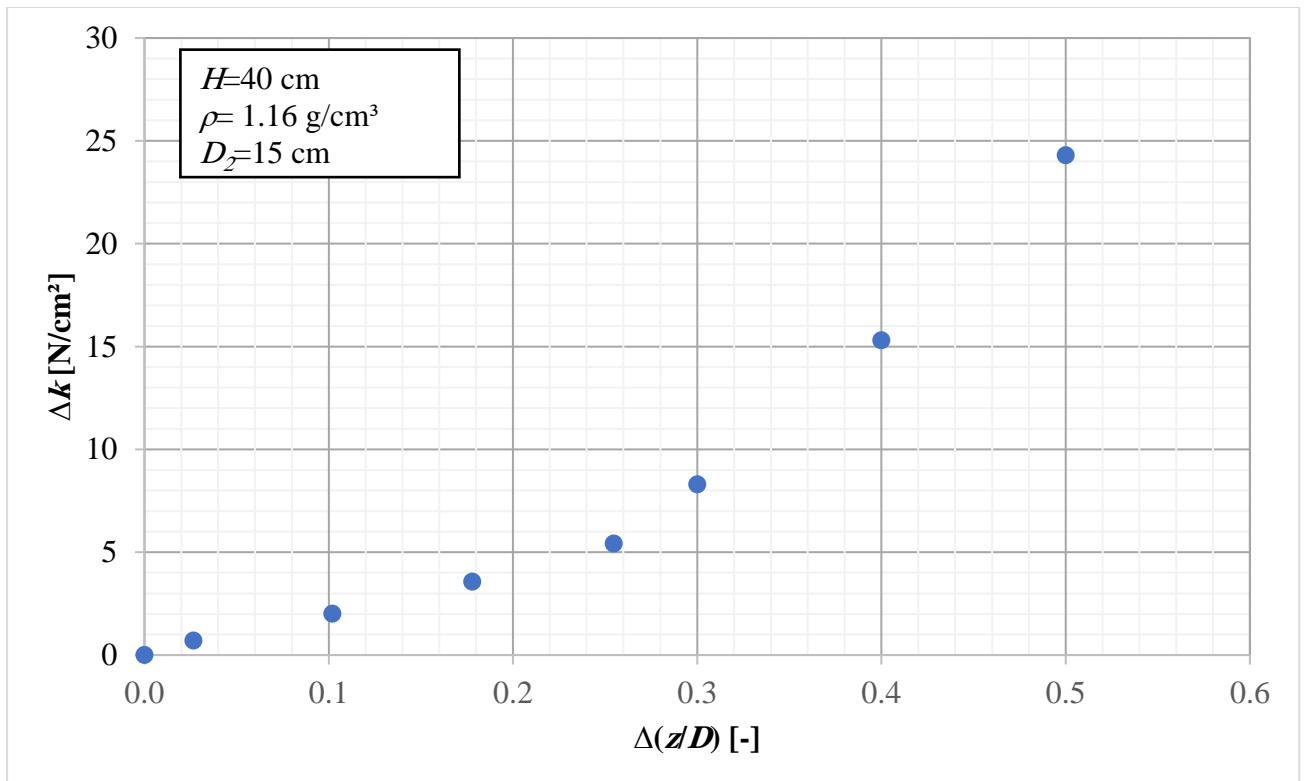


Fig. A5.8. Pressure-sinkage curves with k_{app} curves of soil thickness of 30 cm at bulk density of 1.16 /cm³ and sinkage plate diameter of 15 cm

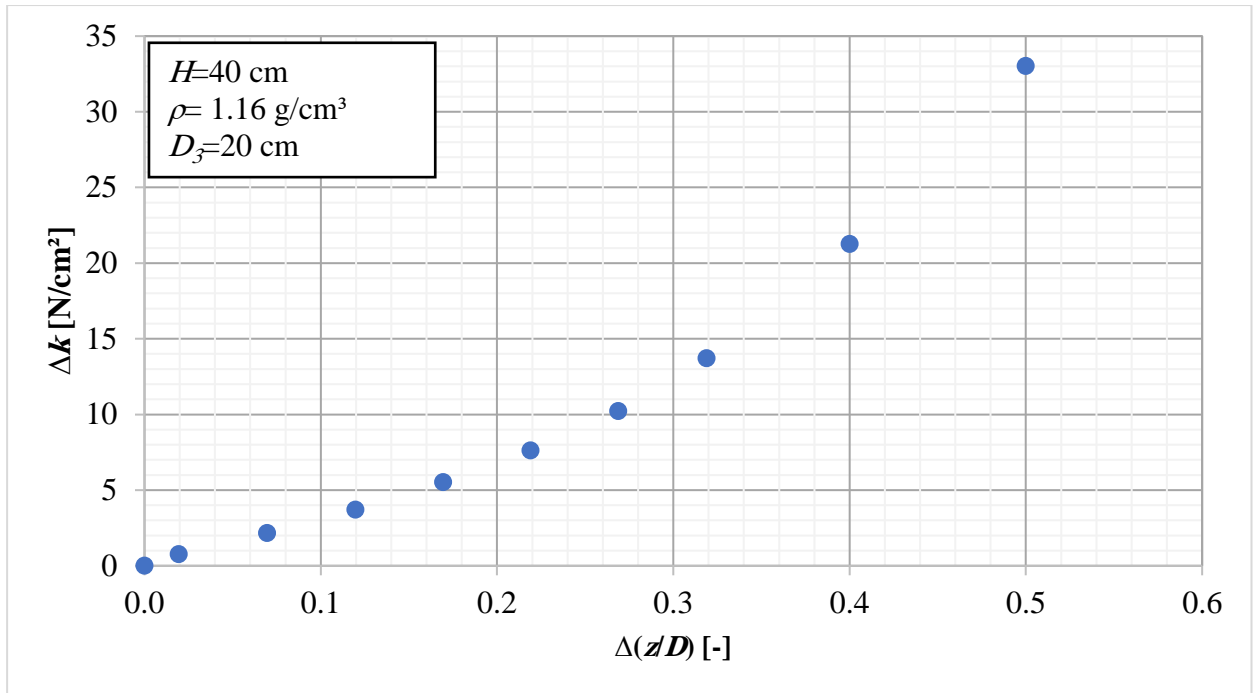


Fig. A5.9. Pressure-sinkage curves with k_{app} curves of soil thickness of 40 cm at bulk density of 1.16 g/cm³ and sinkage plate diameter of 20 cm

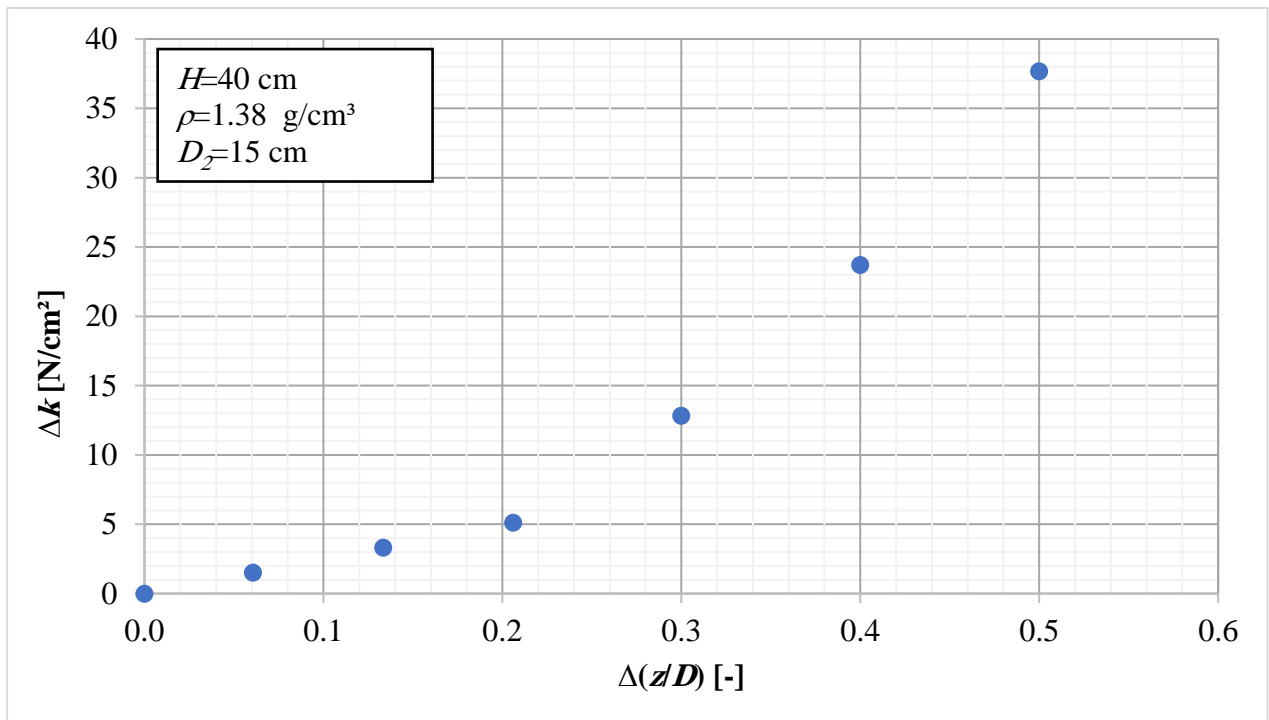


Fig. A5.10. Pressure-sinkage curves with k_{app} curves of soil thickness of 40 cm at bulk density of 1.38 g/cm³ and sinkage plate diameter of 15cm

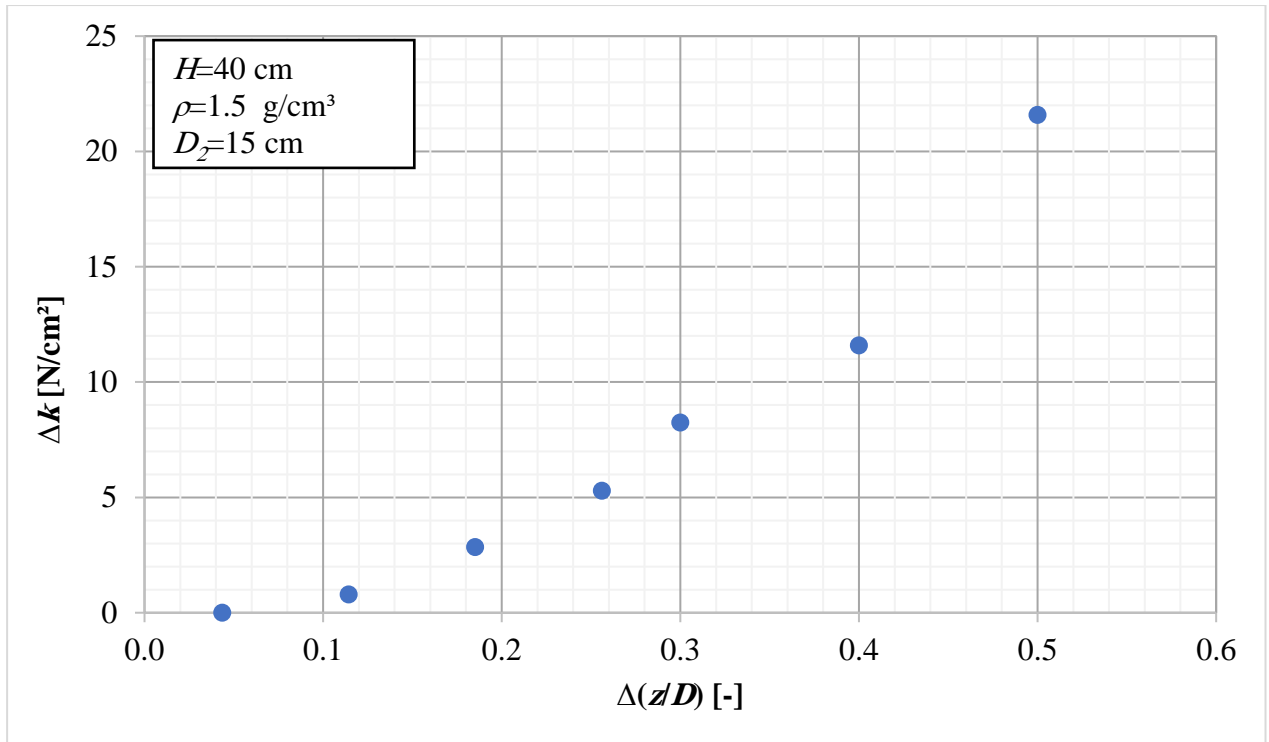


Fig. A5.11. Pressure-sinkage curves with k_{app} curves of soil thickness of 40 cm at bulk density of 1.5 g/cm³ and sinkage plate diameter of 15cm

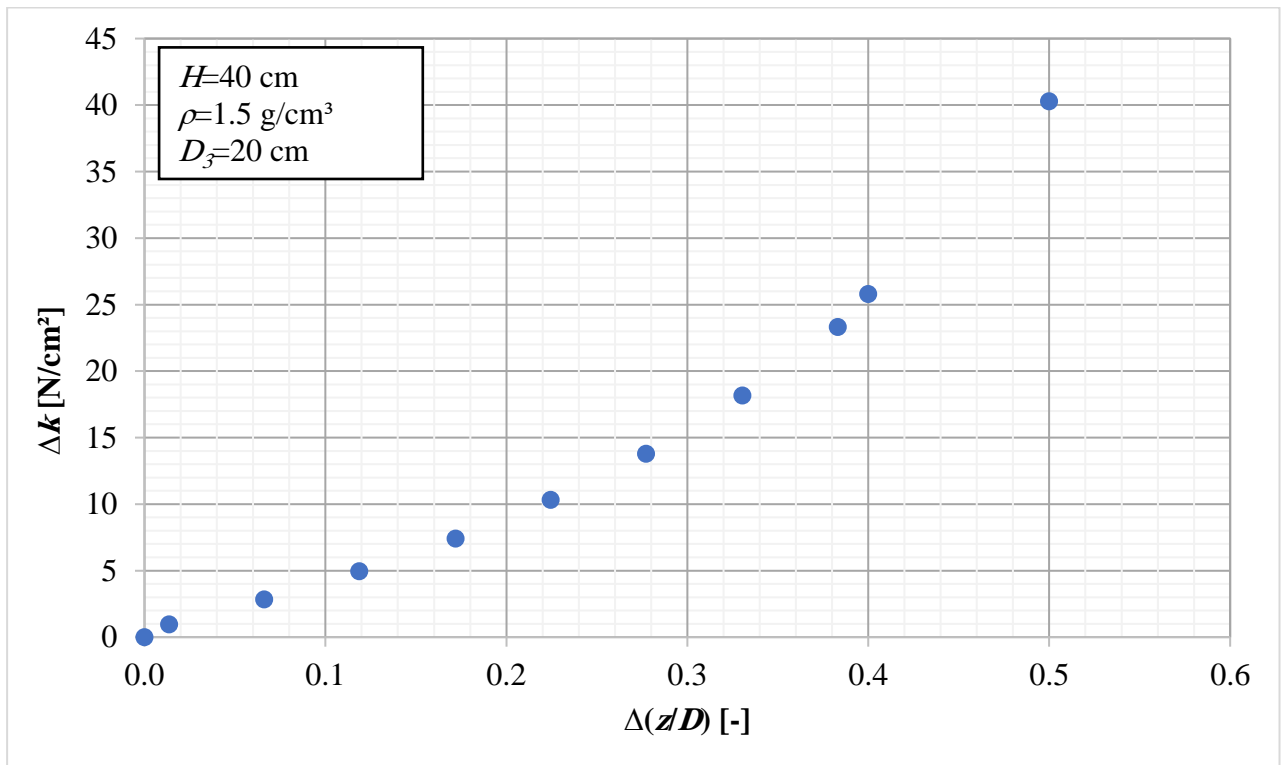


Fig. A5.12. Pressure-sinkage curves with k_{app} curves of soil thickness of 40cm at bulk density of 1.5 g/cm³ and sinkage plate diameter of 20 cm

9. ACKNOWLEDGEMENT

I would like to thank the following people who have helped me undertake this research:

My supervisor, Prof. Peter Kiss, for his patience, guidance, and support. I am extremely grateful that he took me on as a student and continued to have faith in me over the years.

Doctoral Schools of mechanical engineering, Prof. Dr. István Farkas (the former head of Ph.D. school), Prof. Dr. Gábor Kalácska (the current head of Ph.D. school), and Dr. István Seres (secretary of Ph.D. school), for all the considerate guidance.

Dr. Pillinger György, assistant professor at the department of vehicle technology, for his support, guidance. His insight, and knowledge into the subject matter steered me through this research.

My husband Muammel M. Hanon, for all his support. He guided me so positively and always made me feel confident in my abilities. Without him, I would not have been able to complete this journey.

Ms. Zsuzsanna Tassy, International PhD coordinator at DHC, for her kindness, and all her support during this journey.

Tamás Török, a worker at the workshop in the department of vehicle technology for his assistance in conducting the experiments.

My biggest thanks to my family (father, mother, sisters, and brothers) for all the support they have shown me throughout this journey.

My Mates and friends for their support and encouragement all through my studies.

Finally, I would like to express my sincere gratitude to Stipendium Hungaricum Scholarship Program and my country (Iraq) for nominating me for this position and giving me the opportunity to do the Ph.D. in Hungary.

Gödöllő, March 2022

Nihal Dawood Salman